University of California
Santa Barbara

Probing and engineering the environment of near-surface nitrogen-vacancy centers in diamond for quantum sensing and simulation

A dissertation submitted in partial satisfaction
of the requirements for the degree

Doctor of Philosophy
in
Physics

by

Zhiran Zhang

Committee in charge:

Professor Ania C. Bleszynski Jayich, Chair
Professor Mark S. Sherwin
Professor Mark Srednicki

March 2024

The Dissertation of Zhiran Zhang is approved.

Professor Mark S. Sherwin

Professor Mark Srednicki

Professor Ania C. Bleszynski Jayich, Committee Chair

March 2024

Probing and engineering the environment of near-surface nitrogen-vacancy centers in diamond for quantum sensing and simulation

by

Zhiran Zhang

For my beloved family

Acknowledgements

First, I would like to thank all the government agencies who support my research during Ph.D., including NSF, DARPA, DOD, DOE, AFRL and ARO. My research is also supported by the shared facilities of the National Science Foundation (NSF) Materials Research Science and Engineering Center (MRSEC) at UCSB, and the NSF Quantum Foundry through Q-AMASE-i program award, Quantum Structures Facility within the UCSB California NanoSystems Institute, and the UCSB NanoFabrication facility. Everything described in this dissertation would not be possible without their support.

I cannot express how grateful I am to my advisor Prof. Ania Jayich. Ania has introduced me to quantum physics and advised me in the past almost seven years. She is very supportive and resourceful to guide our research without falling down the rabbit holes, while giving me great freedom to pursue my research ideas and explore physics. I am amazed by how much wonderful work we have done so far when I look back at our results and write this dissertation. Her passion about physics inspires me a lot. During the COVID-19 pandemic, when our DNA origami project was put on hold, Ania pivoted our focus to a new project that we could work on remotely. That not only broadened my horizons and research interests, but also leads to my first published paper. Ania is always patient with me and other students in the group. She is willing to help with all of our problems both in research and in life. Her office is always open to us whenever she is available, and I can just show up and discuss our experiments with her. Ania would pay attention to all the details in the experiment of all stages and offers us insightful suggestions, even when she is busy with the proposals or other things. I cherish the moments spent in Ania's office when she offered me help so that I can continue my research and overcome the hurdles in my life. Prof. Deborah Fygenson also mentored me a lot on the origami project, and patiently taught me the fundamentals of working

in a wet lab. The memories of the busy old days will be left in my heart, when Deborah and I have to drive three hours to Winfree's lab at Caltech together to perform exciting experiments and drive back to Santa Barbara at night.

It has been a great pleasure to work with all the physicists I have met in Jayich lab and also people from other groups. I joined Jayich lab in the 2017 immediately after I came to UCSB. Unfortunately I didn't have a chance to work with Bryan Myers since he has already graduated. Both Dolev and I found that his dissertation is really the bible in our lab, especially for the experiments on the 1219 temperature setup. I only had a very short time overlapping with Amila Ariyaratne. He, Dolev and Bryan built the scanning system on the 1219 setup, and performed difficult but beautiful scanning experiment. Even today I feel very lucky to be mentored by and work with Dolev Bluvstein. We have worked very closely on three projects before he graduated from UCSB. Dolev was leading the first two projects and mentoring me on the third one, the DNA origami project, for which we finally achieved our first goal recently. I can safely say that Dolev and Ania taught me everything about NV centers and about how to be a good researcher. He is incredibly diligent and insightful, yet remains modest and enjoyable to collaborate with, and I admire him a lot. Taylor Morrison is the other Ph.D. student I have been working with very closely in recent years. I am so amazed to see how he scale up his skills quickly to build the whole 4215 cryo-setup from scratch, and have learnt everything I am capable to do for our origami project.

I have been working in the Broida room 1219 for a long time during my Ph.D., so I mainly share the lab space with the spin-phonon team. Jeff Cady is the one who introduced me to the hybrid quantum system in diamond. Although he keeps his gravity all along but he is actually very helpful and kind to others, and I often ask him a lot of basic questions about NV centers. Ohad Michel is also an excellent electronic engineer. He went to work in a local technology company afterwards and I occasionally met him

and his family around the campus housing. Carl Padgett, Viraj Dharod, Hyunseok Oh are the new spin-phonon team. I find they are focusing on different aspects of their experiments and they have all become experts in their focused realms in a short time. Carl is leading the measurement on the other setup they have in 1219, and he has a deep understanding of the physics of the spin-phonon system. Viraj is leading the construction of their dil-fridge. As mentioned in Simon's thesis, I also feel Viraj always figures out the problems until the first principles, which is a crucial merit for scientists. Hyunseok is a master of cleanroom fabrication, and he learns things really quickly. He is taking over even more experiments besides the fabrication of optomechanical crystals. (My family went to Hyunseok and Eunseo's wedding ceremony on the Goleta beach and it was so beautiful.) Our new postdoc researcher Jayameenakshi Venkatraman joined us very recently and is working closely with both spin-phonon team and many-body team. I think Jaya is so good at both theoretical and experimental physics, and she has such a broad research interests. There is no doubt that she will keep being very successful in the future and form her own research group.

Claire McLellan, Simon Meynell, and Lillian Hughes are in charge of the diamond growth in our lab during my time in Jayich group. I really appreciate the effort they have made to constantly studying and innovating growth techniques, and all of our experiments are not even possible to get started without the high-quality and novel diamond samples they grow. Furthermore, Claire and Tim Eichhorn show me how close collaboration between two smart scientists could yield great results. Simon and I entered both the Ph.D. program and Jayich lab around the same time. Simon has very good insight for multiple fields in physics, and looks into questions on a broad horizon, which is something that I am trying to learn from him. Discussion with him has been always useful for me. Lillian is able to make numerous advances beyond the existing foundations of her field of study. We have been collaborating on several projects. Lillian always listens to me

carefully and patiently, and the communication between us has always been so efficient even though I am not very fluent.

Shreyas Parthasarathy is working on a research direction similar to Taylor and me, and we shall work with each other more often in the coming year as the members of "many-body team". Shreyas is brilliant and works very hard to get to the bottom of the critical problems in our lab. I think his research reshaped the experiment skills and knowledge base that everyone has. Also, Shreyas and Lillian are in charge of the group social events, and I really appreciate that. Maxime Joos used to be the post-doc researcher before the "many-body" team formed. I feel he really enjoys studying physics, doing experiments and surfing, and he is good at all of them. He also kindly helped me a lot on one of the projects. Jason Chen is a smart and hardworking new Ph.D. student in our many-body team, but he has already contributed so much to our experiments even though he is in his first year. I believe he will keep taking more responsibilities in lab and having fruitful experiment outcomes during his Ph.D. here.

Alec Jenkins is the cleanroom expert and developed the best method for probe fabrication. He is capable to do all kinds of experiments and fabrications and is such a nice person that he would try to help everyone even during his busiest time. Daipeng Yang works on the low temperature scanning experiment as well and inherit the experiment skills from Alec. He works in PSB all the time, but we would often get together to discuss. Daipeng is truly a determined and optimistic person and he has thrived and overcome the challenges in experiments and in life. Sunghoon Kim and Jeff Ahlers are another two brilliant physicists working on scanning projects. Sunghoon understands physics and experiments deeply and keeps improving our experiments. Jeff is probably the best engineer in our group and he kindly takes over many lab jobs. I haven't got chances to know much about Aaron Schwan yet, but I will stay a little longer in UCSB after defense and hopefully know him better. Paz London was already an expert in NV

center before he joined our group. He was also working on scanning experiments and he managed to update our setup software which saves everyone a lot of time. Wenbo Wang worked as a postdoc in our lab for two years. He discussed science and life with me a lot during pandemic. He has started his own group in China and I wish him the best luck with that.

There are so many other outstanding undergraduate students in our group. Chang Jin contributed so much to our experiments, and he is willing to take over multiple different tasks and work on them in parallel. Cole Williams helped Taylor to build the setup and is very cautious when he performed experiments. Yuanqi Lyu is pretty good at theory and he helped me on many derivations. Sophia Han helped to build "cage" setup which we often use for characterizing diamond samples. She is also a close friend to me and my wife. I used to work with Haopu Yang on the 1D many-body project for a while. I found him very optimistic and motivated, and his results on GSD microscopy and 1D physics prove his excellent experiment skills.

I also would like to thank my committee members, Prof. Mark Sherwin and Prof. Mark Srednicki for all the advice on my research and my dissertation. Prof. Mark Sherwin and his student Black Wilson also offer us a lot of help with EPR measurements and connect us with Prof. Songi Han and her student Chung-Ta Han, who kindly let us perform experiment on their setup. Prof. Mark Srednicki would discuss both my research progress and all the obstacles in my profession path with me, every time when we met for annual updates, and I am really thankful for that.

Lastly, I want to thank all my friends and my beloved family. My parents always completely support me with all my decisions including my choise to pursue this Ph.D. degree. They shape me into a resilient person since I was young. My love Mengye and I met each other during the pandemic, and we have got married and had a baby, our daughter Sofia. It is not easy to get where we are today. My wife has been always

inspiring me and giving me help. Although we seldom say it aloud, I deeply know in my heart that she supports me unconditionally. Mengye, my mom, and my parents in law take care of Sofia a lot since she was born, so that I can focus more on my research. Overall, I have had a great time here in Santa Barbara with my family, and it has become such an incomparably precious memory for me.

Curriculum Vitæ

Zhiran Zhang

Education

2017-2024	Ph.D. in Physics (Expected), University of California, Santa Barbara.
2017-2020	M.A. in Physics, University of California, Santa Barbara.
2013-2017	B.S. in Physics, Peking University, Beijing, China

Publications

6. **Zhiran Zhang**, Taylor Morrison, Lillian Hughes, Weijie Wu, Ruiyao Liu, Dolev Bluvstein, Norman Y. Yao, Deborah Fygenson, and Ania C. Bleszynski Jayich, Diamond defect-based sensing of programmably patterned molecular spin arrays with single-spin sensitivity, in preparation, (2024)
5. **Zhiran Zhang**, Maxime Joos, Dolev Bluvstein, Yuanqi Lyu, Ania C Bleszynski Jayich, Reporter-Spin-Assisted T_1 Relaxometry, *Phys. Rev. Applied*, **19**, L031004, (2023)
4. Lillian B. Hughes, **Zhiran Zhang**, Chang Jin, Simon A. Meynell, Bingtian Ye, Weijie Wu, Zilin Wang, Emily J. Davis, Thomas E. Mates, Norman Y. Yao, Kunal Mukherjee, Ania C. Bleszynski Jayich, Two-dimensional spin systems in PECVD-grown diamond with tunable density and long coherence for enhanced quantum sensing and simulation, *APL Material*, **11**, 021101, (2023)
3. Dolev Bluvstein, **Zhiran Zhang**, Claire A. McLellan, Nicolas R. Williams, and Ania C. Bleszynski Jayich, Extending the quantum coherence of a near-surface qubit by coherently driving the paramagnetic surface environment, *Phys. Rev. Lett.*, **123**, 146804, (2019)
2. Dolev Bluvstein, **Zhiran Zhang**, Ania C Bleszynski Jayich, Identifying and mitigating charge instabilities in shallow diamond nitrogen-vacancy centers, *Phys. Rev. Lett.*, **122**, 076101, (2019)
1. Xin Liu, **Zhiran Zhang**, Chaoyi Cai, Shibing Tian, Satya Kushwaha, Hong Lu, Takashi Taniguchi, Kenji Watanabe, Robert J Cava, Shuang Jia and Jian-Hao Chen, Gate tunable magneto-resistance of ultra-thin WTe_2 devices, *2D Mater.*, **4**, 021018, (2017)

Abstract

Probing and engineering the environment of near-surface nitrogen-vacancy centers in diamond for quantum sensing and simulation

by

Zhiran Zhang

Nitrogen-vacancy(NV) centers in diamonds are a prominent example of solid-state spin qubits for applications in quantum information. However, the assembly of solid-state spins, including NVs or auxiliary spins near the diamond surface, with a controlled nanoscale spatial precision remains an outstanding challenge. Consequently, the pathway towards scaling up both quantum simulation and entanglement-enhanced sensing using NVs remains unclear. Furthermore, near-surface NVs tend to exhibit degraded properties, including spin coherence and charge state stability [1, 2]. Firstly, we will discuss the charge state instabilities of shallow NVs [1]. We discover that the charge state stability depends on the local discrete environment, and our observation is consistent with a model of a single electron trap near the NV center. We also discuss protocols that can be used to alleviate the charge state effect on NV measurement. Secondly, we will discuss the utilization of entanglement with auxiliary reporter spins to improve the sensitivity of T_1 relaxometry [3]. Thirdly, we will discuss two methods to engineer two-dimensional NV ensembles and the decoherence dynamics due to the many-body noise in such strongly interacting dipolar spin systems [4]. Lastly, we will present our recent progress, where we combine a DNA-based patterning technique with nitrogen-vacancy (NV) quantum sensors in diamond to sense two-dimensional arrays of molecular spins programmably patterned via a monolayer of DNA origami on a diamond surface. We control the spacing of chelated Gd^{3+} spins down to 6 nm precision and verify this control by observing a

linear relationship between proximal NVs' T_1 relaxation rate and the designated number of Gd^{3+} spins per origami unit. We confirm the preservation of the charge state and spin coherence of the proximal, shallow NV centers and discuss ongoing work towards probing ordered, strongly interacting two-dimensional spin networks on the diamond surface.

Contents

Chapter 1

Introduction: Quantum sensing using nitrogen-vacancy centers in diamond

Isolated impurities, or defect centers, in solid state systems with a low density of nuclear spins can be treated in analogous to atom qubits in vacuum [5]. Quantum information can usually be encoded in the electron spin in the orbital ground state, leading to a variety of quantum information applications, including quantum computing, sensing, and communication [6, 7]. Defect centers here can refer to either single atom defects or atom-vacancy defects. The host materials that are commonly considered include diamond, silicon carbide, silion, and oxide with rare-earth dopants [6, 7]. Depending on the properties of these defect qubits and the host material, there may be advantages for specific applications or for the realization of a hybrid quantum platform. Examples include nitrogen-vacancy (NV) centers in diamond, silicon–vacancy and germanium–vacancy centers in diamond [8, 9], divacancy and silicon–vacancy in silicon carbide [10, 11, 12, 13], rare-earth ions in solids [14, 15, 16, 17, 6], and optically active donors in silicon [5, 18, 19, 20]. Particularly,

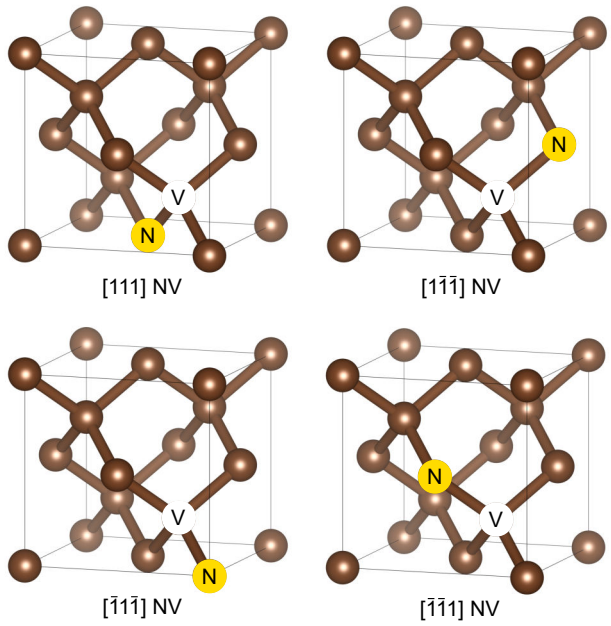

Figure 1.1: The structure of nitrogen-vacancy centers in cubic diamond lattice schematic. There are four possible NV axes, denoted as [111], [1$\bar{1}\bar{1}$], [$\bar{1}$1$\bar{1}$] and [$\bar{1}\bar{1}$1]. The atoms which are not marked are all carbon atoms. The diamond lattice is generated by the crystallographic software VESTA [21].

NV centers display long quantum coherence at room temperature, optical accessibility for initialization and readout, and functionality inside engineered nanostructures. This demonstrates their adaptability for use in quantum information technologies, including nanoscale sensing applications.

1.1 The nitrogen-vacancy centers in diamond

1.1.1 Crystal structure and Hamiltonian of NV center

Nitrogen-vacancy (NV) centers are atomic defects in diamond and are composed of a substitutional nitrogen atom plus a carbon vacancy at one of the nearest sites [22]. Thus an NV center has four possible orientations ([111], [1$\bar{1}\bar{1}$], [$\bar{1}$1$\bar{1}$] and [$\bar{1}\bar{1}$1]), all with a C_{3v} symmetry, as shown in the schematic of diamond cubic crystal structure in Fig.

1.1 [23]. The NV center has at least two known common charge states, NV^- and NV^0. Then negatively charged NV^- has been widely studied and applied for quantum technologies because of its unique electronic structure that allows optical polarization and spn-dependent readout, and we will refer to it as "NV" if not denoting the charge state. On the other hand, NV^- may be converted to unwanted NV^0 during manipulation which poses a challenge to many application [24, 25]. The NV^- defect has six electrons occupying the orbital states, where three electrons from nearby carbons, two from nitrogen itself, and one from a donor somewhere else in diamond. Therefore, NV^- has two unpaired electrons which give rise to the $S = 1$ ground and excited states.

The investigation of the NV center's electronic structure has lasted for the past several decades and remains to be an active field, including both theoretical and experimental research. In this dissertation, we will focus on a simplified spin state Hamiltonian at room temperature that is relevant for experiments demonstrated in this dissertation [23]. Other applications, for example sensing the local strain [26] or temperature [27] should consider a more detailed theory picture. Here we consider the electron spin of NV ($\mathbf{S}$) when coupled to the nitrogen nuclear spin ($\mathbf{I}$), which can be described by the following Hamiltonian [7]:

$$H = \underbrace{\mathbf{S}\cdot\mathbf{D}\cdot\mathbf{S}}_{\text{zero-field}} + \underbrace{\mu_B\mathbf{B}\cdot\mathbf{g}_{\text{nv}}\cdot\mathbf{S}}_{\text{electron Zeeman}} + \underbrace{\mathbf{S}\cdot\mathbf{A}\cdot\mathbf{I}}_{\text{hyperfine}} + ... \tag{1.1}$$

where $\mathbf{D}$ is the zero-field splitting (ZFS) tensor, $\mathbf{B}$ is the external magnetic field, $\mathbf{g}_{\text{nv}}$ is the g-factor tensor of NV, and $\mathbf{A}$ is the hyperfine coupling tensor. μ_B is the Bohr magneton. We have omitted the electrical interaction, nuclear spin Zeeman, and nuclear quadruple (only for ^{14}NV) terms here. Then when the z-axis is defined along the axis of the NV center, a phenomenological Hamiltonian of the NV ground state can be written

as [22, 28, 29]:

$$H = \underbrace{D(S_z^2 - \frac{S(S+1)}{3}) + E(S_x^2 - S_y^2)}_{\text{zero-field}} + \underbrace{\gamma_{\text{nv}}\mathbf{B}\cdot\mathbf{S}}_{\text{electron Zeeman}} + \underbrace{A_\parallel S_z I_z + A_\perp (S_x I_x + S_y I_y)}_{\text{hyperfine}} \tag{1.2}$$

where the first two ZFS terms originate from the dipole-dipole interaction [28]. The ZFS constant D is around 2.870 GHz at room temperature, and the temperature dependence of < 0.1 MHz/K can be ignored under our experiment condition [27]. E equals to zero if the lattice is perfect and the axial symmetry of NV center is retained [28]. A nonzero E can be caused by some nearby impurities or internal strain across the diamond sample, which breaks the axial symmetry of NV. E is typically zero to a few MHz in commercially available type 1b diamond [30], and experimentally, we apply an external magnetic field that causes a much larger Zeeman splitting, so this term can be ignored. In the electron Zeeman term, $\gamma_{\text{nv}} = g_{\text{nv}}\mu_B/\hbar$ is the gyromagnetic ratio of NV. The g-factor approximately equals to 2.0029(2) with a negligible anisotropy, which differs only slightly from free electrons [31]. The hyperfine parameters for ^{15}NV are $A_\parallel = 3.03(3)$ MHz and $A_\perp = 3.65(3)$, and for ^{14}NV parameters are $A_\parallel = -2.14(7)$ MHz and $A_\perp = -2.70(7)$ [31].

1.1.2 Energy diagram and Optical Detected Magnetic Resonance

The basic energy diagram of the NV center is shown in Fig. 1.2. The NV center ground state is a spin triplet denoted as $^3A_2$ and the excited state triplet as ^3E. The excited state is about 0.8(1) eV below the conduction band and 1.945 eV (637 nm) above the ground state [24, 32]. At room temperature, the zero phonon line (ZPL) of this emission is at 637 nm, while around 97% of the photon emission is through the

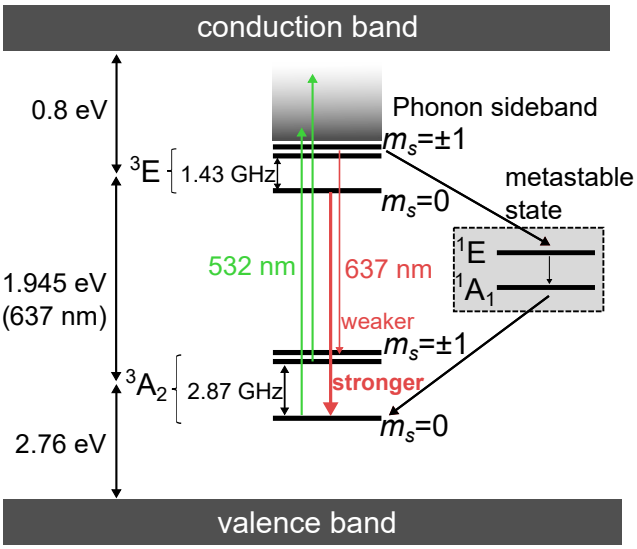

Figure 1.2: The simplified energy diagram of the negatively charged NV center and the optical paths most relevant for our NV experiments. Only the strong decay path through the metastable state is shown here.

phonon side-band near ^3E and $^3A_2$ instead of ZPL when NVs are in bulk diamond [33]. Importantly, there is a metastable singlet state due to spin-orbit and electron-phonon interactions as an alternative decay path other than the path directly from ^3E to $^3A_2$, (where the singlet is simplified from a pair of $^1A_1$ and ^1E states) [22, 34]. The decay rate through this metastable state does not have photon emission and is spin-dependent. The decay from $|m_s = \pm 1\rangle$ ^3E to metastable state and the decay from metastable to $|m_s = \pm 0\rangle$ $^3A_2$ are stronger than the other spin state path respectively, thus transferring the population from $|\pm 1\rangle$ to $|0\rangle$ [35]. This behavior is the central mechanism for the NV's optical detected magnetic resonance (ODMR).

Firstly, the NV center can be optically polarized at room temperature. The 532-nm laser is commonly used to polarize NV, but in principle, this can be done with a wide range of wavelengths [36]. At room temperature, if NV has stayed in the dark for a long enough time and is not disturbed, the NV will approximately be in the fully mixed ground state $^3A_2$ since 1.945 eV $\gg k_B T \gg hD$. The 532-nm photons first excite NV from the

ground state to the phonon side-band, and then NV undergoes the spin-dependent decay paths described above, resulting in an increase in $|m_s = 0\rangle$ population and a decrease of $|m_s = \pm 1\rangle$ population. Experimentally, the NV center can usually polarized to $|m_s = 0\rangle$ $^3A_2$ state with an approximately 80% population eventually after long enough 532-nm illumination [23].

Secondly, the spin state, m_s of $^3A_2$ can be measured optically. When an unpolarized NV is under the 532-nm illumination, if the duration of the 532-nm illumination is below a certain threshold, there will be a measurable photo-luminescence (PL) difference by collecting photons between the NV being initially in $|m_s = 0\rangle$ $^3A_2$ and $|m_s = \pm 1\rangle$ $^3A_2$ states. Then, after the 532-nm laser duration is long enough, the NV will be maximally polarized, and the spin-dependent PL will be zero. Experimentally, we typically only apply up to 400 ns of 532-nm laser pulse to optically measure the spin state, and for single NV without any fluorescence background, the PL of $|m_s = \pm 1\rangle$ after a long-pass filter at 637 nm will have 30%-35% less PL compared to $|m_s = \pm 0\rangle$ [37, 3].

Lastly, these behaviors of NVs are usually stable over a long time unless the charge state stability or other aspects of NVs have changed over the course of measurement, while many other fluorescent nano-materials, including quantum dots and fluorophores, are not as stable as NVs [23, 38]. Note that the shallow NV center is usually more easily affected by these detrimental effects, as the diamond surface is subject to chemical change and substances outside the lattice [24, 1, 39]. With these crucial properties described above, the NV center has a strong ODMR signal, which makes it a prominent quantum sensor.

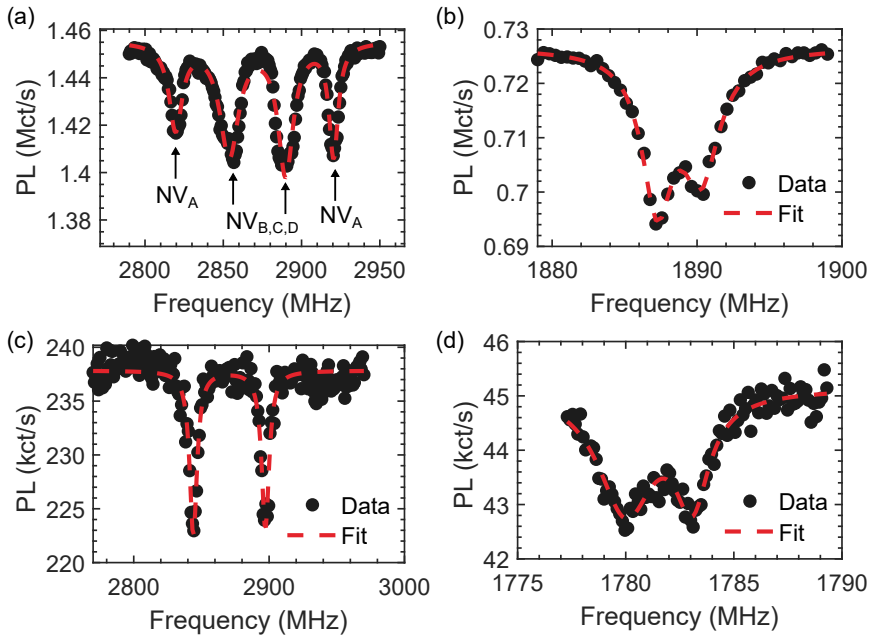

Figure 1.3: Examples of the CWESR measurement of NV ensemble and single NV. (a) CWESR of an NV ensemble. The red dashed line is the fit with Lorentzian functions. The external magnetic field is 18.4 G, aligned with one of the four NV axes, NV_A. The other three NV axes are $NV_{B,C,D}$. (b) CWESR of a ^{15}NV ensemble. The fit to two Lorentzian peaks are at 1887.24(3) MHz and 1890.26(4) MHz, so the difference agrees with the hyperfine parameter of $A_{\parallel} = 3.03(3)$ MHz for ^{15}N [31]. (c) CWESR of a single NV. The external magnetic field along the NV axis is 9.5 G, and the perpendicular field is 11.6 G. (d) CWESR of a single ^{15}NV. The fit to two Lorentzian peaks are at 1780.00(6) MHz and 1783.07(5) MHz, which agrees with the hyperfine parameter.

1.1.3 Continuous-wave ODMR measurement

Continuous-wave electron spin resonance (CWESR) refers to a type of ODMR measurement where the photons emitted from the NV are collected under continuous 532-nm illumination and continuous microwave with a sweeping frequency. This measurement is simple but powerful and can be used to quickly characterize the frequencies of transitions of all NVs that are located in the optical path. As shown in Fig. 1.3, the CWESR can be used to characterize both NV ensembles and single NVs. When measuring the NV ensemble, several NVs in the diamond are located near the center of the confocal beam spot, all contributing to the PL signal. Typically, in [100] diamond samples, where all four possible NV axes are $\arccos(1/\sqrt{3}) \approx 54.7^\circ$ relative to the [100] crystal orientation, there is no preferential alignment, meaning that four NV axes all have roughly same NV densities. Therefore, as shown in Fig. 1.3(a), the CWESR signal contains four peaks when the external B field is applied and aligned with one of the NV axes. As for a single NV or [111] diamond sample that has a strong preferential alignment, which means one of the NV axes is predominant, the CWESR spectrum contains only two peaks as shown in Fig. 1.3(c).

Furthermore, the CWESR can be used to detect the hyperfine splitting caused by nitrogen nuclear spin if using a low enough laser power and microwave power. The behavior of the CW/pulsed-ESR contrast and linewidth as a function of the microwave and laser pumping power is well measured and modeled in Ref. [40]. The CWESR usually has a worse sensitivity but is easier to implement in experiments. As shown in Fig. 1.3(b) and (d), ^{15}NV has two hyperfine lines since ^{15}N has a spin-1/2 nuclear spin and the splitting we measured agrees well with the hyperfine parameter $A_\parallel = 3.03(3)$ MHz for ^{15}N [31]. As for ^{14}NV, there will be three hyperfine lines since ^{15}N has a spin-1 nuclear spin, and the splitting will be $A_\parallel = 2.14(7)$ MHz.

1.2 Quantum sensing pulse sequence

Most studies and sensing applications of NVs require controlling the NV by microwave driving pulses and sensing the external magnetic field, which can be understood and modeled by examining the electron Zeeman term in the Hamiltonian of the NV qutrit more closely. The spin operator $\mathbf{S}$ in principle should be a spin-1 operator, but in many pulse sequences, NV center is treated as a qubit by only addressing a subspace of $|0\rangle$ plus either $|+1\rangle$ or $|-1\rangle$. For simplicity, we treat the NV ground state as a qubit in the following discussion and assume the microwave control drive is not strong enough to address the other spin state, which is not resonant with the microwave.

For an NV subjected to a time-dependent external magnetic field, $\mathbf{B}(t) = B_0\hat{\mathbf{z}}+\mathbf{B}_1(t)$, where the $\hat{\mathbf{z}}$ is chosen to be along the NV axis. The interaction with such a magnetic field can be written as

$$H(t) = \gamma_{\mathrm{nv}}\left[\frac{(B_{1,x}(t) - iB_{1,y}(t))\hat{S}_+}{2} + \frac{(B_{1,x}(t) + iB_{1,y}(t))\hat{S}_-}{2}\right] + \gamma_{\mathrm{nv}}(B_0 + B_z(t))\hat{S}_z, \quad (1.3)$$

where $\hat{S}_\pm$ are the raising and lowering operators, γ_{nv} is the NV's gyromagnetic ratio. The first term implies how the transverse component of a microwave magnetic field can drive the spin state resonantly.

1.2.1 Rotating frame and Rabi oscillation

As an example, under the rotating wave approximation, we consider a continuous-wave microwave field perpendicular to the NV axis to be used to drive the Rabi oscillation of the NV ground state transitions, where $B_{1,x}(t) = B_1\cos(\omega t)$, $B_{1,y}(t) = B_1\sin(\omega t)$, and $B_{1,z}(t) = 0$. Then, this time-dependent term in the Hamiltonian becomes time-independent by going to the rotating frame, which has the same frequency ω as the NV

transition. The transformation operator to the rotating frame is

$$\hat{U}(t) = \exp\left(\frac{i\omega\hat{\sigma}_z t}{2}\right), \tag{1.4}$$

where $\hat{\sigma}_z$ is the Pauli operator. The Hamiltonian after the unitary transformation into the rotating frame can then be written as,

$$\tilde{H} = i\hbar\left(\frac{\partial\hat{U}(t)}{\partial t}\right)\hat{U}^\dagger(t) + \hat{U}(t)H(t)\hat{U}^\dagger(t). \tag{1.5}$$

Then by substituting Eq. (1.3) and Eq. (1.4) into it, we end up with the time-independent Hamiltonian in the rotating frame

$$\tilde{H} = \left(\frac{\gamma_{\mathrm{nv}}\hbar B_0}{2} - \frac{\hbar\omega}{2}\right)\hat{\sigma}_z + \frac{\gamma_{\mathrm{nv}}\hbar B_1\hat{\sigma}_x}{2}. \tag{1.6}$$

Also, note that the NV center has a ZFS and such term can be combined with the external field along NV axis B_0, so now B_0 corresponds to the actual transition frequency of the NV qubit. For example, under a nonzero external static field $B_{\mathrm{ext}} < 500$ G that we usually apply along the NV axis in our experiments, $\gamma_{\mathrm{nv}}B_0 = \pm\gamma_{\mathrm{nv}}B_{\mathrm{ext}} + D$ depending on the subspace chosen for the NV to be considered as a qubit. As a convention, we define $\Delta = \gamma_{\mathrm{nv}}B_0 - \omega$ as the detuning of the Rabi oscillation and $\Omega = \gamma_{\mathrm{nv}}B_1$ as the Rabi frequency. And clearly, when the microwave pulse has a frequency perfectly matched to the actual qubit transition $\gamma_{\mathrm{nv}}B_0$, the detuning Δ becomes zero. Now the time evolution operator in the rotating frame is,

$$\tilde{U}(t) = \cos\left(\frac{\tilde{\Omega}t}{2}\right) - \frac{i(\Delta\hat{\sigma}_z + \Omega\hat{\sigma}_x)}{\tilde{\Omega}}\sin\left(\frac{\tilde{\Omega}t}{2}\right), \tag{1.7}$$

where the so-called generalized Rabi frequency is $\tilde{\Omega} = \sqrt{\Delta^2 + \Omega^2}$. With such a time evolution operator, we can finally derive the spin state of a polarized NV at time t in the rotating frame,

$$\begin{aligned} |\tilde{\Psi}(t)\rangle &= \tilde{U}(t)\,|0\rangle \\ &= \left[\cos\left(\frac{\tilde{\Omega}t}{2}\right) - \frac{i\Delta}{\tilde{\Omega}}\sin\left(\frac{\tilde{\Omega}t}{2}\right)\right]|0\rangle - \frac{i\Omega}{\tilde{\Omega}}\sin\left(\frac{\tilde{\Omega}t}{2}\right)|-1\rangle\,. \end{aligned} \tag{1.8}$$

Here, we assume the NV qubit is utilizing the subspace of $|-1\rangle$ and $|0\rangle$. When the detuning is zero, we have a simple oscillating spin state as

$$|\tilde{\Psi}(t)\rangle = \cos\left(\frac{\Omega t}{2}\right)|0\rangle - i\sin\left(\frac{\Omega t}{2}\right)|-1\rangle\,. \tag{1.9}$$

1.2.2 Bloch sphere

Now, notice that this time evolution operator acting on the spin state is analogous to a rotation operator acting on a vector. Bloch vector can be applied to help visualize the time evolution of the spin state. For a spin state of

$$|\Psi\rangle = \cos\left(\frac{\theta}{2}\right)|0\rangle + \sin\left(\frac{\theta}{2}\right)e^{i\phi}|-1\rangle\,, \tag{1.10}$$

the Bloch vector is defined as the expectation values of the Pauli matrices. Therefore, we have $\langle\hat{\sigma}_x\rangle = \sin(\theta)\cos(\phi)$, $\langle\hat{\sigma}_y\rangle = \sin(\theta)\sin(\phi)$, and $\langle\hat{\sigma}_z\rangle = \cos(\theta)$, which are the x, y and z components of the unit Bloch vector on Bloch sphere. Therefore, the initial polarized spin is along the z-axis of the Bloch sphere, $(\langle\hat{\sigma}_x\rangle, \langle\hat{\sigma}_y\rangle, \langle\hat{\sigma}_z\rangle) = (0, 0, 1)$. Then after the Rabi oscillation, now the vector becomes $(0, -\sin(\Omega t), \cos(\Omega t))$. So clearly, this microwave of $\mathbf{B} = (B_1\cos(\omega t), B_1\sin(\omega t), 0)$ is rotating the Bloch vector along +x axis at the frequency Ω.

More generally, the microwave of a different phase will result in a similar time evolution of spin state and can also be described by the Bloch sphere picture. If the microwave field is written as $\mathbf{B} = (B_1 \cos(\omega t + \phi_0), B_1 \sin(\omega t + \phi_0), 0)$, then the Bloch vector is rotated by an angle of $\theta = \Omega t = \gamma_{\mathrm{nv}} B_1 t$, along the direction of $\hat{\mathbf{n}} = (\cos(\phi_0), \sin(\phi_0), 0)$ which is on the xy plane.

For our experiments, microwave pulses can start with an arbitrary phase, corresponding to driving the NV along different axes on the Bloch sphere. The microwave pulses with $\phi_0 = 0$, π, $\pi/2$, or $3\pi/2$ are called +X, -X, +Y, -Y pulses, respectively, since they correspond to rotation along those axes on the Bloch sphere. For example, a microwave pulse with $\phi_0 = 0$ and $\Omega t = \pi$ is called a +X π pulse, and a microwave pulse with $\phi_0 = \pi/2$ and $\Omega t = \pi/2$ is called a +Y $\pi/2$ pulse. In a nutshell, the ideal microwave pulses in the rotating frame are equivalent to rotating the Bloch vector by Ωt along a certain axis defined by ϕ_0.

1.2.3 Phase accumulation during free precession time

One more important and relevant aspect of the sensing pulse sequence is the evolution of the spin vector under a small time-dependent magnetic field when there are no microwave pulses that control the spin (which is also called free precession time). In the rotating frame, the time-dependent external magnetic field $\mathbf{B}_1(t)$ now becomes an effective magnetic field of

$$\begin{aligned}\tilde{\mathbf{B}}(t) = (B_{1,x}(t)\cos(\omega t) + B_{1,y}(t)\sin(\omega t), -B_{1,x}(t)\sin(\omega t) + B_{1,y}(t)\cos(\omega t) \\ , B_0 + B_{1,z}(t) - \frac{\omega}{\gamma_{\mathrm{nv}}}).\end{aligned} \tag{1.11}$$

The external field $\mathbf{B_1}(t)$ to be detect by NV usually is oscillating at a much smaller frequency compared to ω, and has a small amplitude. Therefore, the x and y components

will quickly be averaged to zero, and only the z component becomes measurable. If not considering the NV's hyperfine splitting, and also assuming the detuning of the rotating frame is zero, then the time evolution unitary operator becomes approximately

$$\tilde{U}(t) = \exp\left(-\frac{-i\gamma_{\mathrm{nv}}}{2}\left[\int_0^t B_{1,z}(\tau)d\tau\right]\tilde{\sigma}_z\right). \tag{1.12}$$

Translating to rotation on the Bloch sphere, this equals a rotation along the +z axis for a phase accumulation of

$$\phi(t) - \phi(0) = \gamma_{\mathrm{nv}}\int_0^t B_{1,z}(\tau)d\tau. \tag{1.13}$$

This is the central idea behind using NV as a magnetometer to sense AC coherent magnetic fields. Now we may also consider the hyperfine splitting. For example, for ^{14}NV, if the detuning from the center hyperfine line is Δ, then in each 1/3 of experiment shots, there will be an extra phase accumulation at three different frequencies of $\Delta - A_{\parallel}$, Δ, and $\Delta + A_{\parallel}$, where $A_{\parallel} = 2.14(7)$ MHz.

1.2.4 Observable and readout of NV center

The observable quantity for NV qubit is the PL which is proportional to the population of $|0\rangle$ state of the NV (the diagonal element for $|0\rangle$ state in the density matrix). For example, after a Rabi oscillation (Eq. 1.9) with a nonzero detuning we have

$$\rho_0(t) = |\langle 0|\Psi\rangle|^2 = |\langle 0|\tilde{\Psi}\rangle|^2 = \left|\cos\left(\frac{\tilde{\Omega}t}{2}\right) - \frac{i\Delta}{\tilde{\Omega}}\sin\left(\frac{\tilde{\Omega}t}{2}\right)\right|^2 = 1 - \left(\frac{\Omega}{\tilde{\Omega}}\right)^2\sin^2\left(\frac{\tilde{\Omega}t}{2}\right) \tag{1.14}$$

Here we also present a phenomenological model for the PL readout. We represent the population of NV^- as ρ^-. Assuming no other charge state other than NV^0 exists, the

population of NV^0 can be denoted as $1-\rho^-$. The PL from $|+1\rangle$ and $|-1\rangle$ of the ground state are approximately the same when the energy levels in both ground state and excited state manifolds are far away from $|0\rangle$. Thus for a single NV, we have

$$\mathrm{PL} = \mathrm{PL}_0^- \rho_0 + \mathrm{PL}_{\pm1}^- \rho_{-1} + \mathrm{PL}_{\pm1}^- \rho_{+1} + \mathrm{PL}^0(1-\rho^-), \tag{1.15}$$

where PL_0^- and $\mathrm{PL}_{\pm1}^-$ are the PL of $|0\rangle$ and $|\pm1\rangle$ respectively, and PL^0 is the PL of NV^0 which is usually lower than $\mathrm{PL}_{\pm1}^-$. For Rabi oscillation, plug Eq. (1.14) into it, we have

$$\begin{aligned}\mathrm{PL}(t) = \mathrm{PL}_0^- \left[1 - \left(\frac{\Omega}{\tilde{\Omega}}\right)^2 \sin^2\left(\frac{\tilde{\Omega}t}{2}\right)\right] + \mathrm{PL}_{\pm1}^- \left[\rho^-(t) - 1 + \left(\frac{\Omega}{\tilde{\Omega}}\right)^2 \sin^2\left(\frac{\tilde{\Omega}t}{2}\right)\right] \\ + \mathrm{PL}^0(1-\rho^-(t)).\end{aligned} \tag{1.16}$$

Now if we further assume the charge state is stable over the time scale of Rabi oscillation here, $\rho^-(t)$ becomes a constant, and the PL is

$$\mathrm{PL}(t) = \left(\mathrm{PL}_0^- - \mathrm{PL}_{\pm1}^-\right)\left[1 - \left(\frac{\Omega}{\tilde{\Omega}}\right)^2 \sin^2\left(\frac{\tilde{\Omega}t}{2}\right)\right] + \left[\mathrm{PL}_{\pm1}^- \rho^- + \mathrm{PL}^0(1-\rho^-)\right]. \tag{1.17}$$

The Rabi oscillation with a near zero detuning is measured by the pulse sequence shown in Fig.1.4. Since we are mostly interested in the Rabi frequency $\tilde{\Omega} \approx \Omega$ and there may be some extra delay when turning on the microwave pulse, the data can be fitted with

$$\mathrm{PL}(t) = c_1 \exp(-t/T_2^*) \cos\left(\Omega(t+t_0)\right) + c_2, \tag{1.18}$$

where c_1 and c_2 are two free parameters to be fitted, and decay associated with T_2^* is typically due to the spin dephasing and relaxation during the pulse sequence or the inhomogeneous environment of NV ensemble, which also causes the broadening of ESR

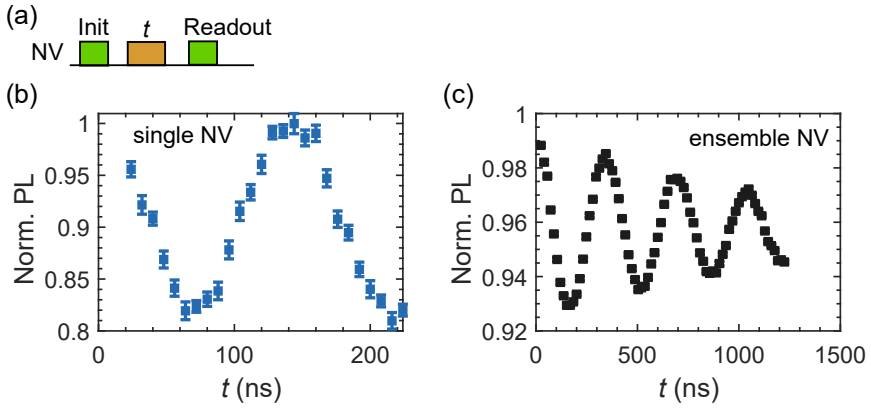

Figure 1.4: The Rabi oscillation of a single NV and an NV ensemble. (a) The pulse sequence of a Rabi oscillation measurement consists of an initialization 532-nm laser pulse (2000 ns), followed by a microwave pulse with duration t, and the readout 532-nm laser pulse (400 ns). (b) Rabi oscillation of a single NV. The PL has been normalized by the PL value right after initialization. (c) Rabi oscillation of an NV ensemble. Both sets of data are taken from [111] diamond samples with different NV densities.

peaks as we will discuss in the following sections.

1.2.5 Modeling the ideal pulse sequence

We have discussed the basic elements to understand most sensing pulse sequences we use for measuring NV centers. Assuming microwave and laser pulses are ideal, a simple workflow can be used to derive the final measurable signal, which is proportional to ρ_0. The microwave pulses being ideal means that the decoherence during the time of pulses is negligible, the parameters are accurate enough to rotate the spin to the exact superposition intended, and these properties are stable over different shots. As an example, the Ramsey Free Induction Decay pulse sequence (FID) can be analyzed using the following steps. As shown in Fig. 1.7(d), Ramsey sequence is

$$\text{Initialization - } \left(\frac{\pi}{2}\right)_{+\text{X}} \text{ - } \tau \text{ - } \left(\frac{\pi}{2}\right)_{+\text{X}} \text{ - Readout.} \tag{1.19}$$

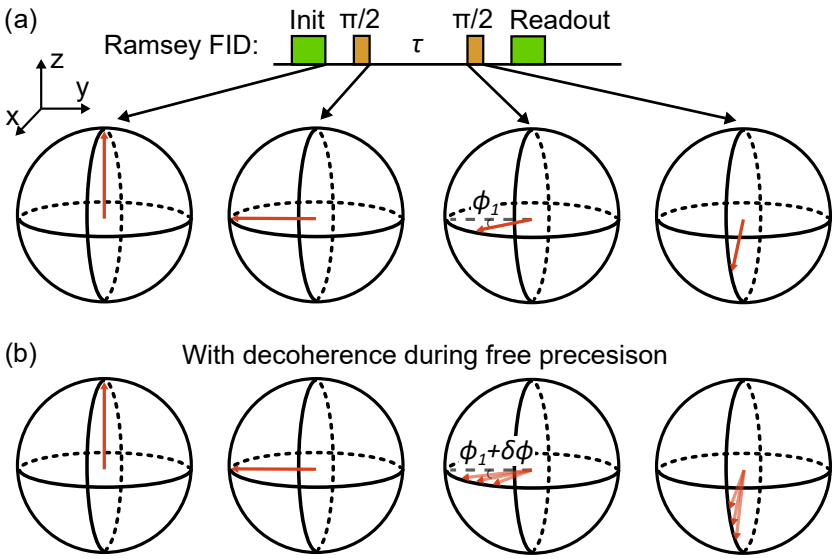

Figure 1.5: The Bloch sphere representation of the evolution of spin state in a Ramsey Free Induction Decay (FID) pulse sequence. (a) The Ramsey pulse sequence and the Bloch sphere representation assuming there is no decoherence during the free precession time τ except ϕ_1 from the the ac signal. The four Bloch spheres represent the spin vector after initialization, after the first $\pi/2$ pulse, after the free precession time τ, and after the second $\pi/2$ pulse, respectively. (b) The Bloch sphere representation if also considering the phase accumulation $\delta\phi$ caused by decoherence during free precession.

After the initialization, assume the NV has a pure $|0\rangle$ state. In the

$$|\tilde{\Psi}\rangle_0 = \begin{pmatrix} 1 \\ 0 \end{pmatrix}. \tag{1.20}$$

Then based on Eq. (1.7), the manipulations of NV, including the free precession time, can also be written as the matrices as follows,

$$\mathcal{R}(\phi, n_x, n_y, n_z) = \begin{pmatrix} \cos(\frac{\phi}{2}) - in_z \sin(\frac{\phi}{2}) & (-in_x - n_y)\sin(\frac{\phi}{2}) \\ (-in_x + n_y)\sin(\frac{\phi}{2}) & \cos(\frac{\phi}{2}) + in_z \sin(\frac{\phi}{2}) \end{pmatrix}. \tag{1.21}$$

Therefore, the first +X $\pi/2$ pulse is represented by $\mathcal{R}_1(\pi/2, 1, 0, 0)$, the phase accumulation of ϕ_1 during free precession time is $\mathcal{R}_2(\phi_1, 0, 0, 1)$, and the second +X $\pi/2$ pulse is $\mathcal{R}_3$. The spin state after these manipulations and free precession is

$$|\tilde{\Psi}\rangle = \mathcal{R}_3\mathcal{R}_2\mathcal{R}_1 |\tilde{\Psi}\rangle_0 . \tag{1.22}$$

The final readout PL will be proportional to $\rho_0 = |\langle 0|\tilde{\Psi}\rangle|^2 = \sin^2(\phi_1/2)$. Bloch sphere can also help visualize the evolution of the spin state in a rotating frame as illustrated in Fig. 1.5. As mentioned earlier in section 1.3.2, the unitary time evolution operators here are equivalent to rotation operators for the Bloch vector. Now considering that a time-dependent magnetic field noise bath gives random phase contribution to $\delta\phi(\tau)$ and causes decoherence, we denote the final signal after averaging over all shots of measurement as

$$C(\tau) = \langle \rho_0 \rangle = \left\langle \sin^2\left(\frac{\phi_1 + \delta\phi}{2}\right) \right\rangle. \tag{1.23}$$

1.3 Spin relaxation and T_1

The spin relaxation, also known as the longitudinal relaxation or spin-lattice relaxation in the realms of nuclear magnetic resonance (NMR) and magnetic resonance imaging (MRI), is the decoherence process of a spin in which the energy is not conserved. Even when the spin is polarized, in the spin relaxation, the spin will evolve towards the thermal equilibrium. For NVs at room temperature, we approximately have $\rho_0 = \rho_{-1} = \rho_{+1} = 1/3$. Here, we assume that the NV is not subject to a large strain, a perpendicular external magnetic field, or an electric field. T_1 denotes the time scale when the polarization drops to 1/e of the original value.

The relaxation mechanisms at room temperature may include (1) the two-phonon Raman processes where a phonon is in-elastically scattered, leaving the spin in a different energy state and emitting a phonon [41]; (2) spin-spin cross relaxation if an NV's transition is in resonance with other spins, for example NVs of other orientations, or substitutional nitrogen (P1 centers); [42, 43]; or (3) magnetic noise which has a strong spectra density at the NV transition frequency [44, 45, 46]. The use of NV center T_1 to sense magnetic noise at NV transition frequency is often referred to as NV T_1 relaxometry.

Since the NV center is a spin triplet, the model of spin relaxation is complex if considering all three possible transitions between individual sublevels shown in Fig. 1.6 [47]. Here we only present the model when the pulse sequence starts with a perfectly polarized NV, and there is no charge state instability, and we have $\Omega_- = \Omega_+$, $\rho_{-1}(t) = \rho_{+1}(t)$. There will be a more detailed discussion later in Chapter 6. Using the pulse sequence shown in Fig. 1.6(b), the first signal is a direct readout, and the second signal has a resonant microwave pulse to swap the ρ_{-1} and ρ_0 right before the readout,

$$\mathrm{PL}(t) = \mathrm{PL}_0^- \rho_0(t) + \mathrm{PL}_{\pm 1}^- \rho_{-1}(t) + \mathrm{PL}_{\pm 1}^- \rho_{+1}(t), \tag{1.24}$$

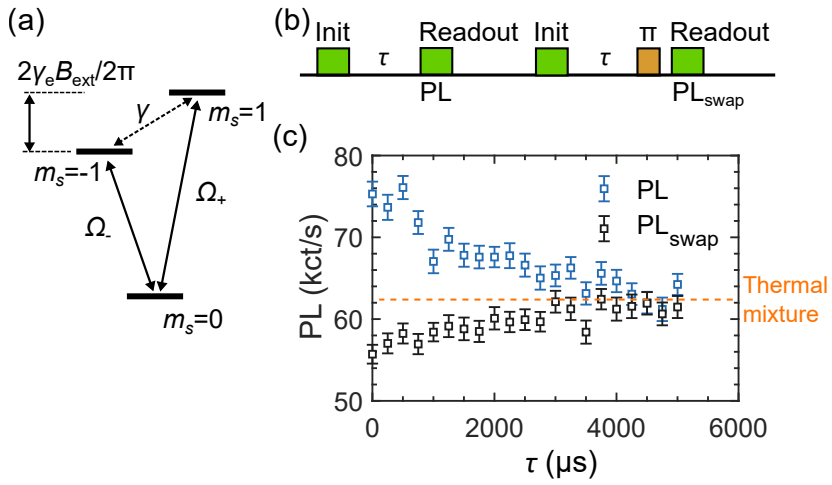

Figure 1.6: The T_1 relaxometry of a single NV. (a) The energy diagram of the NV ground state and the relaxation rates between each pair of sublevels. (b) The pulse sequence of a differential T_1 relaxation measurement. (c) The relaxation signal of a single NV using the pulse sequence in (b). Here the microwave π pulse is driving the $|0\rangle \leftrightarrow |-1\rangle$ transition. The approximate PL level of the thermal mixture is marked by the orange dashed line.

$$\mathrm{PL}_{\mathrm{swap}}(t) = \mathrm{PL}_0^- \rho_{-1}(t) + \mathrm{PL}_{\pm 1}^- \rho_0(t) + \mathrm{PL}_{\pm 1}^- \rho_{+1}(t), \tag{1.25}$$

where PL_0^-, $\mathrm{PL}_{\pm 1}^-$ are the PL of different NV^- spin states. After the spin has fully relaxed to the thermal mixture, we have

$$\mathrm{PL}(\infty) = \mathrm{PL}_{\mathrm{swap}}(\infty) = \frac{2}{3}\mathrm{PL}_{\pm 1}^- + \frac{1}{3}\mathrm{PL}_0^- \tag{1.26}$$

Therefore as shown in Fig. 1.6(c), the PL of thermal mixture level should be higher than PL_0^- by 1/3 of the difference between PL_0^- and $\mathrm{PL}_{\pm 1}^-$. The final differential PL signal can be written as

$$\mathrm{PL}_{\mathrm{diff}}(t) = \mathrm{PL}(t) - \mathrm{PL}_{\mathrm{swap}}(t) = (\mathrm{PL}_0^- - \mathrm{PL}_{\pm 1}^-)(\rho_0(t) - \rho_{-1}(t)) = (\mathrm{PL}_0^- - \mathrm{PL}_{\pm 1}^-)e^{-3\Omega t}, \tag{1.27}$$

where $\Omega = \Omega_- = 1/3T_1$. At room temperature, a T_1 of 3-6 ms can usually be achieved for bulk NV centers, while at low temperature, the T_1 can approach 250 ms both in theory

and experiment [41, 48, 49]. As for shallow NV centers, we usually observe T_1 around 3 ms at room temperature.

1.4 Spin dephasing and T_2^*

The spin dephasing is the decoherence process where the phase of the quantum state ϕ loses its definite value and becomes random. In the picture of the Bloch sphere, it is the process that the spin vector has an indefinite angle ϕ with respect to the fixed xy plane. The dephasing time T_d measures the time scale of dephasing to have 1/e of the original full coherence. Therefore, spin dephasing is completely a different process from spin relaxation, and both dephasing and relaxation can contribute to quantum decoherence. The pure spin dephasing process is usually difficult to measure separately in the presence of spin relaxation. In practice, several methods can be used to characterize the inhomogeneous decoherence time T_2^* of NV, which is the free precession time after which the qubit superposition's coherence decays to 1/e. For shallow NV center at room temperature, usually $T_d \ll T_1$, so we have $T_2^* \approx T_d$. T_2^* is an important property of an NV because it affects the NV's sensitivity for magnetometry of DC fields.

As suggested by Eq.(1.13), any source of the magnetic field can become a source of dephasing, which may include ^{13}C nuclear spins, P1 centers, surface spins, other defect centers, and so on [50, 47, 24]. The exact origin of surface spins is an interesting question and has been a long debate. These unpaired g=2 S-1/2 dark spins often have sizable contributions to the decoherence of shallow NVs [39, 51, 52]. There are recent studies showing that it is the primal sp2 defects on the diamond surface (not the dangling bonds), and the density estimation of 0.001-0.1 nm^{-2} is consistent with many other experiments, including ours [51, 2].

To measure the inhomogeneous linewidth and characterize T_2^*, the so-called pulsed

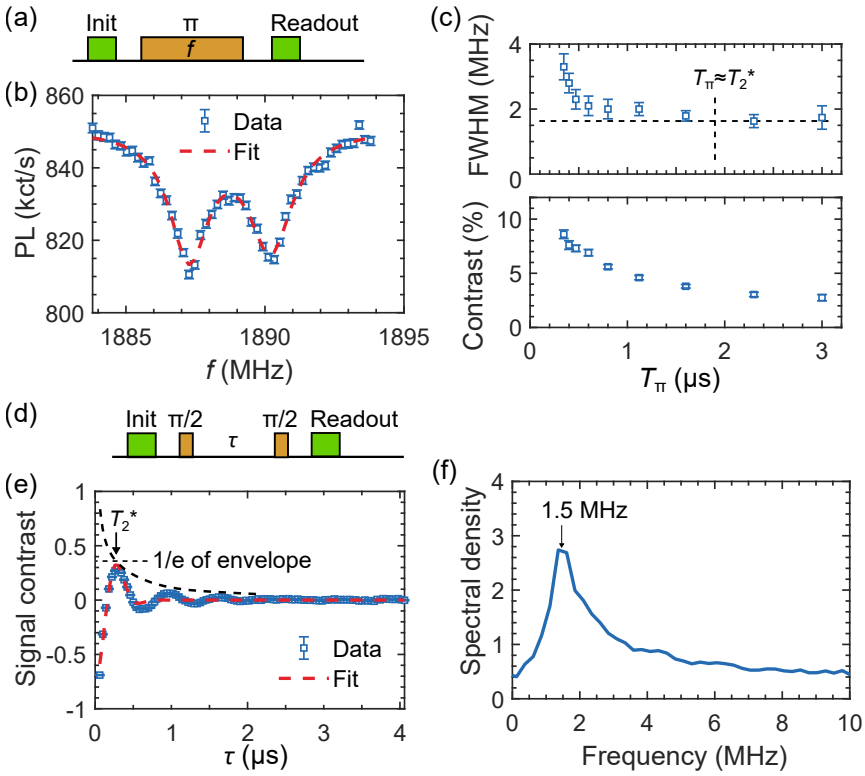

Figure 1.7: The pulsed ESR and Ramsey measurement of NV ensemble in [111] diamond sample. (a) The pulse sequence of pulsed ESR measurement. (b) The pulsed ESR signal of a ^{15}NV ensemble. The π pulse duration is 1600 ns. The dashed line is a fit with two Lorentzian peaks. The extracted linewidths are 1.70(8) MHz and 1.89(9) MHz, and the splitting is 2.94(3) MHz. The external magnetic field is 351.4 G and aligned to the NV axis within an angle of 3°. (c) The dependence of linewidth and signal contrast on the π pulse duration T_π. (e) The pulse sequence of the Ramsey measurement. (f) The Ramsey fringe when the $\pi/2$ pulses drive at the center frequency of the hyperfine lines. (g) The Fourier transform of the Ramsey fringe.

ESR measurement is often employed to mitigate the optical and microwave broadening in the CWESR measurement as mentioned previously. The pulse sequence of this measurement is shown in Fig. 1.7(a). The relationship between $1/T_2^*$ and the linewidth depends on the type of noise bath that dominates the shape of the resonance line. For a single NV, assume each hyperfine line follows a Gaussian distribution

$$\mathrm{P}(\eta') = \frac{1}{\sigma\sqrt{2\pi}} \exp\left[-\frac{(\eta' - \eta_i)^2}{2\sigma^2}\right], \tag{1.28}$$

where η_i is the average frequency of hyperfine lines. For ^{15}NV, we have $\eta_2 - \eta_1 = 3.0$ MHz. Now based on the Eq. (1.23), we obtain the coherence decay form in Ramsey measurement,

$$\begin{aligned} C(t) &= \left\langle \frac{1 - \cos(\phi_1 + \delta\phi)}{2} \right\rangle = \frac{1}{2} - \frac{1}{2}\sum_{i=1}^{N} A_i \left\langle \cos(\phi_1 + \delta\phi) \right\rangle \\ &= \frac{1}{2} - \frac{1}{2}\sum_{i=1}^{N} A_i \int_{-\infty}^{\infty} \mathrm{P}(\eta') \cos(\eta' t) d\eta' \\ &= \frac{1}{2} - \frac{1}{2}\sum_{i=1}^{N} A_i \exp\left(-\frac{t^2}{2/\sigma^2}\right) \cos(\eta_i t), \end{aligned} \tag{1.29}$$

where $N = 2$ for ^{15}NV and $N = 3$ for ^{14}NV. (We will revisit this problem in the next section for a more general approach using the filter function.) We note that the envelope of this signal is $\exp(-(t/T_2^*)^2)$ and we have $T_2^* = \sqrt{2}/\sigma$, where σ is the standard deviation of the resulting Gaussian peaks in pulsed ESR. But different NV systems may have different spin bath characteristics, yielding interesting distinct features in pulsed ESR and Ramsey measurement that we do not fully understand yet. For example, in our pulsed ESR measurement of NV ensemble in a [111] diamond, as shown in Fig. 1.7, the signal fits better with two Lorentzian functions with FWHM of $2\gamma = 1.8(1)$ MHz. The dependence of 2γ and T_π does show with saturation to around 1.8 MHz near around

$T_\pi \approx T_2^*$ [40]. If still adopting the Gaussian noise bath model, this corresponds to a T_2^* of 1.9(1) μs.

Furthermore, the Ramsey pulse sequence can also be employed to characterize T_2^*. This pulse sequence has been discussed previously in section 1.3.5 and is useful to sense AC signals. Because of the hyperfine coupling to ^{15}N nuclear spin, the Ramsey without any extra ac signal will show oscillation at the frequencies of $\Delta - A_\parallel/2$ and $\Delta + A_\parallel/2$. As shown in Fig. 1.7(e), a fit to the Ramsey signal with $A\exp(-(t/T_2^*)^2)\cos(\omega t)$ yields $T_2^* = 0.34(2)$ μs and $\omega = 2\pi \times 1.56(3)$ MHz. Interestingly, we notice that the fit is not ideal with the stretch power of 2. Then we performed a Fourier transform of the Ramsey signal and we observed an asymmetric peak with a FWHM around 1.6 MHz. This observation may be related to the assumptions of the noise bath or the inhomogeneity of the NV ensemble and needs further investigation.

1.5 Mitigating spin dephasing by Hahn echo and dynamical decoupling

The Ramsey measurement is not ideal for sensing AC signals due to several reasons. Firstly, for NV centers, the hyperfine coupling to nitrogen nuclear spins is not avoidable, and those oscillations in the Ramsey signal will interfere with the detection of the target signal. Secondly, the T_2^* is often short, and the Ramsey sequence does not manipulate the spin to mitigate magnetic noise. For example, the T_2^* can be affected by long-term drift of temperature or magnetic field in the laboratory. To reach $T_2^* \approx$100 μs, one needs at least a temperature stability on the order of 0.2 K and magnetic field stability on the order of $\sqrt{2}/\gamma_e T_2^* \approx 5 \times 10^{-3}$ Gauss. Dynamical decoupling sequences, which are adopted from the field of high-resolution NMR, can be applied to solid-state spin qubits to manipulate

the spin states of both the qubit and the environment spin bath [53, 54]. Such a method not only mitigates the dephasing caused by noise and improves the coherence time of the spin qubit but is also useful for sensing since it leaves a narrower window in the filter function so that the NV essentially becomes a spectrometer for detecting the target field signals [55].

To further examine the function of the dynamical decoupling sequence, we can analytically model the statistics of the phase accumulation in Eq. (1.23) and take a step forward to derive the formula for coherence averaged over different measurement shots. In many cases of interest, the noise bath cannot be simply modeled by delta functions in the frequency domain. Instead, one could assume the noise amplitude follows a Gaussian distribution and model the dephasing in the pulse sequence by using the filter function. This also provides a useful perspective of sensing the environment as a spectrometer [55]. A small perturbing field to the NV center couples to the NV ground state. So the simple Hamiltonian considered here is just the same as Eq. (1.11), and in the rotating frame, we only need to consider a term of $\hat{\eta}_z\sigma_z$, where $\hat{\eta}_z$ is the noise bath contribution to the time-dependent field at the NV location. Following derivation in Ref. [55], we assume $\langle\hat{\eta}_z(\tau)\rangle = 0$ since any dc component of this noise field can be written into the time-independent B_0 term in Eq. (1.11). If the central limit theorem stands for the problem, we have a Gaussian distribution noise again,

$$\mathrm{P}[\hat{\eta}_z(t) = \eta'] = \frac{1}{\sigma\sqrt{2\pi}} \exp\left(-\frac{-\eta'^2}{2\sigma^2}\right), \tag{1.30}$$

where the time-independent variance is $\sigma^2 = \langle\hat{\eta}_z^2(t)\rangle$. Here, the noise amplitude is Gaussian, which does not necessarily mean the noise spectrum is Gaussian. Instead, $\eta'(t)$ corresponds to a classical random variable and measures the experiment results in every shot of the pulse sequence. The noise spectrum refers to the Fourier transform of the cor-

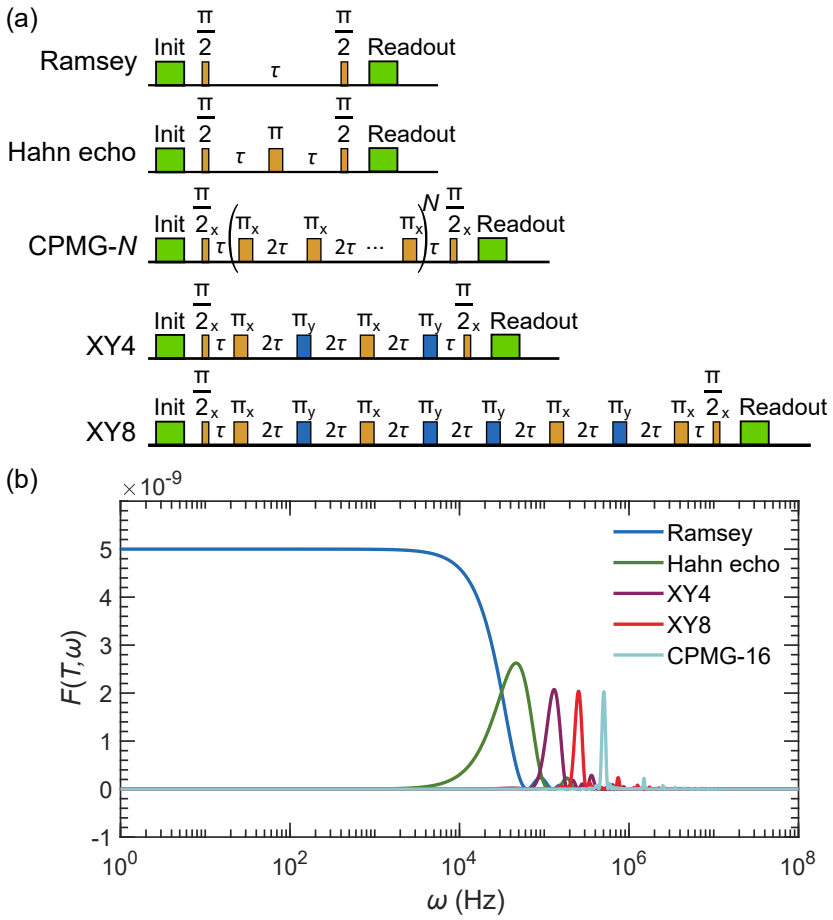

Figure 1.8: Most used pulse sequences and corresponding filter functions. (a) The schematic of the Ramsey, Hahn echo, CPMG, XY4, and XY8 pulse sequences. (b) The filter functions $\mathcal{F}$ of these pulse sequences as a function of free precession time and frequency. Here we fix the total free precession time to be $T = 100$ μs. So the value for τ in each pulse sequence is different from the others. The filter functions of XY4 and XY8 are the same as CPMG-4 and CPMG-8, respectively. Clearly, only the Ramsey sequence can sense the noise at dc or low frequencies. With more π pulses in the dynamical decoupling sequence, the filter function will be narrower, and the peak frequency will be higher if keeping T fixed.

relation function of $\eta'(t)$, which is $\langle \eta'(t)\eta'(t+T)\rangle$. The coherence envelope, by averaging over all noise trajectories, is [55]

$$C(t) = \mathrm{Tr}(\hat{\sigma}_+\rho(t)) = \exp\left[-\int_{-\infty}^{\infty} \tilde{S}(\omega)\mathcal{F}(t,\omega)d\omega\right] \tag{1.31}$$

where $\hat{\sigma}_+ = \hat{\sigma}_x + \hat{\sigma}_y$ is the spin raising operator of the chosen NV ground state subspace, $\rho(t)$ is the density matrix, and $\tilde{S}(\omega)$ is the noise spectrum. $\mathcal{F}(t,\omega)$ is the filter function that depends on the exact pulse sequence between those two $\pi/2$ pulses, which is defined as

$$\mathcal{F}(t,\omega) = \int_0^{\tau} dt' s(t') \int_0^{t'} dt'' s(t'') \cos[\omega(t'-t'')]. \tag{1.32}$$

$s(t)$ is a step function describing the sign of effective phase accumulated during free precession time due to the noise field, which is not driven by any microwave or external control. For example, here we list $s(t)$ for Ramsey FID, Hahn echo and CPMG-4, of which the pulse sequences in illustrated in Fig. 1.8,

$$\begin{aligned}
\text{Ramsey: } & s(t) = 1 \\
\text{Hahn Echo: } & s(t) = \begin{cases} +1 & \text{for} \quad 0 < t < \tau \\ -1 & \text{for} \quad \tau < t < 2\tau \end{cases} \\
\text{CPMG-4: } & s(t) = \begin{cases} +1 & \text{for} \quad 0 < t < \tau \\ -1 & \text{for} \quad \tau < t < 3\tau \\ +1 & \text{for} \quad 3\tau < t < 5\tau \\ -1 & \text{for} \quad 5\tau < t < 7\tau \\ +1 & \text{for} \quad 7\tau < t < 8\tau \end{cases}
\end{aligned} \tag{1.33}$$

The corresponding filter functions are

$$\begin{aligned}
\text{Ramsey: } \mathcal{F}(\tau,\omega) &= \frac{1}{2}\frac{\sin^2(\omega\tau/2)}{(\omega/2)^2} \\
\text{Hahn Echo: } \mathcal{F}(2\tau,\omega) &= \frac{1}{2}\frac{\sin^4(\omega\tau/2)}{(\omega/4)^2} \\
\text{CPMG-4: } \mathcal{F}(8\tau,\omega) &= \frac{1}{2}\frac{\sin^6(\omega\tau/2)[\cos(3\omega\tau/2)+\cos(5\omega\tau/2)]^2}{(\omega/16)^2}.
\end{aligned} \tag{1.34}$$

In contrast to Ramsey, the Hahn echo filter function is zero at $\omega = 0$, so the phase from a constant field (being constant during each shot, but the amplitudes can be random) is canceled. In the Carre-Purcell-Meiboom-Gill (CPMG)-like pulse sequences, the filter function does not depend on the phase of the microwave π pulses. For instance, XY4 and XY8 pulse sequences should have the same filter function as CPMG-4 and CPMG-8, respectively, while being helpful to mitigate pulse errors better [56, 57, 58]. Such pulse error canceling effect can be easier to understand if one uses the Bloch sphere to visualize it. A general filter function for CPMG-N, where N is the number of π pulses, can be computed

$$\text{CPMG-}N\text{: } \mathcal{F}(2N\tau,\omega) = \frac{2\sin^2(\omega N\tau)[1-\sec(\omega\tau)]^2}{\omega^2}. \tag{1.35}$$

Note that the filter functions reach their maximum when $\omega T = \pi$, where T is the total free precession time. Therefore, if the total precession time is fixed, then with more π pulses, the filter function will be effectively shifted to a higher frequency and will have a narrower width for the 1st order peak, as shown in Fig. 1.8(b).

In Chapter 5, we will further present some recent theory and experiment development where we study how many-body noise in strongly interacting spin systems could affect the central spin's dephasing in Ramsey, Hahn echo, and other dynamical decoupling sequences.

Chapter 2

Experiment setup: laser scanning confocal microscopy with scanning NV magnetometry

The experiment setup in the east side of our Broida 1219 lab is used for most of the NV measurements presented in this dissertation. The setup has already been thoroughly discussed in Bryan Myers' dissertation as "Magnetometer B" in Ref. [59]. Therefore, this chapter serves as a supplementary to it to summarize the setup structure and record the changes we have made in the past 7 years.

This setup was initially designed for NV scanning magnetometry experiments in a sample-on-tip geometry in ambient conditions. We have added 594-nm and 637-nm lasers to the excitation path before the fiber to study the charge state of the NV center and spin-to-charge conversion readout [60, 1]. We have switched to using a different stage for controlling the relative distance between the sensing target and diamond [60]. We also added a "temperature cage" to put the objective and scanning components inside in order to improve temperature stability around room temperature [60]. Some changes have

been made to the microwave circuit to perform the double electron-electron resonance (DEER) experiments [2, 4, 3]. The diamond sample holder can now be adjusted to a different configuration to allow for easier switching between diamond samples when scanning experiments are not needed. Overall, this setup has been adjusted and fine-tuned to be suitable for many kinds of NV experiments in ambient conditions.

2.1 Laser scanning confocal microscopy

Laser-scanning confocal microscopes were immediately popular among biologists once they were invented, and they have overcome many of the limits of the traditional light microscope. This innovative microscope allows for the extraction of exceptionally clear and thin optical slices from the fluorescent samples [61]. In short, 3D images can be acquired by simply moving the sample relative to the objective or employing the scanning galvo mirrors as well, with lateral and axial resolution on the order of a few hundred nanometers and a few microns, respectively. Such advantages of the confocal microscope include the ability to image single NV centers in diamonds and the ability to suppress the collection of photons from the background. A simple estimation of the diffraction-limited spot size of a uniform confocal beam should be half of the Airy unit diameter 1A.U.$\approx$ 1.22λ/NA, where NA is the objective lens numerical aperture. For our experiment, when using the 532 nm laser and our NV=0.95 objective, the Airy diameter is 680 nm. In practice, we usually observed the beam spot with a diameter on the order of 1 μm.

The entire confocal microscopy is set up on an optical table. The schematic of the optical paths are shown in Fig. 2.1 and Fig. 2.2. The details of the components, including the description, vendor, and part number, are listed in table 2.1 and 2.2. These two schematics generally reflect the current actual locations of each component for future reference. The optical paths are separated into two parts, before the fiber and after the

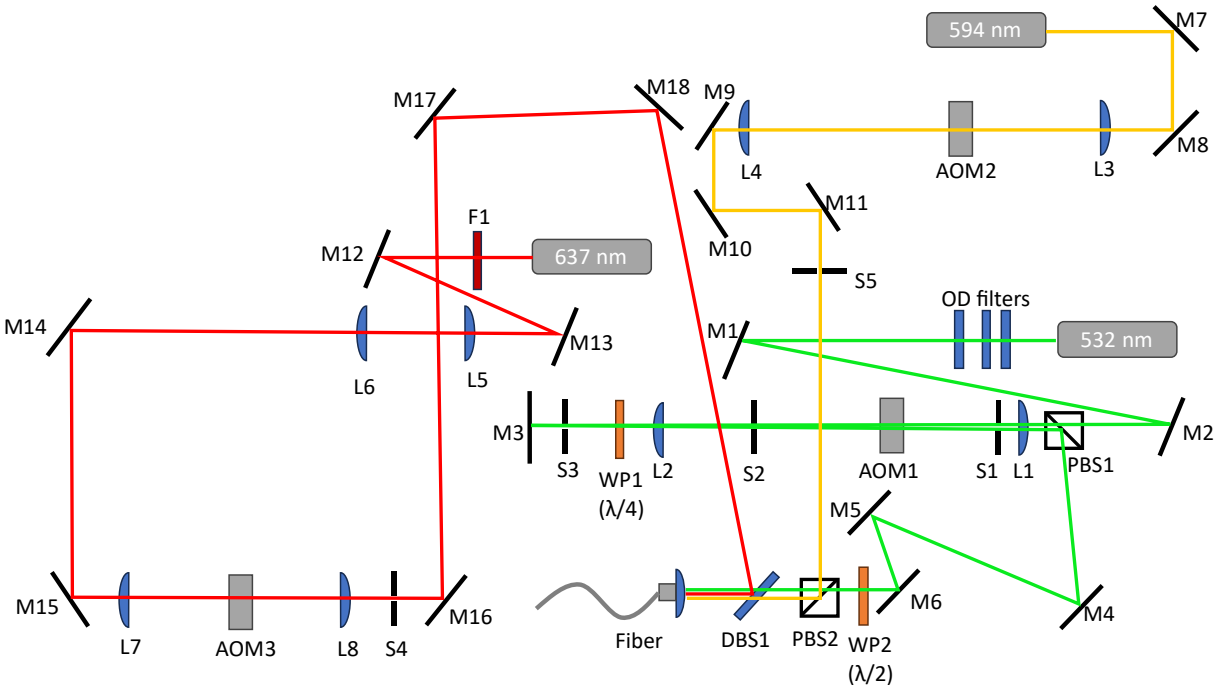

Figure 2.1: Schematic of the excitation path before the fiber. The use of the fiber in the excitation path makes it easy to align the path before and after the fiber separately. Three different wavelengths can be coupled to the fiber: 532 nm, 594 nm, and 637 nm. See table 2.1 for details of all components shown here. "M#" stands for mirrors, "L#" stands for lens, "S#" stands for beam shutters, "F#" stands for filtrs, "WP#" stands for waveplates, "PBS#" stands for polarizing beamsplitter, "DBS#" stands for dichroic beamsplitter.

Parts symbol	Description	Vendor and Part No.
532 nm	Solid-state low noise 532-nm laser, 200 mW	Opto Engine,MLL-III-532
PBS1	Polarizing Beamsplitter Cube, 420-680 nm	Thorlabs, PBS251
L1	Plano-Convex Lens, 125 mm, AR coating: 350-700 nm	Thorlabs, LA1986-A
AOM1	Acousto-optic modulator, 440-700 nm, 200 MHz	IntraAction, ATM200C1
L2	Plano-Convex Lens, 200 mm, AR coating: 350-700 nm	Thorlabs, LA1708-A
WP1	Quarter-wave plate, 532-1480 nm	Foctek, WPF212H
WP2	Half-wave plate, 532-1480 nm	Foctek, WPF220H
PBS2	Polarizing Beamsplitter Cube, 420-680 nm	Thorlabs, PBS201
DBS1	Dichroic Beamsplitter, cutoff = 611 nm	Semrock, FF611-SDi01
594 nm	Yellow HeNe laser, 594 nm, 2.0 mW, 500:1 polarization	Newport, R-39582
L3	Plano-Convex Lens, 150 mm, AR coating: 350-700 nm	Thorlabs, LA1433-A
AOM2	Acousto-optic modulator, 470-690 nm, 200 MHz	G&H AOMO 3200-125
L4	Plano-Convex Lens, 100 mm, AR coating: 350-700 nm	Thorlabs, LA1509-A
637 nm	Laser diode 170mW on a TE-cooled mount	Thorlabs, HL63133DG
Laser driver	6305 ComboSource, 500mA	Arroyo Instruments, 6305
F1	Filter, 637/8 nm single-band bandpass	Semrock, FF01-637/8-25
L5	Unknown, for collimating the red laser	Unknown
L6	Unknown, for collimating the red laser	Unknown
L7	Plano-Convex Lens, 100 mm, AR coating: 350-700 nm	Thorlabs, LA1509-A
AOM3	Acousto-optic modulator, 440-700 nm, 200 MHz	IntraAction, ATM200C1
L8	Plano-Convex Lens, 100 mm, AR coating: 350-700 nm	Thorlabs, LA1509-A
Fiber	Single-mode, 400-680 nm, S405-XP FT030-Y FC/PC	Thorlabs, custom patch

Table 2.1: Parts list of the excitation path before the fiber. There are three wavelengths, 532 nm, 594 nm, and 637 nm. "M#" stands for mirrors, and mostly are silver mirrors. "S#" stands for beam shutters, and they are mostly used for blocking $m \neq 1$-th order diffraction patterns of laser coming out from AOM. The laser driver for 637-nm laser diode is not the corresponding accessory from Thorlabs, so it is also listed here.

fiber. Aligning the optics can, therefore, also be separated, and the misalignment of one part does not affect the other part. In front of the 532 nm laser, there are three layers of neutral density filters (OD filters) for attenuation; the first two are manual wheels, and the third one is with a motorized wheel (Thorlabs, FW102C). Unlike the other two wavelengths, the 532 nm laser is double-passing the acousto-optic modulator (AOM) to increase the effective isolation, in other words, to decrease the laser power into the fiber when AOM is turned off. L1 and L2 are a pair of two lenses that focus the laser beam into the AOM1 and re-collimate it after coming out. The same for other pairs of lenses around the AOMs. The beam shutters, for example, S1, S2, and S3 are generally used for blocking the extra diffraction patterns of AOM or reflections to prevent them from coupling to the fiber when AOM is off. The double-passing geometry is essentially achieved by using the polarising beamsplitter (PBS1) and the quarter-waveplate (WP1, $\lambda/4$). The green laser passed WP1 twice, so its phase is shifted by $\pi/2$ and can be greatly reflected by the polarising beamsplitter. As for the 637 nm laser, we are currently using a laser diode and a bandpass filter (F1) with a narrow band around 636 nm to further filter the spectrum. To combine the three wavelength lasers, a polarising beamsplitter (PBS2) is used for directing the yellow laser to the green path, and a dichroic beamsplitter (DBS1) is used for combining red. The dichroic beamsplitter has a cutoff around 611 nm, so it mainly reflects the red laser. The fiber used here is a single-mode laser for 400-680 nm lasers, and the transmission for the green is usually around 70%, so it introduces some loss, but it greatly simplifies the alignment by isolating the whole path into two parts.

The schematic in Fig. 2.2 shows the excitation path with a green solid line, but it represents the collimated lasers of three wavelengths, 532 nm, 594 nm, and 637 nm together. Our objective has a correction collar to look through glass or diamond, and it has a high NA for dry imaging to increase the photon collection efficiency. The collection

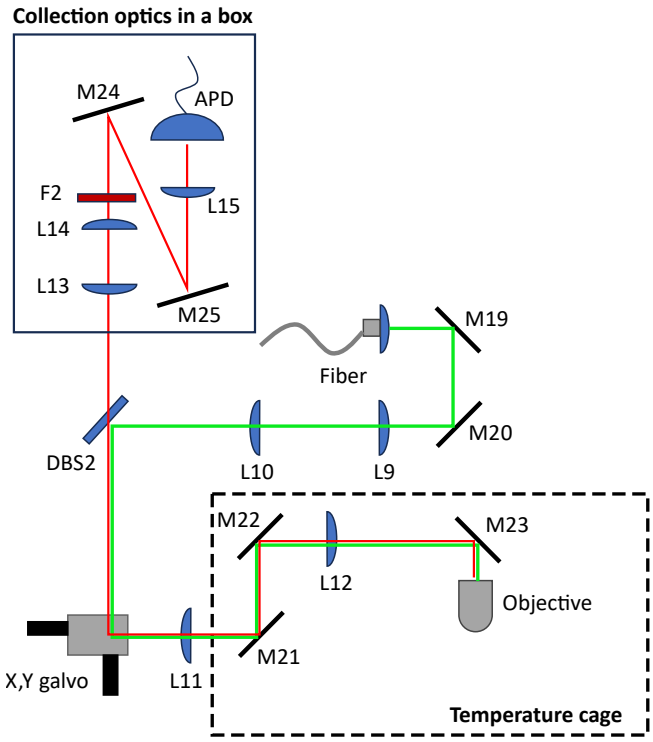

Figure 2.2: Schematic of the collection path and excitation path after the fiber. The collection optics are kept inside a box to block the room light. The "temperature cage" also contains the components shown in Fig. 2.5 including the translation stage, stepper for diamond sample, AFM piezo, etc.

Parts symbol	Description	Vendor and Part No.
DBS2	Dichroic Beamsplitter, transmission >∼532 nm	Semrock, Di01-R532-25x36
L9	Plano-Convex Lens, 50 mm, AR:350-700nm	Thorlabs, LA1131-A
L10	Plano-Convex Lens, 100 mm, AR:350-700nm	Thorlabs, LA1509-A
L11	Achromatic doublet, 150 mm, B:650-1050nm	Thorlabs, AC508-150-B
L12	Achromatic doublet, 300 mm, B:650-1050nm	Thorlabs, AC508-300-B
L13	Achromatic doublet, 200 mm, B:650-1050nm	Thorlabs, AC508-200-B
L14	Achromatic doublet, 100 mm, B:650-1050nm	Thorlabs, AC254-100-B
L15	Ashpheric lens,f=11.00 mm,NA=0.30,650-1050nm	Thorlabs, A397TM-B
F2	Long-pass filter, wavelength> 600 nm	Semrocks, BLP01-594R-25
APD	Avalanche photodiode, efficiency ∼65% @ 650 nm	Perkin Elmer, SPCMAQR14
X,Y galvo	Scanning mirrors	Thorlabs, GVS012 (10 mm)
Objective	Objective with correction collar, NA=0.95	Olympus UPlanSAPO 40x2

Table 2.2: Parts list of the collection path and excitation path after the fiber.

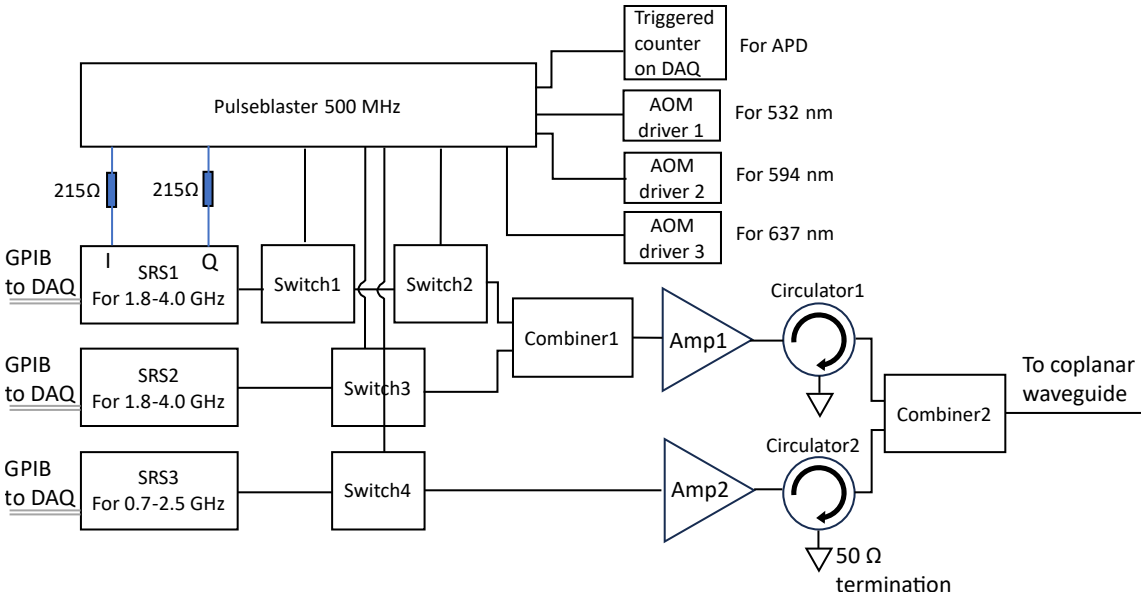

Figure 2.3: Diagram of the RF/microwave circuits including logical programmable pulse generator (Pulseblaster). Here, we are using 10 output channels ("bits") from the Pulseblaster. See table 2.3 for details of the components shown here. The microwave is generated by the three SRS signal generators. They can be controlled by a 0.5 V TTL pulse to generate microwaves with different phases through I and Q input channels. Ideally, the IQ switchbox should be used for access to all four IQ pulses (±X and ±Y for spins) [59]. Here, we are only using +I and +Q pulses for SRS1, and the 215 Ω resistors bring down the TTL voltage from PulseBlaster (+3.3 V) to SRS1 (+0.5 V). Therefore, with the circuit configuration shown here, we can generate +X and +Y from SRS1, but only +X from SRS2 and SRS3. This is adequate for most of our experiments. "DAQ" stands for the DAC board (National Instruments, PXIe-6363).

optic components after L13 are all kept in a box to block room light, which helps to reduce the background PL by at least a few kct/s. The temperature cage is a black plastic box that covers the scanning components around the objective and maintains the temperature stability inside. More details will be discussed later in this chapter. One last thing to note is that when performing charge state or relaxation measurement, extra black curtains may be used to cover the optics around DBS2, X,Y galvo, and temperature cage. This helps to bring down the stray light power from the lab by a few hundreds of μW, which is relevant when dark time is on the order of milliseconds.

Parts symbol	Description	Vendor and Part No.
SRS1/2/3	RF signal generator, DC-4.05 GHz	Stanford Research Systems, SG384/123
Switch1/2	RF switch, 0.1-12 GHz, 55 dB	CMC, S0947A-C2
Switch3/4	RF switch, DC-5.0 GHz, 70 dB	MiniCircuits, ZASWA-2-50DRA+
Combiner1	2 Way Power Divider, DC-4.2 GHz	MiniCircuits, ZFRSC-42+
Combiner2	2 Way Power Divider, 0.5-6.0 GHz	MCLI, PS2-94
Amp1	High Power Amplifier, 1.8-4.0 GHz	Mini-Circuits, ZHL-16W-43+
Amp2	High Power Amplifier, 0.7-2.5 GHz	Mini-Circuits, ZHL-30W-252+
Ciculator1	Circulator 2.0-4.0 GHz, SMA	Narda-MITEQ, 4923
Ciculator2	Circulator, 0.8-2.0 GHz, SMA	MECA Electronics, CS-1.400
Pulseblaster	Programmable Pulse Generator, 500 MHz	SpinCore, ESR-PRO-500-PCIe

Table 2.3: Parts list of the microwave circuit components. The Pulseblaster is a high--speed programmable pulse generator that directly interfaces with PC and controls the pulse sequence. The minimal TTL signal form it is 10 ns with a resolution of 2 ns.

The microwave circuit, including the logical programmable pulse generator (Pulseblaster), is shown in Fig. 2.3. The components details are listed in table 2.3. Overall, the setup is controlled by a home-built software written in Matlab on the PC. The Pulseblaster (500 MHz) directly interfaces with the PC and can be programmed to generate 3.3 V TTL pulses through different channels ("bits") to perform pulse sequences. The minimal duration that can be usually generated is 10 ns, with a resolution of 2 ns. Each bit can be connected to an instrument and may vary. The signal generators (SRS, SG384) can generate microwaves continuously with different phases. The phase can be controlled by the IQ modulation, I and Q input channels. For example, -0.5V at I input means -X microwave. Because of the voltage difference between Pulseblaster and SRS's IQ channels, we usually use an IQ modulation switchbox to transform +3.3 V to ±0.5 V TTL. Alternatively, as shown in Fig. 2.3, we use a resistor of around 215 Ω to bring down the voltage, but this method only works for +X and +Y pulses. If IQ modulation is not specified (for SRS2 and SRS3), the SRS generates +X microwaves. Then the microwave is gated by the switch. We pass the signal from SRS1 through two identical switches

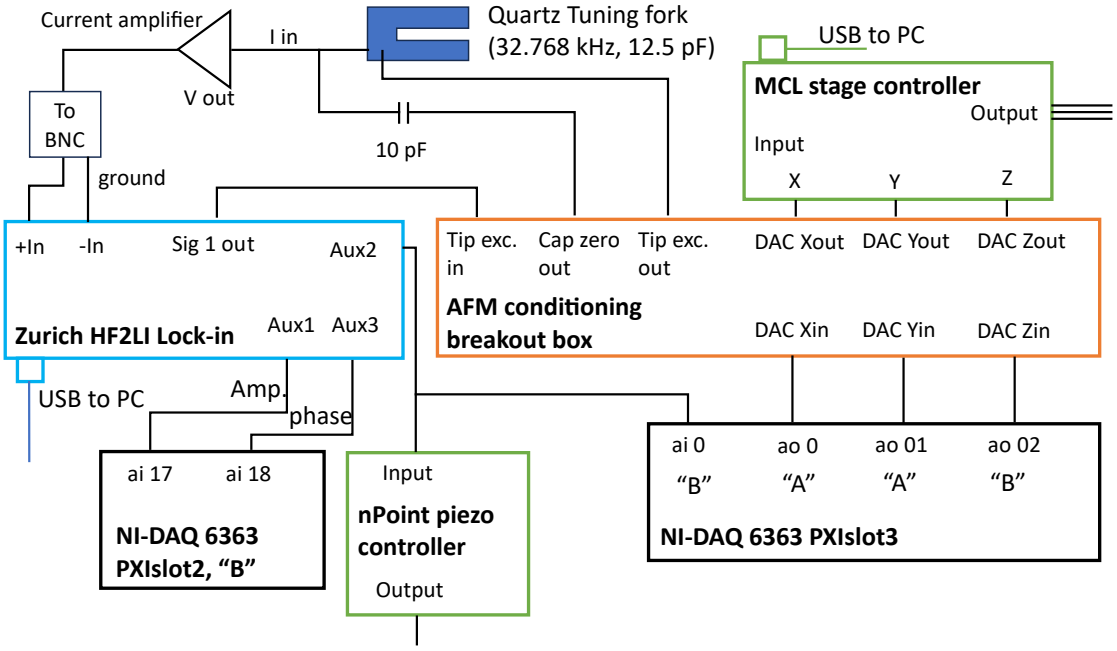

Figure 2.4: The circuit diagram of the electronics for the scanning components. See Fig. 2.5 for the schematic and picture of the scanning setup. Through a PID controller inside, the Zurich lock-in controls the nPoint piezo (one-axis, Motion Solutions) which moves the sensing target on the tuning fork relative to the diamond sample in z direction. This feedback signal of this PID controller is the tuning fork's current after the amplifier. The PC reads the amplitude and phase of the signal from the tuning fork, voltage to the nPoint input through the NI-DAQ card. The PC also controls the MCL (three-axes, Mad City Labs, Nano-LP300) controller's input through the NI-DAQ card, and the setpoint, driving conditions, etc. of the Zurich lock-in's PID controller. Details of the AFM conditioning breakout box can be found in Ref. [59].

to further increase the isolation. For the other two SRS, the switch itself has a much better isolation (70 dB), so we only use one switch. The "DAQ" refers to the DAC board (National Instruments, PXIe-6363), and can be used as analog output ("ao #") or analog input ("ai #"), controlled by the Matlab program. One rule of thumb in designing the pulse sequence is that the response times of different components are different. Therefore, one needs to calibrate the delay time of each component first [59].

2.2 Scanning NV magnetometry

The laser confocal microscopy can be further combined with scanning components. The schematic of the electronics used to perform the NV scanning experiment is shown in Fig. 2.4. The scanning is controlled by the commercial lock-in amplifier (Zurich Instruments, HF2LI 50 MHz), and a home-built AFM conditioning breakout box. We employ the tuning fork as the AFM probe and attach the sensing target onto the top of the tuning fork as shown in Fig. 2.5. The main difference from the previous version of our setup is that we added the nPoint one-axis stage, which serves as a high-bandwidth z scanner so that a fast AFM imaging can be achieved.

The geometry of the scanning setup is shown in Fig. 2.5. The diamond is facing down towards the sensing target glued on the tuning fork. We typically fabricate diamond nanopillar to enhance photon collection, identify single NVs, and make the positioning of certain NV above sensing targets much easier [60]. The sensing target is glued onto the tuning fork, and the tuning fork is glued on a piece of coverslip clipped on the tuning fork holder. The electrodes on two prongs of the tuning fork are then connected to coaxial cables. The definitions of axes directions for each component are also listed for future reference. The diamond sample stage, Micronix stepper, nPoint stage and the three-axes MCL stage are attached to a bottom X,Y translation stage. Therefore, they can move together relative to the confocal objective above. This serves as the first level of coarse positioning of the experiment. The three-axes MCL stage only has a small movement range (100 μm), but the exact position of the sensing target on top of the tuning fork varies a large amount from one sample to another. Therefore, the Micronix stepper, which holds the sample stage but is not attached to the MCL stage, should be used as the second step to coarsely adjust the diamond to above the sensing target. Before the scanning experiment, the objective can be brought close to the backside of

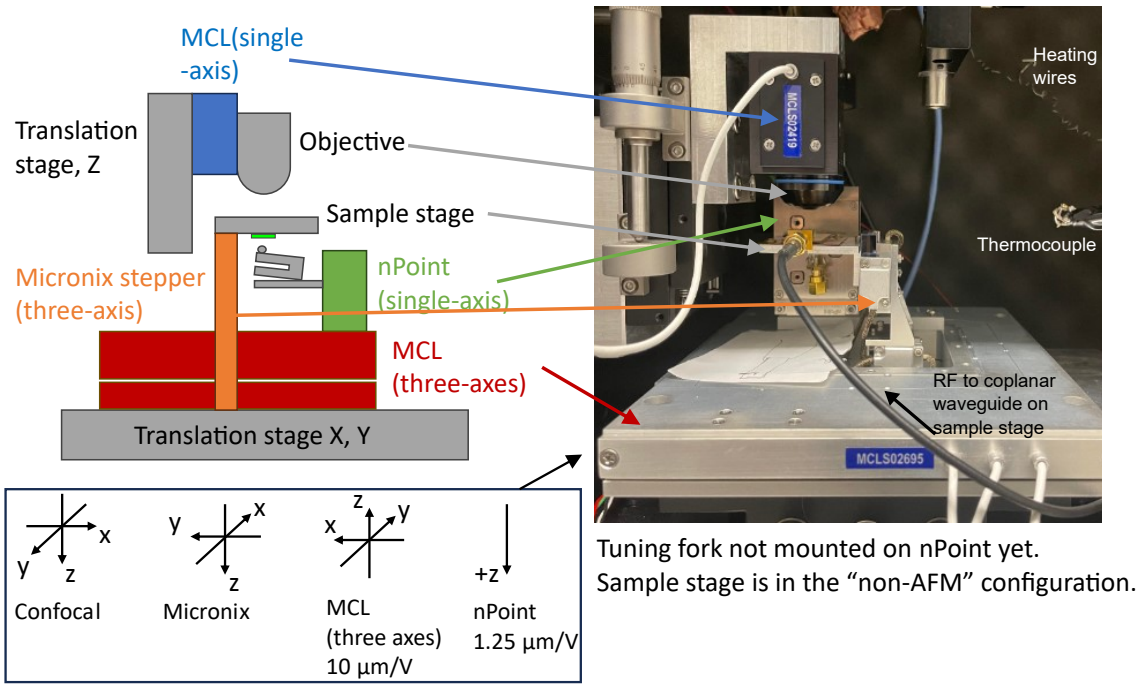

Figure 2.5: Scanning components and some confocal microscope components at the center of the temperature cage. Shown on the left side is a schematic of the components; on the right side is a photo of the setup. The translation stage (Z) controlling the objective is not attached to the bottom translation stage (X,Y). Therefore, the bottom X,Y translation stage can be used to move both the diamond sample stage and tuning fork on nPoint/MCL together relative to the confocal microscope axes. The Micronix stepper is used to coarsely position the diamond sample stage. In the photo, one of the thermocouples and heating wires, which is used to control the temperature inside this temperature cage, is also shown. The two connectors to be connected to the tuning fork are outside of the view. At the bottom, the definitions of the axes for each scanning component are shown.

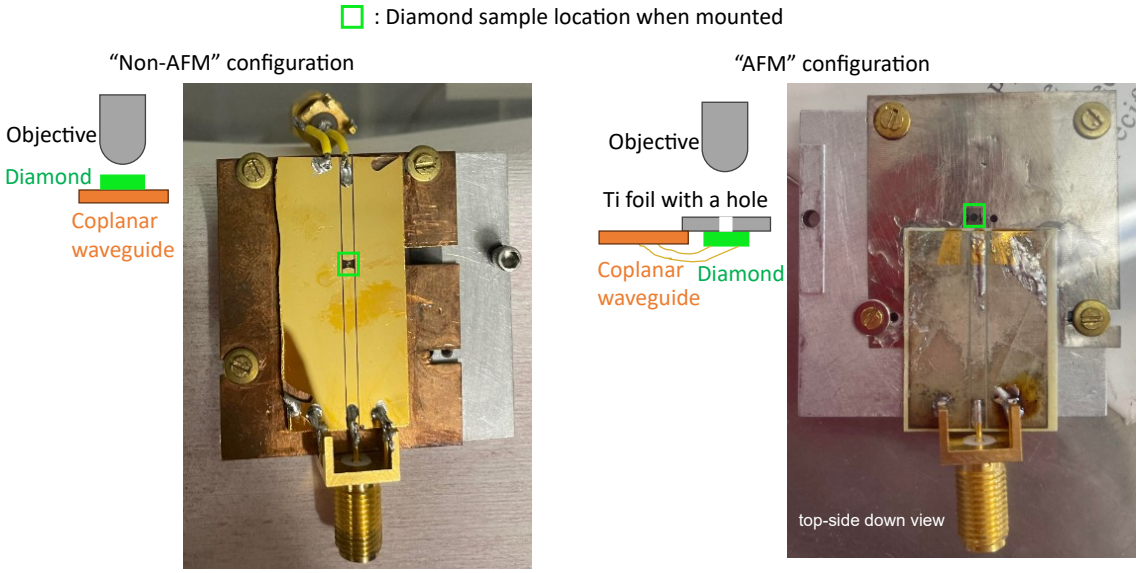

Figure 2.6: The two different configurations for the diamond sample stage. The "non-AFM" configuration is used when there is no scanning experiment. The diamond sample sits freely on the coplanar waveguide, which can be connected to the microwave circuit shown in Fig. 2.3 and emits microwave to drive NVs and other spins. The NV side of the diamond should face the coplanar waveguide, and the confocal microscope should look through the diamond. The "AFM" configuration can be used for scanning experiments. The titanium foil is thin enough to satisfy the objective's working distance. To deliver the microwave, a coplanar waveguide should be fabricated onto the diamond surface (NV side) for this configuration. The diamond is then glued onto the foil and wirebonded to the outside waveguide.

the diamond and image both the desired single NV in nanopillar and the sensing target on the tuning fork through the diamond (if the tilt angle between the optical path and sample stage is maintained to be small and working distance allows). Lastly, during the scanning experiment, the MCL can be used to move the tuning fork in the lateral direction, and nPoint stage can be used to control z motion to enable tapping mode or similar to peak-force-tapping mode.

We typically perform amplitude-modulated AFM. The frequency we drive the tuning fork (through the inverse piezoelectric effect) is usually first fixed to the resonance frequency, which is around the original frequency of 32.768 kHz, depending on the sensing target that is glued on the tuning fork. Then when the tuning fork engages to be close

to the diamond, both the resonance frequency and quality factor Q will decrease since the vibration is damped, so the driving frequency now becomes slightly higher than the new resonance frequency. Therefore, when the repulsive force between the tuning fork and the diamond increases, the resonance frequency will further decrease, and the vibration amplitude (signal as the current from the tuning fork) will decrease. Here, we use a commercial current-to-voltage amplifier (Femto LCA-100K-50M, DC-100 kHz) with a gain of 5e7 V/A to convert and amplify the tuning fork output current to voltage for Lock-in's input.

In fact, in ambient conditions, there is a confined nano-water with a nanometer-scale thickness between the diamond and tuning fork/sensing target. When the tuning fork actually engaged and "snapped" onto the diamond surface within a few nanometers, depending on the actual vibration amplitude, there is a sudden decrease of vibration amplitude and phase, which we use as the signal indicating the engagement [62, 63]. By setting a threshold to either the amplitude or phase, one can detect the engagement easily, so a tapping mode (TM) AFM by tuning fork can be achieved. The feedback control loop to perform TM scanning can be done either by using the PID controller inside Zurich Lock-in or by using the GUI in our Matlab program with an algorithm similar to a PID controller. Furthermore, we also observed that the standard deviation of the amplitude and phase of the signal from the tuning fork ("V out" from the amplifier in Fig. 2.4) also increases when the engagement happens. Therefore, in practice, we can also use the standard deviations as the signal to determine engagement. Experimentally, for example, in one engagement, when the amplitude decreases from 35.2 mV to around 32 mV, we observed the standard deviation increase from 0.1 mV to 0.5 mV; and when the phase increases from -47.5 degrees to around -30 degrees, the standard deviation increases from around 0.15 degrees to over 1 degrees. Alternatively, we can use the frequency shift instead of the amplitude as the feedback signal as well.

The mechanical vibration amplitude of the tuning fork can be characterized by the deflection spectrum at thermal excitation [64, 65]. We measured one of the tuning fork prongs to have a dimension of length $L = 3.10(5)$ mm, thickness $t = 0.41(1)$ mm, and width $w = 0.35(1)$ mm. Therefore, the effective spring constant can be approximated by [65]:

$$k = \frac{Ewt^3}{4L^3} = 15930 \pm 650 \text{ N/A}, \tag{2.1}$$

where E is the Young's modulus. Then, the thermal deflection amplitude of one prong will be:

$$A_{\text{therm}} = \sqrt{\frac{k_B T}{2k}} = 0.36 \pm 0.01 \text{ pm}, \tag{2.2}$$

where k_B is the Boltzmann constant. Experimentally, we measured the tuning fork's (when mounted on the tuning fork holder) deflection voltage spectrum at room temperature without driving the tuning fork. Then, we fitted the spectrum with a Gaussian function, centered at the resonance frequency, and extracted the voltage amplitude of the tuning fork measured at Lock-in to be 8.7 ± 0.2 μV. The current-to-voltage amplifier should still have a good linearity for output voltage within a volt. Therefore, the coefficient between the voltage and actual vibration can be determined to be:

$$c = 24 \pm 5 \text{ mV/nm}. \tag{2.3}$$

For example, to maintain a small distance between the NV center and the sensing target small and relatively constant, we may want to keep the vibration smaller than 1 nm. Thus, the voltage amplitude reading at the Zurich Lock-in should be kept below 24 mV by tuning the excitation voltage ("Sig 1 out" in Fig. 2.4) to be small (typically around 0.2 mV but will depend on the actual Q factor).

Lastly, the temperature control system to keep the temperature in the cage a few

Kelvin above the temperature can achieve a sensitivity around $\sim$0.1 mK/$\sqrt{\text{Hz}}$. It mainly contains the following components: (1) the Raspberry Pi with a PID controller code in Python; (2) a thermistor with 10 kΩ at RT, B constant around 3400 K, temperature range $-$40-120 °C (TDK corporation, NTCG103JF103FT1); (3) a DC current source to apply current to thermistor; (4) a multimeter (Agilent Technologies, 34980A) to measure the voltage across the thermistor, connected to the Raspberry Pi through GPIB; (5) heating wires, $\sim 60\Omega$ is enough for us; (6) current amplifier circuit to amplify the current output from Raspberry Pi to supply the heating wire. More details of the performance of the temperature cage with this control system in an experiment are discussed in Chapter 6.

Chapter 3

Identifying and mitigating charge instabilities in shallow NV centers

3.1 Probing the variation of NV charge state characteristics

Shallow, negatively charged nitrogen-vacancy (NV^-) centers in diamonds have received particular attention for their sensing prowess, while neutral NV^0 centers have not achieved promising electron spin control, yet NV^0 is experimentally common [66, 67, 68] and results in undesired background in NV^- experiments. Of particular importance for shallow NV^- centers is that the diamond surface is observed to preferentially convert NV^- to NV^0 [69, 70, 71], thus imposing a clear obstacle to nanoscale sensing applications, where the NV depth is critical to both sensitivity and spatial resolution [72, 73].

In a typical sensing sequence, NV^- spins are initialized optically, interact with a target

The content of this chapter has substantially appeared in the reference [1]: Dolev Bluvstein, Zhiran Zhang, and Ania C. Bleszynski Jayich, Identifying and Mitigating Charge Instabilities in Shallow Diamond Nitrogen-Vacancy Centers, textitPhys. Rev. Lett. **122**, 076101 (2019)

sample in the dark, and are readout optically; the charge behaviors under illumination and in the dark are thus critical to sensor functionality. Under optical illumination in bulk diamond, single NV centers continuously interconvert between negative and neutral charge states as the NV exchanges electrons with the electronic bands, where the steady-state NV^- population reaches $\approx 75\%$ under commonly used CW 532-nm excitation [36, 74, 75, 76, 77, 78]. For near-surface NV centers, however, understanding of photoinduced charge interconversion is largely limited to ensemble measurements which explain surface-induced NV^- ionization as a result of upwards band bending from surface acceptor states [69, 79]. In the dark, studies prior to our work on NV ensembles have contrastingly shown that NV charge states are stable [80, 81, 82] and unstable [83, 42, 84], with no obvious reconciliation or conclusion for individual shallow centers. Instability of shallow NV^- centers under illumination or in the dark would directly compromise sensing modalities, yet understanding is still limited.

In this work we study the charge state properties of single, shallow NV centers both under illumination and in the dark, focusing in particular on the implications for sensing and on identifying the microscopic origins of charge state instability. We find that the fidelity of optical initialization into NV^- exhibits large variations between shallow NV centers as well as over time. We identify reduced NV^- initialization fidelity as the primary source of reduced spin measurement contrast in shallow NVs, which we alleviate by implementing a logic-based charge initialization protocol. We also find that shallow NV^- centers can ionize to NV^0 in the dark, which we methodically identify as tunneling to a single, local electron trap. We achieve control and readout of the trap charge state, and we measure the trap's optical ionization properties. Further, we show that charge conversion in the dark can produce anomalous signatures in spin measurements and, at worst, will appear indistinguishable from T_1 and T_2 spin decay; we demonstrate how to relieve this misleading effect via various measurement protocols.

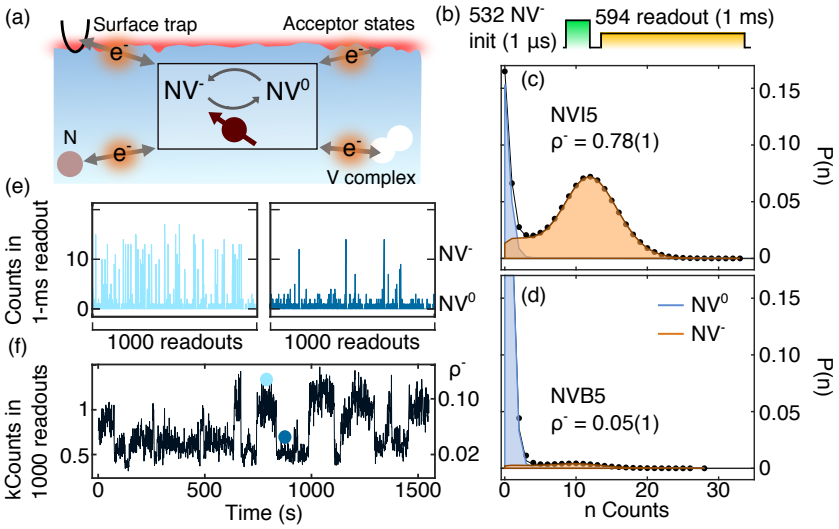

Figure 3.1: NV charge state characteristics vary with different local charge environments. (a) The charge state of local nitrogen (N) centers, vacancy (V) complexes, surface electron traps, and surface acceptor states can all affect the NV charge state. (b) Pulse sequence to measure NV^- initialization fidelity with 532 illumination. (c),(d) Measurement statistics for charge stable (c) and charge unstable (d) NV centers in the same sample. The black line is the sum of the fitted NV^- and NV^0 distributions. $\rho^- \equiv P(NV^-)$ immediately after the 532 nm initialization in (b). (e) Two sets of 1000 consecutive measurements ($\approx$ 1 ms per shot) of the same data comprising the distribution in (d). (f) Consecutive measurements binned into sets of 1000 ($\approx$ 1 second each).

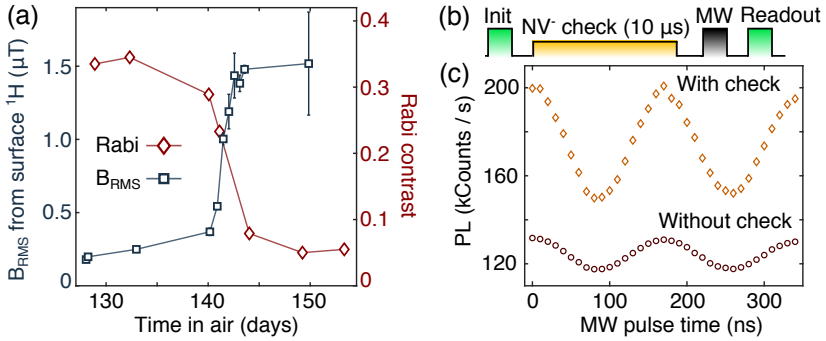

Figure 3.2: (a) Rabi contrast and root-mean-square magnetic field B_{RMS} produced by surface ^{1}H as a function of time under ambient conditions. The spontaneous reduction to NV Rabi contrast is accompanied by a spontaneous increase in the number of surface ^{1}H. (b) Rabi pulse sequence for (c), including logic-based charge initialization protocol. (c) Photoluminescence-based-measurement of Rabi oscillations on charge unstable NV center (at a time when $\rho^- \approx 0.15$), with (orange diamonds) and without (red circles) using precheck protocol.

The experimental setup consists of a home-built, room-temperature confocal microscope for optically addressing NV^- and NV^0 centers, which have zero-phonon lines at 637 nm and 575 nm, respectively [67]. We use a 532 nm laser for spin and charge state initialization and for NV^- spin state readout, and we use a 594 nm laser for charge state readout. Under $\sim$ 2 μW of 594 nm excitation, NV^- is $\sim$ 40x brighter than NV^0 in our setup. NV centers are formed by ^{14}N ion implantation at 4 keV with a dosage of 5.2×10^{10} ions / cm^2 into a 150-μm thick Element 6 electronic grade (100) diamond substrate, followed by subsequent annealing at 850 °C for 2.5 hours (see Appendix A for full details on sample preparation). Single NV centers are found with second-order correlation measurements showing $g^{(2)}(0) < 0.5$ [85], CEWSR measurement showing only one pair of transition peaks, and further confirmed via evaluating charge state photon statistics. The NV center depth is experimentally measured via proton NMR [86] and ranges from $\sim$ 3-17 nm.

We first report on NV^- initialization fidelity ρ^- under 532 nm excitation and its variation in near-surface NV centers. ρ^- is an important parameter for it directly affects

NV^- measurement sensitivity; the NV^0 state gives unwanted background while not contributing to the sensing signal. It has been commonly reported in the literature that with a standard initialization protocol used here, a several-μs-long pulse of green light, ρ^- is consistently $\approx 75\%$. Here we find that ρ^- varies strongly for shallow NV centers and can be significantly less than 75%. In Figs. 3.1(c-d) we measure the NV^- initialization fidelity ρ^- for two near-surface NVs in the same sample. Plotted are the statistics for the number of photons measured during a 1-ms-long 594-nm readout pulse following a 532-nm initialization pulse. The photon statistics are fit to a model that is approximately the sum of two Poisson distributions for NV^- and NV^0, where the relative contribution of the NV^- distribution yields ρ^- (the full model is described later in this section) [74, 87]. For the NV center presented in Fig. 3.1(c) (NVI5), we extract $\rho^- = 0.78(1)$, reproducing the typical reported value for bulk NVs. In contrast, we measure $\rho^- = 0.05(1)$ for NVB5, shown in Fig. 3.1(d). From a sample of 67 individual centers we measure $\langle \rho^- \rangle = 0.59$ and $\sigma_{\rho^-} = 0.15$.

We also find that ρ^- can vary in time on timescales spanning seconds to months. To capture the faster dynamics, in Fig. 3.1(e) we plot two data sets, each consisting of one thousand consecutive 1-ms-long measurements of photon counts for NVB5. The two data sets, taken 2 seconds apart, show a notable difference in outcomes of NV^-, as measured by photon counts, indicating that ρ^- is larger in the first data set than in the second. Coarse-graining the data by binning one thousand consecutive measurements yields the data in Fig. 3.1(f), which shows that ρ^- takes on discrete values that are stable on timescales of seconds to minutes. This discrete behavior suggests that the NV charge state is governed by discrete, metastable configurations of the local charge environment. In practice, this environment-induced slow blinking, which is also observed under CW 532 nm excitation and is distinct from photoinduced hopping between NV charge states, can reduce the sensitivity of near-surface NV centers by introducing substantial slow

noise into measurements.

The model of photon statistics for assessing the charge state of NV is as follows. We typically analyze the photon statistics under a low-power yellow readout (around 1 ms of a few μW 594-nm laser excitation). As shown in Fig. 3.1(b), we plot the probability to get n photons P(n) and then fit the statistics to the sum of two distributions, specifically:

$$\mathrm{P}(n) = \mathrm{P}(n|\mathrm{NV}^-)\mathrm{P}(\mathrm{NV}^-) + \mathrm{P}(n|\mathrm{NV}^0)\mathrm{P}(\mathrm{NV}^0), \tag{3.1}$$

where P(NV^-) and P(NV^0) are the respective probabilities to be in NV^- and NV^0 immediately before readout, and P($n|\mathrm{NV}^-$), P($n|\mathrm{NV}^0$) are the respective probabilities to get n photons given that the NV was in NV^-, NV^0 immediately before readout. Knowledge of the distributions P($n|\mathrm{NV}^-$) and P($n|\mathrm{NV}^0$) then allows to extract P(NV^-) and P(NV^0) = 1 − P(NV^-).

If the NV charge state were stable during the entire readout period, then we have P($n|\mathrm{NV}^-$) = PoissPDF($\gamma_- t_R, n$) and ($n|\mathrm{NV}^0$) = PoissPDF($\gamma_0 t_R, n$), where γ_-, γ_0 are the count rates from NV^- and NV^0, and PoissPDF(λ, n) is the probability of an outcome n for a Poisson random variable with mean value λ. However, if the NV photoionization rate g_{-0} and photorecombination rate g_{0-} are non-negligible, to accurately calculate P($n|\mathrm{NV}^-$) and P($n|\mathrm{NV}^0$) one must account for the possibility of ionization and recombination during readout. For instance, if the NV starts in NV− and then ionizes to NV0 halfway through the readout, then P(n) = PoissPDF($\gamma_- t_R/2 + \gamma_0 t_R/2, n$). The appropriate P($n|NV^-$) and P($n|NV^0$) are thus sums over an infinite number of Poisson distributions, weighted by the probability for each ionization sequence to occur. This weighted infinite sum is calculated by Shields et al. [74] and Hacquebard et al. [87] to

arrive at:

$$\begin{aligned}\mathrm{P}(n|\mathrm{NV}^-,\mathrm{odd}) = \int_0^{t_R} d\tau g_{-0} e^{-g_{-0}\tau - g_{0-}(t_R-\tau)} \\ \mathrm{BesselI}_0(2\sqrt{g_{0-}g_{-0}\tau(t_R-\tau)})\mathrm{PoissPDF}(\gamma_-\tau - \gamma_0(t_R-\tau), n)\end{aligned} \tag{3.2}$$

$$\begin{aligned}\mathrm{P}(n|\mathrm{NV}^-,\mathrm{even}) = \int_0^{t_R} d\tau \sqrt{\frac{g_{0-}g_{-0}\tau}{t_R-\tau}} e^{-g_{-0}\tau - g_{0-}(t_R-\tau)} \mathrm{BesselI}_1(2\sqrt{g_{0-}g_{-0}\tau(t_R-\tau)}) \\ \mathrm{PoissPDF}(\gamma_-\tau - \gamma_0(t_R-\tau), n) + e^{-g_{-0}t_R}\mathrm{PoissPDF}(\gamma_- t_R, n)\end{aligned} \tag{3.3}$$

$$\mathrm{P}(n|\mathrm{NV}^-) = \mathrm{P}(n|\mathrm{NV}^-,\mathrm{odd}) + \mathrm{P}(n|\mathrm{NV}^-,\mathrm{even}). \tag{3.4}$$

where BesselI(m, x) is a modified Bessel function of the first kind. To calculate $\mathrm{P}(n|\mathrm{NV}^0)$ one can simply exchange the subscripts to "0". Under cw excitation, Eq. (3.1) rewritten with the ionization rate g_{-0} and recombination rate g_{0-} because $\mathrm{P}(\mathrm{NV}^-)/\mathrm{P}(\mathrm{NV}^0) = g_{0-}/g_{-0}$ in the steady state. So, in that case, we have:

$$\mathrm{P}(n) = \mathrm{P}(n|\mathrm{NV}^-)\left(\frac{1}{1+g_{-0}/g_{0-}}\right) + \mathrm{P}(n|\mathrm{NV}^0)\left(\frac{1}{1+g_{0-}/g_{-0}}\right). \tag{3.5}$$

In practice, during the measurement, we bin the photons in 100-μs windows and then, in postprocessing, increase the bin size in multiples of 100-μs. We find that this variable bin size is an effective way to verify the validity of the fit. As for the population of the NV^-, $\rho_- = \mathrm{P}(\mathrm{NV}^-)$ after green excitation or in the dark, we can explicitly calculate after fitting the distributions $\mathrm{P}(n|\mathrm{NV}^-)$ and $\mathrm{P}(n|\mathrm{NV}^0)$ to the photon statistics data:

$$\rho^- = \frac{\langle n\rangle - \langle n_0\rangle}{\langle n_-\rangle - \langle n_0\rangle} = \frac{\langle n\rangle - \sum_{n=0}^{\infty} n\mathrm{P}(n|\mathrm{NV}^0)}{\sum_{n=0}^{\infty} n\mathrm{P}(n|\mathrm{NV}^-) - \sum_{n=0}^{\infty} n\mathrm{P}(n|\mathrm{NV}^0)}, \tag{3.6}$$

where $\langle n\rangle$ is the measured mean number of photons per shot, and those two integrals can be approximated by only summing until $n = 10\gamma_- t_R$.

3.2 Charge state stability of shallow NV center under ambient conditions

Our measurements also reveal that the average ρ^- decreases on the time scale of days to months, and this decrease is strongly correlated to environmental changes at the diamond surface. As a practical metric for ρ^- we monitor the NV^- spin fluorescence contrast in a Rabi oscillation measurement; the contrast is reduced when the NV spends more time in the neutral NV^0 state, which contributes spin-independent background fluorescence. Fig. 3.2(a) plots the Rabi contrast of NVI5 as a function of time after a standard surface preparation protocol, which includes acid cleaning and oxygen annealing (see Appendix A). The Rabi contrast was stable at 35% for 130 days before suddenly decreasing to 5% over a span of 20 days. Other NV centers exhibit similar behavior, with *e.g.* NVB5 as shown in Fig. 3.1(d), exhibiting a drop in ρ^- from $\approx 75\%$ to 5% over several months. Notably, cleaning the surface induces a partial or full recovery of ρ^-, suggesting that changes in ρ^- are dominated by surface effects.

Critically, as shown in Fig. 3.2(a), we find that the reduction in Rabi contrast on NVI5 (measured depth ~ 3.5 nm) is strongly correlated with an increase in the number of ^{1}H nuclear spins on the diamond surface, as measured via NV-based nuclear magnetic resonance [88, 89]. The root-mean-square magnetic field B_{RMS} produced by surface ^{1}H is measured with an XY8-k sensing sequence [86, 90]. The reason for the increased hydrogen is unclear, but we make a few observations. The 1.5 μT B_{RMS} value measured after long air exposure is too large to be exclusively due to a two-dimensional surface hydrogen termination layer, indicating that other adsorbates such as water or hydrocarbons are contributing. We further note that other NV centers did not exhibit similar changes in contrast and ^{1}H density between days 130 to 150, and hence we speculate that laser-illumination also plays a role. The importance of maintaining high Rabi contrast over

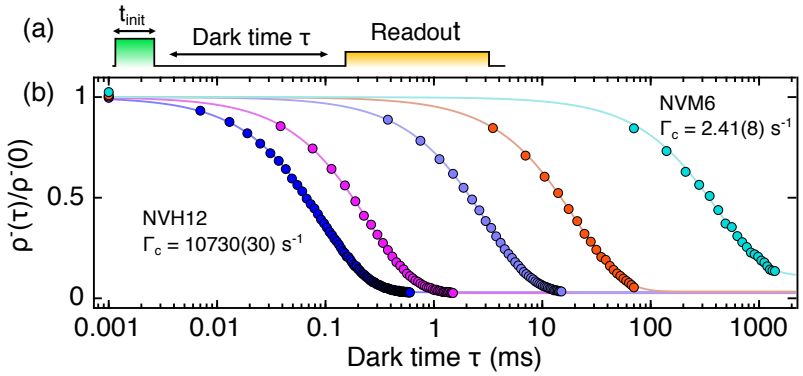

Figure 3.3: NV^- survival probability in the dark after 532 nm initialization. (a) Measurement sequence for (b). (b) NV^- ionization in the dark measured on 5 representative NV centers; solid curves are fits to the exponential decay in Eq. 3.7. Left to right, $\Gamma_c = 10730(30)$, 4030(10), 331(1), 48.9(6), 2.41(8) s^{-1}.

extended periods of time is critical for NV-based sensing, and the correlation discovered here motivates a more detailed investigation.

The deleterious effects of low ρ^- on Rabi contrast can be alleviated by implementing a measurement protocol (Fig. 3.2(b)) that checks for successful NV^- initialization prior to the spin measurement sequence. In Fig. 3.2(c), we plot a Rabi measurement with and without this precheck; the spin measurement contrast increases from 14 kct/s to 50 kct/s, and the measured signal-to-noise ratio increases 3-fold. This result also serves to confirm that poor NV^- initialization fidelity is the dominant source of reduced Rabi contrast. In demonstrating this precheck technique in Fig. 3.2(b), we postselect on the raw data by removing measurements where no photons were detected during the 10-μs, 594-nm NV^- check in Fig. 3.2(b). In practice, to increase measurement sensitivity, one would integrate on-the-fly logic to reinitialize after a failed precheck.

3.3 Charge state dynamics in the dark and single local electron trap model

We now turn to a discussion of NV charge state dynamics in the dark. In Fig. 3.3(b) we plot the NV^- population as a function of dark wait time after a 532 nm initialization pulse (Fig. 3.3(a)) for five NVs; NV^- ionizes to NV^0 in the dark with a wide distribution of decay times. All NVs fit well to a model of exponential decay

$$\rho^-(t)/\rho^-(0) = 1 - A\left(1 - e^{-\Gamma_c t}\right) \tag{3.7}$$

where decay rate Γ_c, starting NV^- population $\rho^-(0)$, and decay amplitude A are free fit parameters, with $0 \leq A \leq 1$. The five NVs plotted in Fig. 3.3 span four orders of magnitude in fitted Γ_c, with timescales ranging from 100 μs to seconds. From a sample of 108 individual centers, approximately: 10% of NVs have $\Gamma_c > 50$ s^{-1}, 10% have 50 s^{-1} $> \Gamma_c >$ 20 s^{-1}, 30% have 20 s^{-1} $> \Gamma_c >$ 1 s^{-1}, and 50% have $\Gamma_c <$ 1 s^{-1}. We do not observe a dependence of Γ_c on the magnetic field or a strong correlation with NV depth.

We find that the dark ionization process is highly dependent on initialization power and duration. To illustrate this dependence, Fig. 3.4(a) plots the charge decay observed on NVI2 (middle curve in Fig. 3.3(b)) for different initialization times $t_{init} = 3$ and 200 μs. Both curves are well fit by the model in Eq. 3.7. Interestingly the two fits yield the same value of Γ_c (within error), but A changes substantially; as $t \to \infty$, NV^- decays to NV^0 in 98% of the measurement shots for $t_{init} = 200$ μs, but only in 42% of the shots with $t_{init} = 3$ μs. We note that in Fig. 3.3, t_{init} was chosen to be long enough on each NV such that A reaches its saturation value.

To arrive at a more quantitative understanding of the observed NV^- ionization be-

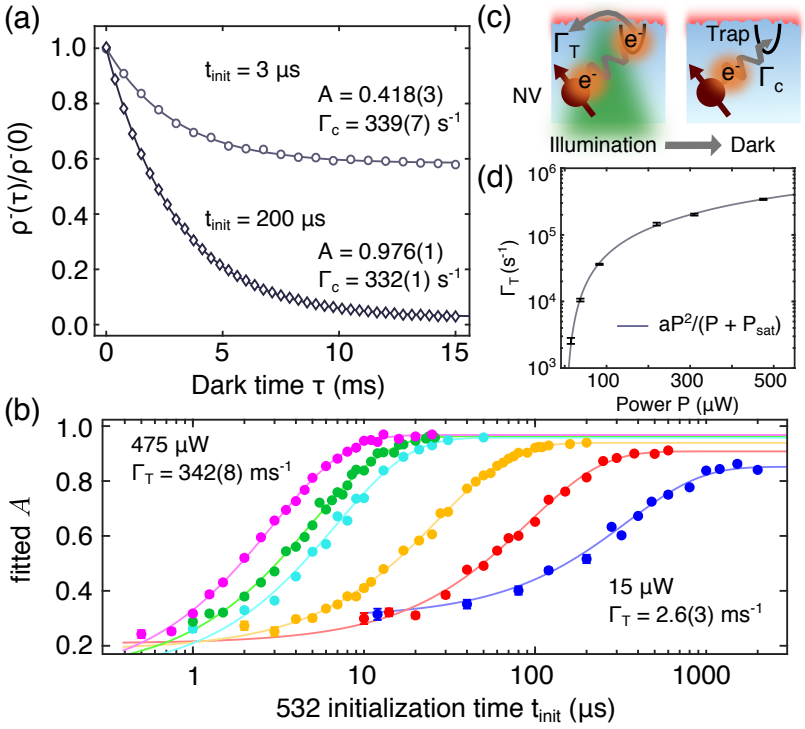

Figure 3.4: (a) Charge decay measurement (Fig. 3.3(a)) with 225-μW, 532-nm excitation for $t_{init} = 3$ μs (light circles) and 200 μs (dark diamonds). Solid curves are a fit to the model in Eq. 3.7. (b) Fitted values of A for varied initialization times at six laser powers ranging from 15 μW to 475 μW. The solid curves are fits to a model of exponential saturation with rate $\Gamma_T + \Gamma_c$. (c) Model for charge decay: a local electron trap is ionized during initialization at rate Γ_T and then captures an electron from NV^- at fixed tunneling rate Γ_c in the dark. A is then the probability that the trap is empty. (d) Trap ionization rate Γ_T vs. laser power. Solid curve is a fit to $aP^2/(P + P_{sat})$.

havior, we repeat the measurement in Fig. 3.4(a), varying t_{init} over a large range of values. The dependence of A on t_{init} is plotted in Fig. 3.4(b) at six different powers, and the result is fit well by a mono-exponential with a rate that increases with initialization power. Γ_c does not change with initialization time or power.

To explain the observations of figures 3.4(a) and 3.4(b), in Fig. 3.4(c), we present a model of electron tunneling to a single, dominant local electron trap with fixed tunneling rate Γ_c. If the trap is empty, NV^- will decay to NV^0 as $t \to \infty$; A then represents the probability that the trap is empty. In our model, the green illumination ionizes the trap at rate Γ_T and thus empties the trap with probability $A \sim 1 - \exp(-\Gamma_T t_{\text{init}})$, as observed in Fig. 3.4(b). To repump the trap between measurement repetitions, we optically initialize into NV^- and wait in the dark for a time $> 3/\Gamma_c$.

A key result is that the presence of multiple dominant traps is inconsistent with the data in Fig. 3.4. More than one dominant trap would result in non-mono-exponential decays. This fact can be understood by interpreting Eq. 3.7 as the probability of surviving charge decay to one particular trap, the i^{th} trap, which we express as $P_s(i)$. For multiple traps, the probability to survive decay, $\rho^-(t)/\rho^-(0)$, would then be the product of the individual survival probabilities $\Pi_i P_s(i)$. This product is necessarily non-mono-exponential for more than one trap. Further, though non-mono-exponential decays can resemble mono-exponential decays, the fitted Γ_c would then necessarily increase with A, which we also do not observe. With this analysis, we identify the mechanism for charge decay as tunneling to a single local electron trap. Moreover, we can controllably and quantitatively set the trap charge state population by varying t_{init} as in Fig. 3.4(b).

We probe the ionization properties of the trap with our control and readout capabilities: we intentionally populate the trap via controlled tunneling of an electron from NV^- to the trap, then ionize the trap optically while repopulating NV^-, and finally measure the trap charge state via NV^- ionization in the dark. In Fig. 3.4(d) we plot the

trap ionization rate Γ_T as a function of 532-nm laser power. We find Γ_T is fit well by a saturation model of $aP^2/(P + P_{\text{sat}})$, where $a = 814(43)$ s$^{-1}/\mu$W, P is laser power, and the saturation power $P_{\text{sat}} = 65(23)$ μW. This power-dependence is consistent with trap ionization by a two-photon transition through an orbital excited state or a single-photon transition where the density of available states $\propto P/(P + P_{\text{sat}})$. In Fig. 3.4(b) we also observe $A(t_{\text{init}} = \infty)$ to increase with laser power. To model this behavior we consider $A(t_{\text{init}} = 0) = 0$, constant trap ionization at rate Γ_T, and constant trap repump at rate Γ_c, which then yields:

$$A(t_{\text{init}}) = \frac{\Gamma_T}{(\Gamma_T + \Gamma_c)} \left(1 - e^{-(\Gamma_T + \Gamma_c)t_{\text{init}}}\right). \tag{3.8}$$

This model qualitatively reproduces the observed saturation behavior since Γ_T increases with power and also indicates that the exponential saturation in Fig. 3.4(b) is actually at a rate $\Gamma_T + \Gamma_c$. Interestingly A never reaches 1, and from the 5 NVs in Fig. 3.3(b), $A = 0.970(1), 0.974(2), 0.972(1), 0.966(5), 0.89(1)$ from left to right. The similar, non-unity values of A in the first 4 NVs could correspond to trap photorecombination at rate 0.03 Γ_T; or trap-NV^0 tunneling at rate 0.03 Γ_c, corresponding to a thermal Boltzmann factor with the trap 0.1 eV lower in energy than the NV.

Physical trap candidates where tunneling could be energetically favorable include vacancy-related complexes, specifically divacancy [80, 91] and surface sp^2 defects [92]. Tunneling to a nearby nitrogen substitutional defect is energetically unfavorable [93]. We do not observe a correlation of Γ_c with NV depth from a subsample of 9 NVs. However, with a low trap density that would be consistent with single trap behavior, we do not expect a strong correlation of Γ_c with NV depth even if all traps are on the surface. Nevertheless, we do observe variations in Γ_c and Γ_T over month timescales or after surface treatments, indicating that the trap properties and the NV-trap tunneling

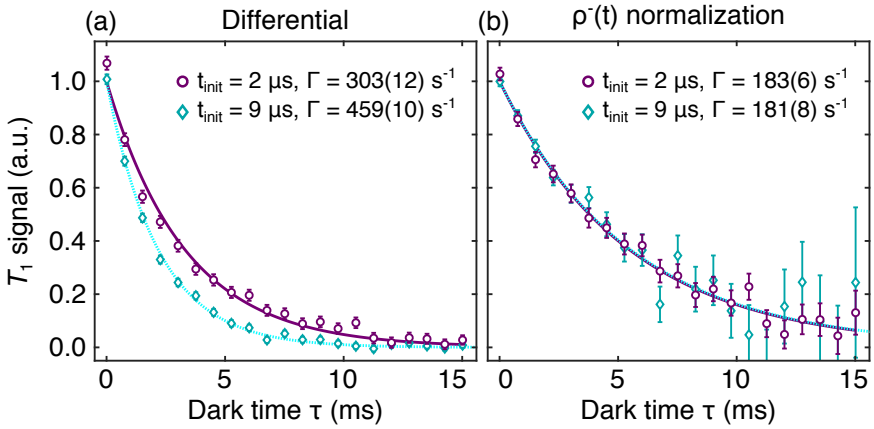

Figure 3.5: Removing the effect of NV^- ionization in the dark from spin measurements. (a) Differential T_1 measurement, measured with a spin-to-charge sequence [74, 60]. Initialization times of 2 μs (purple circles) and 9 μs (blue diamonds) yield substantially different differential T_1 signals and exponential fits (solid and dashed lines, respectively). (b) Normalizing for charge decay during the dark τ time for the signals in (a) renders agreement between the two different measurements and yields spin relaxation rates consistent with other NVs in the same sample ($\Gamma_1 \sim 200 \pm 30\ s^{-1}$).

mechanism depend on the surface.

3.4 Alleviate the charge state conversion effect on NV measurement

We now turn to a discussion of how spin measurements are affected by charge state conversion in the dark and how to alleviate these unwanted effects via various measurement protocols. Due to charge conversion in the dark, the NV^- and NV^0 populations become functions of time, in addition to any spin processes such as T_1 or T_2 decays. Without proper measurement protocols to account for charge conversion in the dark, the added time-dependence can produce misleading signatures in spin measurements. If $\rho^-(t)$ decays with $\Gamma_c \gtrsim 1/T_1$ or $1/T_2$, then one may observe an exponential PL decay which is strictly not spin relaxation or spin dephasing. For example, in Fig. 3.5(a), an exponential fit to a typical T_1 measurement on NVI2 yields different relaxation rates de-

pending on the duration of the green initialization pulse, indicating the presence of other confounding effects that mask the real T_1. This T_1 measurement employs a common-mode rejection technique, referred to as a differential measurement, which is still insufficient to alleviate the effects of charge conversion in the dark. In this differential measurement [94], the 0 and +1 spin state populations are swapped with a resonant microwave π pulse immediately before PL readout (see Chapter 1, section 1.3 for more details), yielding:

$$\mathrm{PL}_{\mathrm{diff}}(t) = \left(\mathrm{PL}_0^- - \mathrm{PL}_1^-\right)\left(\rho_0^-(t) - \rho_1^-(t)\right) \tag{3.9}$$

where $\mathrm{PL}_0^-, \mathrm{PL}_1^-$ are the PL from the $m_s = 0, 1$ states of NV^- with respective populations ρ_0^-, ρ_1^-. In the case of recombination in the dark, the differential measurement is sufficient to remove charge conversion effects because the incoming NV^- population is unpolarized and ρ_0^- and ρ_1^- gain the same additive time-dependence. However, this differential scheme is still insufficient to alleviate the effect of ionization in the dark (the observed effect in this work), because ρ_0^- and ρ_1^- gain a multiplicative time-dependence $\rho^-(t)/\rho^-(0)$. A differential T_1 measurement in the case of ionization in the dark, as in Fig. 3.5(a), yields

$$\mathrm{PL}_{\mathrm{diff},T_1}(t) = C\exp\left(-\Gamma_1 t\right)\left(\rho^-(t)/\rho^-(0)\right) \tag{3.10}$$

where $\Gamma_1 = 1/T_1$ and C describes the contrast between the spin states. For NVI2 presented in Fig. 3.5, it is known (Fig. 3.4) that $\mathrm{t_{init}} = 2$ and 9 μs produce different $\rho^-(t)$, and thus fitting to $\exp(-\Gamma t)$ results in different values of Γ, neither of which are Γ_1. In practice, the bi-exponential decay of $\mathrm{PL}_{\mathrm{diff},T_1}$ may be nearly indistinguishable from a mono-exponential decay with $\Gamma \approx \Gamma_1 + A\Gamma_c$, and so we emphasize that NV^- ionization in the dark requires attention. Specifically, in our sample at room temperature, a naive mono-exponential fit to a differential T_1 measurement would systematically overestimate

Γ_1 of $\sim 25\%$ of the NVs by $> 10\%$. As for the case of both strong ionization and recombination are present, there is no simple method to mitigate the effect on T_1 measurements, unless one could manipulate and characterize the charge state dynamics [1].

It is possible, however, to fully mitigate the effects of charge ionization in the dark on the extracted dynamic NV properties. To do so, one must normalize $\mathrm{PL}_{\mathrm{diff},T_1}$ by $\rho^-(t)$, which is measured separately in the same measurement sequence. In Fig. 3.5(b) we employ such a normalization protocol to recover a T_1 decay free from the effects of ionization in the dark: the data and the fitted values of Γ agree within error for the two different initialization times. The same analysis and mitigation protocol hold for T_2-relevant measurements as well. For recombination in the dark, one could just perform the differential measurement to remove the charge state effect. For ionization in the dark, one could measure $\rho^-(t)/\rho^-(0)$ and use it to divide out its contribution to the differential signal. As for a general case where both ionization and/or recombination, or neither of them are present, one could always just perform differential T_1 measurement first and divide the T_2-relevant measurement signal by $\mathrm{PL}_{\mathrm{diff},T_1}(t)$ [1].

In conclusion, we show that the charge state of near-surface NV centers both under illumination and in the dark depends on the charge configuration of the local environment, and shallow NV centers can exhibit a significantly lower and less stable NV^- population relative to bulk NVs. These observations have direct implications in measurement sensitivity and validity, which can be addressed with various measurement protocols that we present here. We also identify the origin of NV^- ionization in the dark as tunneling to a single local electron trap; we achieve control and readout of the trap charge state and measure its optical ionization properties. Future experiments can use these control and readout capabilities to directly identify the trap's structure and characterize the NV-trap tunneling mechanism [95]. For instance, one can measure NV-trap separation by measuring trap-state-dependent electric fields [96, 97], or one could measure the trap

position in the bandgap by varying the optical excitation energy. Physical identification could then lead to appropriate sample preparation. On the other hand, the NV-trap tunneling mechanism could be utilized for quantitative and highly sensitive measurements of electrochemical potentials or for the production of tunable local electric and magnetic fields for sensing applications, among other potential applications.

Chapter 4

Enhancing NV T_1 relaxometry

Sensing fluctuating electromagnetic fields is crucial for understanding the behavior of solid-state systems [3], for example, the local current and spin fluctuations in magnetic and correlated electron systems [98, 99, 100, 101, 102, 103], decoherence processes in quantum systems [45, 104, 105, 106, 94], and chemical and biological processes [107, 108, 109]. Single-spin quantum sensors emerge as a potent means for this purpose through a method known as relaxometry. In this technique, fluctuating fields that have a spectral component resonant with the energy gap of the sensor spin lead to a shortened relaxation time, T_1 of the sensor [110].

Nitrogen vacancy (NV) centers in diamonds stand out as a prime example of solid-state spin qubit sensors due to their broad operational temperature range, compatibility with biological and condensed matter environments, remarkable sensitivity, and superior spatial resolution. NV centers for relaxometry have enabled the investigation of magnetic fluctuations near the diamond's surface to enhance our understanding of surface-induced decoherence [106, 104, 105, 94], the detection of spin waves within magnetic materi-

The content of this chapter has substantially appeared in the reference [3]: Zhang, Zhiran and Joos, Maxime and Bluvstein, Dolev and Lyu, Yuanqi and Bleszynski Jayich, Ania C., Reporter-Spin-Assisted T_1 Relaxometry, *Phys. Rev. Appl.* **19**, L031004 (2023) © 2023 American Physical Society

als [111, 112], imaging of local conductivity and current flow in condensed matter systems [113, 114, 60, 115], spectroscopy of electronic spins [43], and detection of magnetic nanoparticles [116] and magnetic ions [117, 118, 119].

In our research, we tackle two significant challenges in NV T_1 relaxometry. Firstly, the sensitivity of NV T_1 relaxometry is often limited by the readout fidelity and photon shot noise. In the first section of this chapter, we will discuss the use of the spin-to-charge conversion readout technique to improve fidelity and the photon counts by converting the spin-state information into the charge-state information. Secondly, the proximity of the sensor to its target plays a pivotal role in achieving enhanced spatial resolution and sensitivity. This is especially crucial in relaxometry aimed at detecting individual nuclear or electronic spins, as the dipolar magnetic fluctuation signal from a single spin die off as $1/r^6$, with r being the sensor-target separation [3, 117, 120]. However, NV centers with high-grade spin and optical properties cannot be made arbitrarily shallow because of the low NV yield [121], increased charge instabilities [70, 1, 122] and shorter coherence times [106, 39]. In the second section of this chapter, we will demonstrate the possibility of creating entanglement between NV and an auxiliary reporter spin that is closer to the diamond surface to circumvent this problem.

4.1 Spin-to-charge conversion technique for T_1 relaxometry

The readout efficiency of a qubit can be quantified by the ratio of the actual noise level to the spin-projection noise (SPN) limit. For example, a qubit source is at the superposition of $\frac{1}{\sqrt{2}}|0\rangle + \frac{i}{\sqrt{2}}|1\rangle$, and we will measure either a signal of $S = 1$ for $|1\rangle$ and $S = 0$ for $|0\rangle$. If the readout fidelity of this qubit is 1, meaning the readout signal is only

limited by the uncertainty principle, then the averaged signal results will follow a binomial distribution since each measurement readout is independent. For N measurement shots, the expectation of the mean value of the signal is $\langle S \rangle = 1/2$, with a standard error of the mean being $\sigma_{\mathrm{SPN}} = \frac{1}{\sqrt{4N}}$. If now, in each shot, two measurements are performed (in differential measurement) to determine the spin state, then the errors add in quadrature, so we have $\sigma_{\mathrm{SPN}} = \frac{1}{\sqrt{2N}}$ instead.

For NV center, the conventional readout methods under ambient conditions usually suffer from a readout fidelity up to typically 30%-35% [37], which is the PL difference between $|0\rangle$ and $|\pm 1\rangle$, as well as a low photon count per measurement shot. For example, for the single NV in nanopillar to enhance the collection efficiency, we typically are able to get a PL on the order of 150 kct/s for 400 ns at half saturation for $|0\rangle$, which equals to only 0.06 counts per shot, and a fidelity of 25%. Now if the NV is at the superposition of $\frac{1}{\sqrt{2}}|0\rangle + \frac{i}{\sqrt{2}}|1\rangle$, the photon shot noise limit for N shots of conventional readout is $\sqrt{0.06(1-25\%/2)N} = \sqrt{0.0525N}$. Converting this PL value to the spin coherence S (assuming the PL level of $|0\rangle$ and $|\pm 1\rangle$ are already known), we have a standard error of $\sigma_{\mathrm{shot}} = \sqrt{0.0525N}/0.015N = \frac{1}{\sqrt{0.0043N}} \approx 30.6 \times \sigma_{\mathrm{SPN}}$. Therefore, we lost most of the photon emitted from NV and we are mostly limited by the photon shot noise.

In conclusion, the conventional readout for NV center, in our case, is limited by the low readout fidelity and the low photon counts we collect per shot, to about $30 \times \sigma_{\mathrm{SPN}}$. One approach to improve the readout is to use the spin-to-charge conversion (SCC) readout technique to increase the readout fidelity and the number of photons collected per shot. SCC readout is suitable for room temperature applications and does not need a specific external magnetic field strength. The first kind of SCC technique basically converts the spin-state information to charge-state information and uses a long-duration 594-nm weak laser to selectively excite NV^-'s sideband [74]. The principle and steps of SCC are illustrated in Fig. 4.1(a). Firstly, a 532-nm shelving laser pulse can selectively

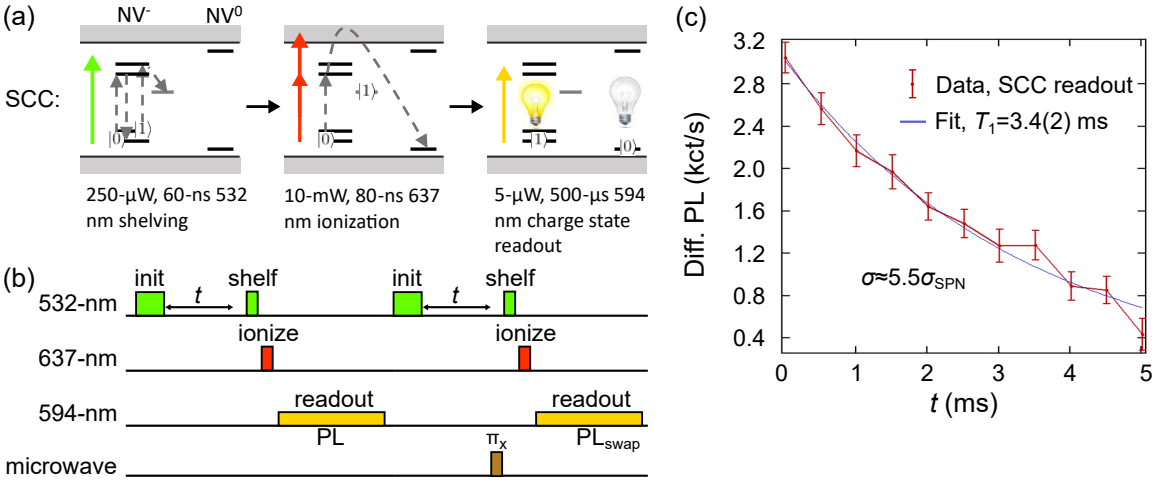

Figure 4.1: Spin-to-charge conversion (SCC) readout technique for NV T_1 relaxometry. (a) The spin-to-charge conversion technique allows for transferring the spin-state dependent population to the charge-state dependent population. The 532-nm shelving pulse only shelves $|\pm1\rangle$ state into the metastable state. Then, before the metastable state decays, a strong 637-nm red pulse ionizes the population not protected in the metastable state into the NV^0. Finally, a weak 594-nm readout pulse selectively excites the NV^- and photons are collected. (b) The pulse sequence for differential T_1 relaxometry with SCC readout. (c) An example of single NV T_1 differential measurement with SCC readout using sequence in (b). The signal plotted is the differential PL which equals to $\mathrm{PL} - \mathrm{PL}_{\mathrm{swap}}$, with a 594-nm readout pulse duration of 500 μs. This data is averaged from 7,200 shots. The noise level achieved is 5.5$\times$ the spin-projection-noise (SPN) limit. The blue solid line is a single-exponential decay fit.

shelve the population from $|\pm1\rangle$ into the metastable state. Secondly, a short, strong 637-nm laser pulse ionizes the NV from its ground state to the conduction band through a two-photon process, while the population in the metastable state remains unchanged before relaxing to the ground state. Therefore, the $|0\rangle$ population converts more to NV^0. Finally, a long weak 594-nm laser is used to selectively excite the NV^-. (The energy to excited state for NV^0 is 2.16 eV, corresponding to 574 nm, while the energy to excited for NV^- is 637 nm. So 594-nm is right in between.) One advantage of SCC readout is that this 594-nm readout features a better PL difference compared to a 532-nm conventional readout of NV^- spin state, even after accounting for the imperfect ionization. Another advantage of SCC readout is that it does not quickly polarize the NV again and destroy the information, so the converted charge state can be read out for a long time.

The actual sensitivity or measurement speed of an NV pulse sequence is also affected by the overhead time, including the time consumed for readout. Therefore, while the noise level of $\sim 10\sigma_{\mathrm{SPN}}$ for short 594-nm readout duration is much lower than conventional readout ($30\sigma_{\mathrm{SPN}}$), the SCC readout technique is even more useful for longer pulse sequence such as T_1 relaxometry [74]. The pulse sequence utilized SCC readout for T_1 relaxometry is illustrated in Fig. 4.1(b). The pulse sequence has a differential measurement structure, wherein in every cycle of the sequence, there are two readout, PL and $\mathrm{PL}_{\mathrm{swap}}$. The NV populations of $|0\rangle$ and $|-1\rangle$ are swapped before the SCC readout for PLswap. We demonstrate the SCC readout enhanced T_1 measurement in Fig. 4.1(c), using a single shallow NV center found in the nanopillar structure in our sample B033. The $|0\rangle$ (still containing effect from imperfect initialization) results in around 8 kct/s for 500 μs 594-nm readout. The PL difference of $\mathrm{PL} - \mathrm{PL}_{\mathrm{swap}}$ is 3.0 kct/s, corresponding to a signal contrast of 37.5%. The standard error of this measurement is $\approx 5.5\sigma_{\mathrm{SPN}}$.

In our work, when the 594-nm readout pulse is set to 500 μs, we usually can achieve a noise level of $\sigma^{\mathrm{SCC}} = 5 \sim 10 \times \sigma_{\mathrm{SPN}}$ in our sample B033, as shown in Fig. 4.1(c)

and Ref. [60, 3]. If also accounting for the error caused by imperfect spin and charge initialization, we can achieve roughly $4 \times \sigma_{\mathrm{SPN}}$, which is comparable to the diamond nanobeam measured in Ref. [74]. For diamond nanobeam, if the 594-nm readout pulse is long enough, the readout fidelity can approach 0.98, and the photon per shot can reach >100 counts, so it is no longer limited by the photon shot noise. In the end, the noise level of $2.76(9) \times \sigma_{\mathrm{SPN}}$ can be achieved [74]. The noise level is eventually limited by the information loss during the shelving-ionization process, where the spin-state information is converted to charge-state information.

When implementing SCC readout on a new experiment setup, one should first calibrate the delay time for the extra two AOMs for 594 nm and 637 nm lasers by using the same pulse sequence for 532 nm but on different AOMs. The laser power for the ionization pulse should be as high as possible to minimize the duration of this pulse. The optimal powers for the charge state readout should be based on the photon statistics analysis and the actual pulse sequence duration, but we typically use the half-saturation power for 532 nm and around 5 μW for 594 nm for T_1 measurement. As for the shelving pulse, the optimal power is still subject to further study since one usually also has to use it for initialization, so the dependence on overall sensitivity can be complex. As for the duration of each pulse, in general, one should roughly optimize them by maximizing the yellow readout signal contrast between 0 and ± 1 states. Overall, a good starting point for all the parameters of laser pulses can be found in Fig. 4.1(a).

For sensing applications, the sensitivity can be a function of the duration of both the readout pulse and free precession time (or dark time for T_1 relaxometry) [110]. One may optimize their duration in order to achieve better sensitivity. For T_1 relaxometry, if we can assume a phenomenological model for the dependence of SCC readout noise level on the readout duration, the optimal readout duration and the optimal dark time can be simultaneously extracted [60, 3]. For example, as shown in Fig. 4.2 [3], we first assume

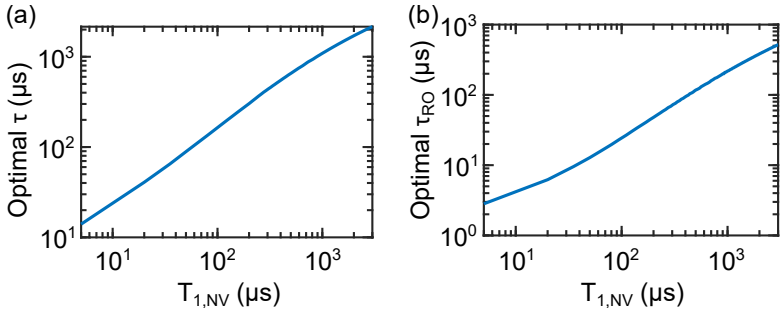

Figure 4.2: Optimize T_1 relaxometry pulse sequence with SCC readout. (a) Dependence of the optimal measurement point τ_r on the relaxation time of reporter spin ($T_{1,\mathrm{NV}}$) to be measured. This is optimized for NV relaxometry with an intrinsic $T_{1,\mathrm{NV}}$=3.5 ms and SCC readout noise. (b) The optimal SCC readout duration τ_{RO} as functions of $T_{1,\mathrm{NV}}$ under the same condition as (a).

the pulse sequence is a differential measurement, and the dark time τ is fixed between shots. In such a scenario, we may define the signal-to-noise ratio (SNR) as:

$$\mathrm{SNR} = \sqrt{2N}\Delta\Gamma_1 \frac{\sigma_{\mathrm{SPN}}}{\sigma^{\mathrm{SCC}}} \left(\frac{\partial S}{\partial \Gamma_1}\bigg|_{\tau} \right), \tag{4.1}$$

where N is the number of measurement shots, the $\Delta\Gamma_1$ is the change of the relaxation rate of NV center, $\Gamma_1 = 1/T_1$, S is the NV coherence (the normalized differential signal), and τ is the dark time in the pulse sequence. Furthermore, we also assume an empirical equation to approximate the noise level we measured from a single NV in sample B033 on our experiment setup:

$$\frac{\sigma^{\mathrm{SCC}}}{\sigma_{\mathrm{SPN}}} = 16.3 - 6.3\frac{\log_{10}(\frac{\tau_{\mathrm{RO}}}{\tau_0})}{\log_{10}(50)}, \tag{4.2}$$

where $\frac{\sigma^{\mathrm{SCC}}}{\sigma_{\mathrm{SPN}}}$ is the ratio of readout noise to spin-projection-noise level, τ_{RO} is the readout duration, and a constant $\tau_0 = 10$ μs. The SCC readout is performed by a sequence of a 60-ns 220-μW 532-nm green shelve pulse, an 80-ns 9.9-mW 637-nm red ionization pulse, and an 8-μW 594-nm yellow readout with varied duration τ_{RO}. We found the optimal τ and readout duration have a positive correlation with the T_1 of the NV center. In a

scanning T_1 experiment, the adaptive measurement may adjust both parameters after each pixel is measured.

4.2 Reporter-spin-assisted T_1 relaxometry

Here we propose an alternative approach that leverages an auxiliary spin that resides closer to, or even at, the diamond surface (Fig. 4.3(a)) to sense fluctuating fields. This reporter spin acts as the relaxation sensor, whereas a nearby NV center, comfortably deeper in the diamond, serves as a local optical readout of the reporter spin state [123, 124]. Compared to direct NV relaxometry, this method features improved sensitivity and spatial resolution while circumventing the reduced NV coherence and charge stability associated with the diamond surface. In essence, the main advantage of the reporter relaxometry method stems from the fact that the reporter translates an incoherent magnetic field signal, which decays as $1/r^6$, into a coherent magnetic signal emanating from the reporter spin with a $1/r^3$ dependence. Furthermore, the proposed approach offers access to an additional range of detection frequencies determined by the reporter spin's energy splitting. In this paper, we analytically examine the dependence of the relaxation signal on NV and reporter spin properties, finding a measurement sensitivity increase up to 100-fold compared to conventional NV relaxometry as relevant parameters are varied in real working conditions. For concreteness, we use a theoretical calculation and a simulation of scanning relaxometry to benchmark performance using a specific example of detecting and imaging a single Gadolinium (Gd^{3+}) ion, a commonly used spin label for bio-structural imaging, but we remark that the results are broadly applicable to other target systems. We then experimentally verify the proposed pulse sequence with a single NV center strongly coupled to a nearby reporter spin, whose relaxation time is tuned via a stochastic driving technique [125]. Finally, the challenges and future outlook

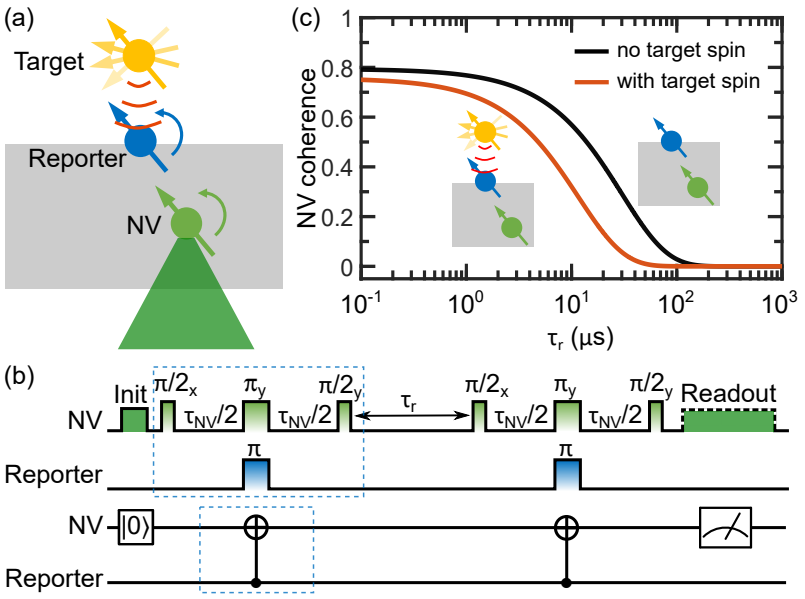

Figure 4.3: (a) Schematic representation of the proposed experiment. The magnetic fluctuations (red contours) from a target spin (yellow) are detected by an optically addressable NV center (green) in diamond, through a change in the relaxation time $T_{1,R}$ of the reporter spin at the diamond surface. The close proximity of the reporter spin to the target spin amplifies the signal. (b) Pulse sequence and corresponding quantum circuit diagram (bottom) used for measuring $T_{1,R}$. After optical initialization of the NV center (dark green), microwave pulses control the spin states of NV center (light green) and reporter spin (blue), followed by optical readout of the NV (dark green).(c) Calculated NV coherence as a function of τ_r as measured by the pulse sequence shown in (b), for an NV that is 4.5 nm deep. In the absence of a target spin, the black curve shows the signal corresponding to the reporter spin's intrinsic T_1, 30 μs in this case. The red curve shows a faster decay when a nearby Gd^{3+} spin, 3 nm from the reporter spin in this case, reduces $T_{1,R}$ to 11.6 μs.

of this proposed approach are discussed.

4.2.1 The protocol of T_1 relaxometry with a reporter spin

We consider a single reporter spin located at the diamond surface near a single NV center, as shown in Fig. 4.3(a). Although the reporter spin can come in any form, its primary requirement is a long intrinsic T_1. We note that single spins at the diamond surface have been detected with 100-μs-scale relaxation times at room temperature [126], which are sufficiently long for the protocols proposed here. For simplicity, we discuss the

case of spin-1/2 reporter spins, but the analysis can be extended to systems with larger spins.

The proposed reporter-spin relaxometry protocol is shown in Fig. 4.3(b). This protocol probes the correlation time of the magnetic field signal produced by the reporter spin, which is equal to its relaxation time $T_{1,R}$, via its dipolar coupling to the NV using double electron-electron resonance (DEER) techniques. The sequence constitutes a correlation measurement of the NV center's environment seen through the filter function set by the "xyy" Hahn echo NV pulse sequence in this case. Importantly, by matching τ_{NV} to the inverse of the NV-reporter dipolar spin coupling rate k_s, the sequence selectively probes the coupling between the reporter spin and NV. Therefore, the two separate "xyy" DEER sequences are equivalent to two CNOT gates in quantum circuit representation [52]. The correlation time of such coupling is then imprinted onto the NV coherence, which can be measured via differential photoluminescence readout of the NV center's spin state [94]. In effect, the NV center acts as a "flag" qubit whose state changes if the reporter spin flips during the correlation sequence [127, 128].

Fig. 4.3(c) shows the expected signal for the example case of detecting a single Gd^{3+} spin, a spin label with a large electronic spin of $S = 7/2$ and fast GHz-scale dynamics [107, 129]. Ensembles of Gd^{3+} spins have been interfaced with and detected by NV centers [117, 120, 119, 130]. The Gd^{3+} produces a rapidly fluctuating magnetic field, which reduces the correlation time of the reporter spin and manifests as a faster NV population decay. The reduction in NV coherence is caused by the relaxation of reporter spin. The NV parameters used in the numerical calculations are experimentally measured on an implanted shallow NV (NV1) in a chemical vapor deposition-grown diamond sample (sample B033). The parameters are $T_2 = 8.4$ μs, and $T_{1,\mathrm{NV}} = 3.5$ ms, and the NV depth is measured via proton NMR [86, 1] to be 4.5 nm. The reporter spin is assumed to be located on the diamond surface at a position where the dipolar coupling to the NV is

maximized, $T_{1,R}$ is assumed to be 30 μs, and τ_{NV} is set to 912 ns to match the inverse of the dipolar coupling strength k_s [124].

4.2.2 Comparison between reporter relaxometry and conventional relaxometry

To quantitatively compare the performance of the proposed reporter-spin-assisted relaxometry protocol with direct NV relaxometry, we first define the sensitivity of a relaxometry measurement as the minimum number of spins detectable per $\sqrt{\mathrm{Hz}}$:

$$\eta = \frac{C_{\mathrm{SPN}}}{\sqrt{2}\Delta S}\sqrt{t_{\mathrm{seq}}}, \tag{4.3}$$

where ΔS is the change of the normalized signal due to the reduced $T_{1,R}$, C_{SPN} is the ratio between experimental measurement uncertainty and the spin projection noise limit, and t_{seq} is the total duration of the pulse sequence including the overhead time, such as the initialization and readout time. The sensitivity of NV relaxometry η_{NV} and sensitivity of reporter relaxometry η_{R} are computed separately using Eq. (4.3) with the corresponding ΔS and t_{seq} for each method respectively.

Next, we outline the steps of the numerical calculation for reporter and NV relaxometry sensitivities. We first calculate how a target fluctuating magnetic field external to the diamond imprints itself on the relaxation time of a single spin, which can be either the NV center when using direct NV relaxometry or the reporter spin when using reporter-spin-assisted relaxometry [44, 120, 131]. For the expected change in T_1, $\Delta S(\tau_{\mathrm{r}})$ is calculated as shown in Fig. 4.3(c). Then using Eq. (4.3), the readout and measurement times are optimized to minimize η_{R} and η_{NV} for each case independently, and the sensitivity enhancement $\eta_{\mathrm{NV}}/\eta_{\mathrm{R}}$ is calculated. We assume the use of the spin-to-charge

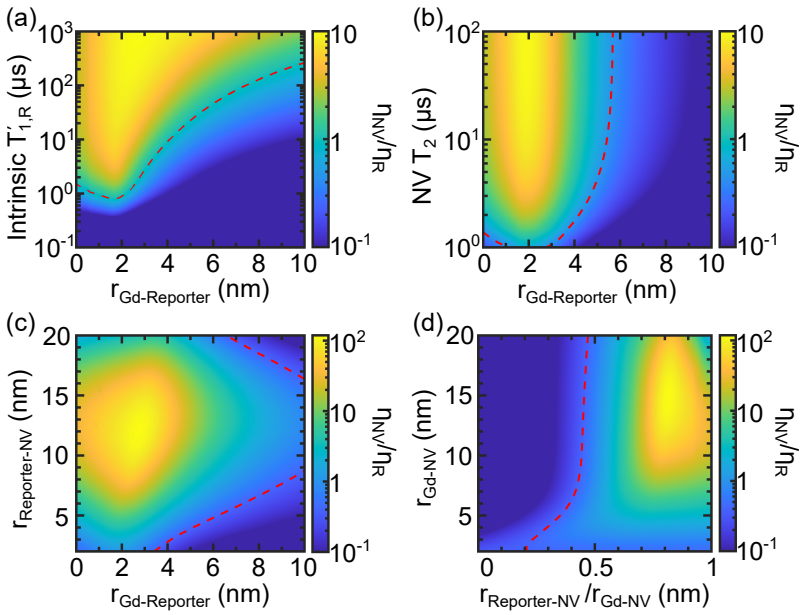

Figure 4.4: Sensitivity improvement of reporter relaxometry over direct NV relaxometry for single Gd^{3+} spin detection. (a) Numerically calculated sensitivity enhancement ($\eta_{\mathrm{NV}}/\eta_{\mathrm{R}}$) as a function of the distance from the Gd^{3+} to reporter ($r_{\mathrm{Gd\text{-}Reporter}}$) and the intrinsic T_1 of the reporter. We assume NV $T_2 = 8.4$ μs, and NV depth is 4.5 nm. (b) $\eta_{\mathrm{NV}}/\eta_{\mathrm{R}}$ as a function of the distance from the single Gd^{3+} to the reporter, and the NV T_2. We assume reporter spin $T_{1,R} = 30$ μs, and NV depth is 4.5 nm. (c)(d) $\eta_{\mathrm{NV}}/\eta_{\mathrm{R}}$ as a function of the distances between NV, reporter, and the single Gd^{3+}. We assume NV $T_2 = 100$ μs and reporter spin $T_{1,R} = 30$ μs. SCC readout technique is used here for both reporter relaxometry and NV relaxometry. The red dashed lines indicate $\eta_{\mathrm{NV}}/\eta_{\mathrm{R}} = 1$, where the sensitivities of two methods are equal.

conversion (SCC) readout technique for all cases here, where the readout noise level is experimentally verified on NV1 [74].

Figure 4.4 plots the sensitivity enhancement of the reporter spin relaxometry protocol over the direct NV relaxometry protocol, varying several parameters to highlight the situations in which reporter spins are an advantageous choice. The qualitative picture that emerges from the plots is that longer intrinsic reporter $T'_{1,R}$, longer NV T_2, smaller reporter-Gd^{3+} separations, and deeper NV centers enhance the benefits of reporter relaxometry, culminating in a 100-fold sensitivity enhancement for a 10-15 nm deep NV with $T_2 = 100$ μs and a Gd^{3+} spin located $\sim$3 nm above a reporter spin with $T'_{1,R} = 30$ μs

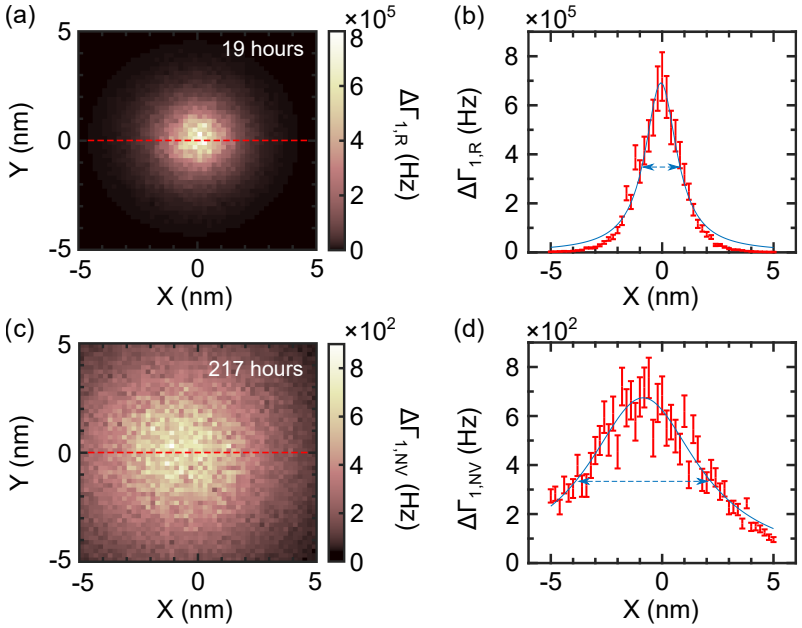

Figure 4.5: A comparison of simulated scanning images of a single Gd^{3+} spin acquired by reporter relaxometry and direct NV relaxometry. (a) Reporter-spin assisted relaxometry image: plotted is the change of reporter relaxation rate, $\Delta\Gamma_{1,R}$, as the reporter spin is scanned in a plane 2 nm above a single Gd^{3+}. (b) A line-cut along the red dashed line in (a). (c) Direct NV relaxometry image plots the change of NV relaxation rate, $\Delta\Gamma_{1,\mathrm{NV}}$, as the NV center is scanned in a plane 6.5 nm above a single Gd^{3+}. (d) A line-cut of the red dashed line in (c). The reporter relaxometry image in (a) takes 19 hours compared to 217 hours for direct NV relaxometry imaging. These simulations target the same level of relative standard error for each pixel. The solid blue lines in (b) and (d) are Lorentzian fits, and the dashed lines with arrows indicate the FWHM. For both images, the NV $T_{1,\mathrm{NV}} = 3.5$ ms, $T_2 = 8.4$ μs, NV depth is 4.5 nm, and the reporter $T_{1,R} = 100$ μs.

(Fig. 4.4(c)(d)). We note that these are all experimentally confirmed values [119, 94, 1, 2]. For each point calculated in Fig. 4.4, the readout and measurement times are optimized to minimize η_{R} and η_{NV} separately, which has been discussed in previous section 5.1.

Reporter relaxometry can also be combined with scanning probe microscopy (SPM) [118, 116, 60, 132] to achieve better spatial resolution and provide faster imaging for a given sensitivity. In reporter-spin-assisted scanning relaxometry, a reporter spin is incorporated onto the apex of a diamond scanning probe tip with a nearby subsurface NV center and is scanned over an imaging target, spatially mapping the fluctuating

fields emanating from the sample. In Fig. 4.5 we compare two simulated images of a single Gd^{3+} spin obtained using scanning reporter T_1 relaxometry (Fig. 4.5(a)) and direct scanning NV T_1 relaxometry (Fig. 4.5(c)). The change of the reporter's relaxation rate is plotted against its lateral position relative to the Gd^{3+} as it is scanned above the diamond surface. Noise at the level of $C_{\mathrm{SPN}} \approx 10$, as experimentally measured on NV1, is included. We utilize an adaptive measurement technique [60] that optimizes the parameters of the pulse sequence (τ_{r} and readout time) at each pixel. We also set the averaging time at each pixel to maintain a constant relative standard error of $\Delta\Gamma_1$, where $\Delta\Gamma_1 = 1/T_1 - 1/T_1^{'}$ is the change in relaxation induced by the Gd^{3+}. We find that reporter relaxometry shows an 11.4-fold overall measurement speed enhancement, and a 3.5-fold better spatial resolution (FWHM resolution) as seen by comparing the signals shown in Fig. 4.5. The FWHM of the signal peaks in Fig. 4.5(b)(d) are limited by the distance between the sensor and target spin.

4.2.3 Proof-of-principle experiment

We now experimentally demonstrate the ability of the proposed sequence (Fig. 4.3(b)) to accurately detect the T_1 reduction of a reporter spin.

Firstly, we will give more information about the fabrication process for our diamond sample (for NV1 in sample B033 and NV2 in another similar sample). The diamond substrate is a 150-μm-thick plate with optically resolvable near-surface NV centers. We use the properties of an NV center (NV1) found in our diamond sample for calculation and simulation and use another NV (NV2) with its nearby strongly coupled spin to perform our proof-of-principle experiment. The same diamond sample is also used and described in references [94, 60, 1, 2].

The details of the fabrication process for sample B033 can be found in Appendix A.

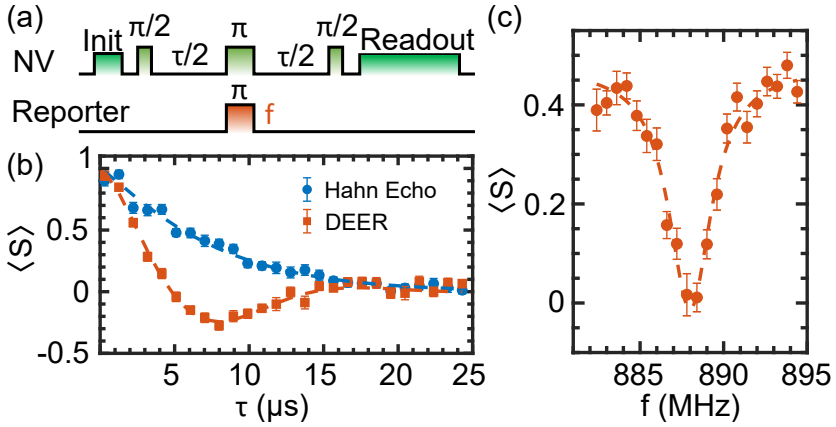

Figure 4.6: DEER measurement of NV2 in a similar sample to B033 with a strongly coupled single dark spin. (a) Pulse sequence of the DEER measurement. (b) Comparison of the Hahn echo decay of NV2 and DEER measurement of the nearby g=2 electron spin. The DEER signal indicates a strong coherence coupling between NV2 and the dark spin. (c) NV coherence as a function of pulse frequency f in the DEER measurement, showing a resonance corresponding to g=2 electronic spins. A π pulse of a duration of 400 ns is used on the dark spin. Dash line is a Lorentzian fit. The external magnetic field is at 317 G.

We identify a single shallow NV (NV1) center in a diamond pillar via a second-order correlation measurement $g^{(2)}(0) = 0.08 \pm 0.04$, and also check the optically detected magnetic resonance (ODMR) spectrum and probability distribution of photon counting under cw 594-nm excitation [1]. We measure the NV $T_2 = 8.4 \pm 0.4$ μs with stretch power $n = 1.16 \pm 0.09$ by fitting the Hahn echo decay with $C\exp[-(\tau/T_2)^n]$. The NV $T_{1,\mathrm{NV}} = 3.5 \pm 0.3$ ms is measured with a spin-to-charge conversion (SCC) readout technique. The NV depth is measured to be 4.5 ± 0.2 nm via surface proton NMR, and further details are given in the supplement of Ref. [1]. NV2 is found to be strongly coupled to a nearby spin and we use it for the demonstration of reporter relaxometry. The NV2's coherence time is measured to be $T_2 = 7.9 \pm 0.4$ μs with a stretch power of $n = 1.2 \pm 0.1$. The double electron-electron resonance (DEER) measurement is fitted with the following equation and shows a strong estimated coupling strength of $k = 0.66 \pm 1$

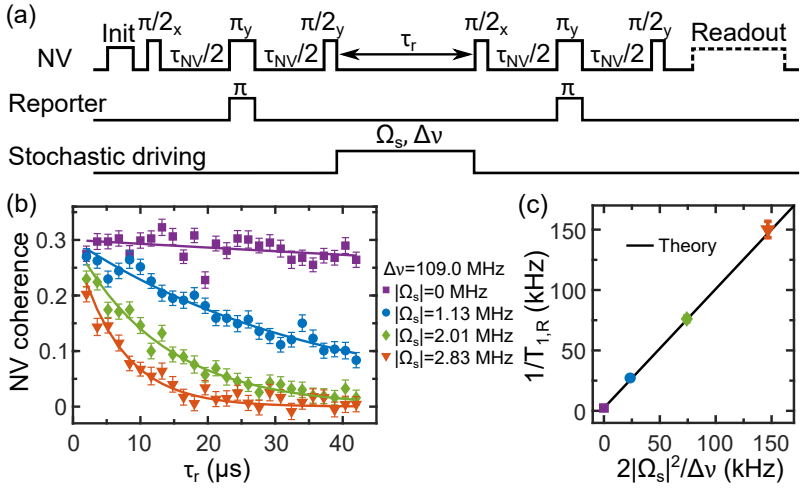

Figure 4.7: Demonstration of reporter relaxometry with artificially reduced reporter spin correlation by stochastic driving. The measurement is performed with a single NV center that is strongly coupled to a nearby g=2 spin-1/2. (a) Pulse sequence of reporter relaxometry with additional stochastic driving of the reporter spin during τ_r. Incoherent spin dynamics caused by stochastic driving with Rabi frequency $|\Omega_s|$ and linewidth $\Delta\nu$ reduces $T_{1,R}$ of the reporter spin. (b) NV coherence for various stochastic driving powers, indicating reduced reporter spin auto-correlation with increased Ω_s. Solid lines are mono-exponential decay fits. This data agrees with our theory model discussed in the next section, Eq. (4.16). (c) Extracted reporter spin relaxation rate as a function of $2|\Omega_s|^2/\Delta\nu$. The black solid line is the theory model, Eq. (4.5).

MHz between the NV2 and the nearby spin (see Fig. 4.6):

$$\langle S\rangle = e^{-(\tau/T_2)^n}\cos\left(\frac{1}{2}k\tau\right), \tag{4.4}$$

where the signal strength $\langle S\rangle$ indicates the NV coherence measured via differential measurements, τ is the NV free evolution time. The differential measurement we used in this paper is the same common-mode rejection technique used in the literature and also described in our previous work [94, 60, 2]. This technique helps alleviate some effects of NV charge state conversion in the dark [1], removing the technical noise and also normalizing the signal.

Finally, in our proof-of-principle experiment, we apply an external stochastic field [125] to a reporter spin located in close proximity to an NV center, thus emulating the

effect of fluctuating fields produced by a sensing target. The polychromatic drive, spectrally centered on the reporter spin resonance, reduces the correlation time of the reporter spin by inducing incoherent spin dynamics; the induced relaxation rate is controlled by the amplitude and broadening of the engineered field:

$$\frac{1}{T_{1,R}} = \frac{1}{T'_{1,R}} + 2\frac{|\Omega_s|^2}{\Delta\nu}. \tag{4.5}$$

where $|\Omega_s|$ is the Rabi frequency of the stochastic drive, and $\Delta\nu$ is the full-width at half maximum linewidth of the Lorentzian spectrum of the drive. We implement the reporter-assisted relaxometry sequence (Fig. 4.7(a)) on a single shallow NV center (NV2) in the diamond that is strongly coupled to a nearby g=2 reporter spin, and we probe the correlation of the reporter spin while turning on stochastic driving centered at 888.0 MHz during τ_r. Figure 4.7(b) shows the reduced correlation of the reporter spin mapped onto the NV coherence as the strength of the stochastic drive is increased. For negligible stochastic drive power ($|\Omega_s| = 0$ kHz), the observed correlation is governed by the intrinsic slow relaxation of the reporter spin, $T'_{1,R} \approx 1$ ms in this case. As the drive power is increased, the reporter spin's correlation time is reduced and dominated by its incoherently driven dynamics. Figure 4.7(c) shows the reporter spin decay rate extracted from a mono-exponential fit to the data in Fig. 4.7(b) as a function of $|\Omega_s|^2/\Delta\nu$. Experimental results agree quantitatively with the expected behavior of Eq. (4.5), demonstrating the suitability of the reporter spin-assisted relaxometry sequence.

4.2.4 Theoretical modeling of the reporter relaxometry

We now further discuss the model of reporter-spin-assisted relaxometry using the theory framework we presented in Chapter 1. In the rotating frame of NV ground states $|m_s = 0\rangle \leftrightarrow |m_s = \pm 1\rangle$ transition, in the i-th shot of the experiment, the phase accu-

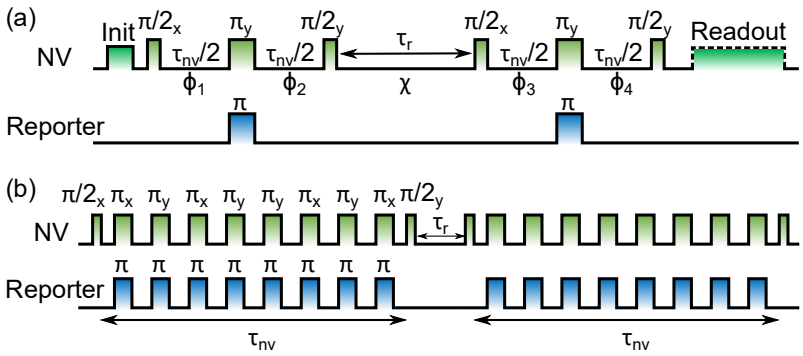

Figure 4.8: (a) The schematic of the pulse sequence for reporter relaxometry. ϕ_i and χ correspond to the phase accumulation of the NV center during free evolution time. (b) The schematic of another pulse sequence of reporter relaxometry using XY8 dynamical decoupling to further mitigate decoherence of NVs caused by environment magnetic noise and pulse errors to increase the signal contrast.

mulation during free precession periods are $\phi_1, \phi_2, \chi, \phi_3$, and ϕ_4 as shown in Fig. 4.8(a). Assuming perfect microwave control pulses, at the end of the pulse sequence, the probability of measuring NV being in $|m_s = 0\rangle$ is given by

$$\begin{aligned} S &= \frac{1}{2} + \frac{1}{2}\cos(\phi_2 - \phi_1)\cos(\phi_3 - \phi_4)\sin(\chi) - \frac{1}{2}\sin(\phi_2 - \phi_1)\sin(\phi_3 - \phi_4) \\ &\approx \frac{1}{2} - \frac{1}{2}\sin(\phi_2 - \phi_1)\sin(\phi_3 - \phi_4) \\ &= \frac{1}{2} + \frac{1}{4}\cos[(\phi_2 - \phi_1) + (\phi_3 - \phi_4)] - \frac{1}{4}\cos[(\phi_2 - \phi_1) - (\phi_3 - \phi_4)]. \end{aligned} \tag{4.6}$$

The term associated with $\langle \sin\chi \rangle$ is considered to be zero here for several reasons. Firstly, the τ_{NV} could be tuned to make sure $\langle \cos(\phi_2 - \phi_1) \rangle$ is as close to zero as possible, thus limiting the effect from $\sin(\chi)$ term. Secondly, when the NV T_2^* is short compared to τ_r, $\langle \sin\chi \rangle$ is close to zero. Lastly, if this phase accumulation remains a problem, it can be alleviated by adding dynamical decoupling sequences on the NV center during τ_r.

The dipole-dipole interaction between the NV center in its ground state $\mathbf{S}$ and the

surface reporter spin **J** can be expressed by the Hamiltonian as follows:

$$H_d = \frac{\mu_0}{4\pi}\frac{\hbar^2\gamma_{\mathrm{NV}}\gamma_R}{r_s^3}\left[\mathbf{S}\cdot\mathbf{J} - 3\frac{(\mathbf{S}\cdot\mathbf{r}_s)(\mathbf{J}\cdot\mathbf{r}_s)}{r_s^2}\right], \tag{4.7}$$

where $\mathbf{r}_s$ is the position of the reporter spin relative to the NV center. γ_{NV} and γ_R are the gyromagnetic ratios of NV and reporter spin. We ignore all the non-secular terms and consider only the terms that commute with S_z and J_z:

$$H_d = \frac{\mu_0}{4\pi}\frac{\hbar^2\gamma_{\mathrm{NV}}\gamma_R}{r_s^3}\left(1 - 3\cos^2\theta_s\right)S_zJ_z, \tag{4.8}$$

where θ_s is the angle between $\mathbf{r}_s$ and the magnetic field. The coupling strength is defined as

$$k_s = \frac{\mu_0}{4\pi}\frac{\hbar\gamma_{\mathrm{NV}}\gamma_R}{r_s^3}\left(1 - 3\cos^2\theta_s\right). \tag{4.9}$$

So we have

$$H_d = \hbar k_s S_z J_z. \tag{4.10}$$

Note that the coupling strength k_s between NV and reporter spin depends on both the distance between them and the angle θ_s. For a 4.5 nm deep NV, if the reporter spin is located on the surface, the maximum coupling strength will be $|k_s| = 3.44$ MHz. In the following derivation, we assume the transition rates between reporter spin states are the same.

Now we consider different sources of decoherence during NV's free evolution time. $\phi_2 - \phi_1$ contains random phases induced by coupling to both other noise sources in the environment $\phi_E^{(i)}$ and the reporter spin.

$$\phi_2 - \phi_1 = \phi_E^{(i)} + \frac{\tau_{\mathrm{NV}}}{2}k_s h_s^{(i)}\sigma_s^z, \tag{4.11}$$

where $\sigma_s^z = \pm 1$, is the spin state of the reporter at the beginning of the pulse sequence in the i-th shot. $h_s^{(i)}$ describes the averaged spin state of the reporter spin during the first "xyy" sequence in the i-th shot of the experiment, and is defined as $h_s^{(i)} = \int \tau_0^{\tau_{\rm NV}} \sigma(t)dt/(\tau_{\rm NV}\sigma(0))$, where the $\sigma(t)$ is the time-dependent spin state of reporter. Let us assume a "telegraph" behavior of the spin states so $\sigma(t)$ only takes the value of ± 1. At the beginning of the second "xyy" sequence, the spin state of the reporter becomes $v_s^{(i)}\sigma_s^z$. Averaging over all shots of the experiment for $v_s^{(i)}$ gives

$$\langle v_s^{(i)} \rangle = e^{-(\tau_r + \tau_{\rm NV})/T_{1,\rm R}}. \tag{4.12}$$

As for $\phi_3 - \phi_4$, we have

$$\phi_3 - \phi_4 = \phi_E'^{(i)} + \frac{\tau_{\rm NV}}{2} k_s h_s'^{(i)} v_s^{(i)} \sigma_s^z. \tag{4.13}$$

If $\phi_E^{(i)}$, $\phi_E'^{(i)}$, $(h_s^{(i)} + h_s'^{(i)} v_s^{(i)})$ and σ_s^z are uncorrelated with each other,

$$\begin{aligned}
\langle \cos[\phi_2 - \phi_1 + \phi_3 - \phi_4] \rangle &= \left\langle \cos\left[\phi_E^{(i)} + \phi_E'^{(i)} + \frac{1}{2} k_s \tau_{\rm NV} (h_s^{(i)} + h_s'^{(i)} v_s^{(i)}) \sigma_s^z \right] \right\rangle \\
&= \sum_{l=0}^{\infty} \frac{(-1)^l}{(2l)!} \left\langle \left(\phi_E^{(i)} + \phi_E'^{(i)} + \frac{1}{2} k_s \tau_{\rm NV} (h_s^{(i)} + h_s'^{(i)} v_s^{(i)}) \sigma_s^z \right)^{2l} \right\rangle \\
&= \sum_{l=0}^{\infty} \frac{(-1)^l}{(2l)!} \sum_{\{n_E, n_s\}} \frac{(2l)!}{(2n_E)!(2n_s)!} \left(\frac{\tau_{\rm NV} k_1}{2} \right)^{2n_s} \left\langle (\phi_E^{(i)} + \phi_E'^{(i)})^{2n_E} \right\rangle \\
&\quad \left\langle \left[(h_s^{(i)} + h_s'^{(i)} v_s^{(i)}) \right]^{2n_s} \right\rangle \\
&= \left\langle \cos\left(\phi_E^{(i)} + \phi_E'^{(i)} \right) \right\rangle \left\langle \cos\left(\frac{1}{2} k_s \tau_{\rm NV} (h_s^{(i)} + h_s'^{(i)} v_s^{(i)}) \right) \right\rangle
\end{aligned} \tag{4.14}$$

Note that $\langle \cos(\phi_E^{(i)} + \phi_E'^{(i)}) \rangle \geq \exp[-(2\tau_{\rm NV}/T_{2,\rm NV})^n]$, with the Hahn-echo decay T_2 and stretch power n. For simplicity and to avoid overestimating the signal, we assume

$\langle\cos(\phi_E^{(i)} + \phi_E^{\prime(i)})\rangle \approx \exp[-(2\tau_{\rm NV}/T_{2,\rm NV})^n]$. Also, $h_s^{(i)}$, $h_s^{\prime(i)}$ and $v_s^{(i)}$ are not correlated with each other and $\langle(h_s^{(i)})^k\rangle = \langle(h_s^{\prime(i)})^k\rangle$, with $k \in \mathbb{Z}$. Therefore, we have

$$\begin{aligned}\langle S\rangle &\approx \frac{1}{2} - \frac{1}{2}e^{-(2\tau_{\rm NV}/T_{2,\rm NV})^n}\left\langle \sin\left(\frac{1}{2}k_s\tau_{\rm NV}h_s^{(i)}\right)\sin\left(\frac{1}{2}k_s\tau_{\rm NV}h_s^{\prime(i)}v_s^{(i)}\right)\right\rangle \\ &= \frac{1}{2} - \frac{1}{2}e^{-(2\tau_{\rm NV}/T_{2,\rm NV})^n}\langle v_s^{(i)}\rangle\left[\frac{1}{2^2}k_s^2\tau_{\rm NV}^2\langle h_s^{(i)}\rangle^2 - \frac{2}{3!}\frac{1}{2^4}k_s^4\tau_{\rm NV}^4\langle h_s^{(i)}\rangle\langle(h_s^{(i)})^3\rangle + ...\right] \\ &= \frac{1}{2} - \frac{1}{2}e^{-(2\tau_{\rm NV}/T_{2,\rm NV})^n}e^{-(\tau_r+\tau_{\rm NV})/T_{1,\rm R}}\left[\sum_{l=0}^{\infty}\frac{(-1)^l}{(2l+1)!}\left(\frac{k_s\tau_{\rm NV}}{2}\right)^{2l+1}\left\langle(h_s^{(i)})^{2l+1}\right\rangle\right]^2.\end{aligned} \tag{4.15}$$

We also consider the effect of NV's relaxation during the pulse sequence here. For a differential measurement, one should add a π pulse on reporter spin before the period τ_r and it will change the sign of $\langle v_s^{(i)}\rangle$ function.

In conclusion, the differential signal for reporter-spin-assisted T_1 relaxometry can be written as

$$\begin{aligned}\langle S\rangle_{\rm diff} =& e^{-(\tau_r+\tau_{\rm NV})/T_{1,\rm R}}e^{-(\tau_r+2\tau_{\rm NV})/T_{1,\rm NV}}e^{-(2\tau_{\rm NV}/T_{2,\rm NV})^n} \\ &\cdot\left[\sum_{l=0}^{\infty}\frac{(-1)^l}{(2l+1)!}\left(\frac{k_s\tau_{\rm NV}}{2}\right)^{2l+1}\left\langle(h_s^{(i)})^{2l+1}\right\rangle\right]^2.\end{aligned} \tag{4.16}$$

where $T_{2,\rm NV}$ is the coherence time of NV, n is the stretch power, and $h_s^{(i)}$ describes the averaged spin state of the reporter spin in the i-th shot of the experiment. The first term in equation (4.16), $\exp[-(\tau_r + \tau_{\rm NV})/T_{1,\rm R}]$ describes the exponential relaxation of the reporter spin. The second term is due to the NV relaxation. The third term $\exp[-(2\tau_{\rm NV}/T_{2,\rm NV})^n]$ is due to NV decoherence during the two Hahn echoes. The last term describes the dipolar coupling between the NV and reporter spin, accounting for reporter spin flips during the two "xyy" echo sequences. The contribution from the T_1 decay of NV is considered in our calculation and simulation, but it is negligible compared

to other terms in most cases where intrinsic $T_{1,NV}$ of the NV is much longer than $T_{1,R}$. The coupling strength k_s can be extracted from the DEER measurement as the signal oscillates with a frequency related to k_s [124].

Now we calculate $\langle (h_s^{(i)})^n \rangle$, where $n = 1, 3, 5, ...$, by deriving the probability distribution function of $h_s^{(i)}$, which is similar to the derivation of the photon statistics of NV charge state dynamics described in the supplement of Ref. [74]. Assume this spin has a relaxation time T_1 and the transition rates between $|\uparrow\rangle$ and $|\downarrow\rangle$ are the same, $1/2T_1$. We consider a process of an odd number, $2k+1$ times of transition between $|\uparrow\rangle$ and $|\downarrow\rangle$ by integrating over τ, where τ is the total time it is in the initial state,

$$\langle (h_s^{(i)})^n \rangle|_{2k+1} = \int_0^{\tau_{\rm NV}} d\tau \left(\frac{2\tau - \tau_{\rm NV}}{\tau_{\rm NV}} \right)^n \frac{\tau_k (\tau_{\rm NV} - \tau)^k}{(k!)^2} (\frac{1}{2T_1})^{k+1} (\frac{1}{2T_1})^k e^{-\frac{\tau_{\rm NV}}{2T_1}}. \tag{4.17}$$

Similarly, we can calculate the situation for $2k$ times of transitions during $\tau_{\rm NV}$. Therefore, by considering all possible k,

$$\begin{aligned} \langle (h_s^{(i)})^n \rangle =& \langle (h_s^{(i)})^n \rangle|_0 + \sum_{k=0}^{+\infty} \langle (h_s^{(i)})^n \rangle|_{2k+1} + \sum_{k=1}^{+\infty} \langle (h_s^{(i)})^n \rangle|_{2k} \\ =& e^{-\frac{\tau_{\rm NV}}{2T_1}} + \int_0^{\tau_{\rm NV}} d\tau \left(\frac{2\tau - \tau_{\rm NV}}{\tau_{\rm NV}} \right)^n \frac{1}{2T_1} \left[\mathrm{I}_0 \left(\frac{\sqrt{\tau(\tau_{\rm NV} - \tau)}}{T_1} \right) \right. \\ & \left. + \sqrt{\frac{\tau}{\tau_{\rm NV} - \tau}} \mathrm{I}_1 \left(\frac{\sqrt{\tau(\tau_{\rm NV} - \tau)}}{T_1} \right) \right] e^{-\frac{\tau_{\rm NV}}{2T_1}}. \end{aligned} \tag{4.18}$$

The $\mathrm{I}_\nu(z)$ is the modified Bessel function of the first kind. The last term comes from the situation where no transition happens during $\tau_{\rm NV}$.

If the reporter spin coupling is too weak compared to the environmental noise during $\tau_{\rm NV}$, the environmental noise can be mitigated by using other dynamical decoupling (DD) sequences instead of the simple "xyy" Hahn echo, for example using XY8 sequence shown in Fig. 4.8(b), as long as the sequence gives the same signal as in Eq. (4.6). The signal

contrast could be further improved by using other DD sequences.

The strength of the dipolar coupling, k_s, can be determined by performing a DEER measurement. For example, we measured k_s =0.66(1) MHz from the DEER measurement shown in Fig. 4.6(b). The measurements use a Hahn echo or other DD sequence to control the NV spin and use corresponding π pulses to control the reporter spin. In conclusion, the expected signal for DEER can be described by the following equation:

$$\langle S\rangle = \frac{1}{2} + \frac{1}{2}\left\langle \cos\left(\phi_2 - \phi_1\right)\right\rangle = \frac{1}{2} + \frac{1}{2}e^{-(\tau_{\mathrm{NV}}/T_{2,\mathrm{NV}})^n}\sum_{l=0}^{\infty}\frac{(-1)^l}{(2l)!}(\frac{1}{2}k_s\tau_{\mathrm{NV}})^{2l}\left\langle (h_s^{(i)})^{2l}\right\rangle . \quad (4.19)$$

This signal is that it has a strong oscillation when τ_{NV} is varied and allows one to extract k_s [124]. When $T_{1,R} \gg \tau_{\mathrm{NV}}$ we retrieve to the familiar form for DEER measurement:

$$\langle S\rangle = \frac{1}{2} + \frac{1}{2}e^{-(\tau_{\mathrm{NV}}/T_{2,\mathrm{NV}})^n}\cos\left(\frac{1}{2}k_s\tau_{\mathrm{NV}}\right), \quad (4.20)$$

which is simply a cosine function with a decaying envelope limited by the NV T_2 coherence time.

4.2.5 Summary and outlook

Our work opens up a broad path of inquiry into a range of possible reporter spin systems that can serve as relaxation sensors without the need for optical initialization and readout capabilities. While engineering single reporter spins at the diamond surface is challenging, there are several promising candidates. Naturally occurring surface spins located on the diamond surface have been detected and measured to have remarkably long $T_1 = 100$ μs [133, 134, 124, 1, 39, 51, 126], though further work is necessary to confirm their microscopic origin and engineer their properties. Reporter spins can also be engineered via ion implantation or chemical synthesis and patterning of molecules

[135, 136], ions encapsulated in fullerene [137], rare-earth ions, and radical spin labels [138, 139].

In conclusion, we propose a method that utilizes reporter spins in conjunction with optically addressable NV centers in diamond to improve the measurement sensitivity and spatial resolution of conventional NV T_1 relaxometry sensing and imaging. We quantitatively compare the sensitivity and spatial resolution of this method to conventional NV T_1 relaxometry and find a wide range of parameter space in which reporter spin relaxometry provides substantial gains. Proof-of-principle experiments confirm the ability of the proposed sequence to quantitatively probe the relaxation of a single, dark reporter spin. This work motivates the development of engineered reporter spins and some candidates are proposed.

Chapter 5

Two-dimensional NV spin systems in PECVD-grown diamond

5.1 Many body noise in strongly interacting dipolar spin systems

Current methods of generating high-density NV centers in diamond, including ion implantation or nitrogen doping during growth, inevitably also create a comparable density of substitutional nitrogens (P1 centers) and other defects or surface-related spins [4]. On the one hand, the many-body noise from these other defects limits the coherence time of the NV centers, which deteriorates the performance of many NV applications. Therefore, it is essential to understand the nature of it. On the other hand, such a strongly interaction spin system itself is an interesting many-body system to study, and could be useful

The content of this chapter has substantially appeared in the reference [4]: Hughes, Lillian B. and Zhang, Zhiran and Jin, Chang and Meynell, Simon A. and Ye, Bingtian and Wu, Weijie and Wang, Zilin and Davis, Emily J. and Mates, Thomas E. and Yao, Norman Y. and Mukherjee, Kunal and Bleszynski Jayich, Ania C., Two-dimensional spin systems in PECVD-grown diamond with tunable density and long coherence for enhanced quantum sensing and simulation, *APL Materials* **11**, 021101 (2023)

for discovering novel phases of matter and developing new correlated sensing protocols [3, 124, 140, 141, 142].

The dipolar interaction between spins in diamond can be captured by a more general Hamiltonian for Ising interactions,

$$H_z = \sum_i \frac{J_z g_i}{r_i^\alpha} \hat{s}_p^z \hat{s}_i^z, \tag{5.1}$$

where J_z is the interaction strength, g_i is the angular dependence in the interaction, r^α is the distance between i-th spin to the probe spin, $\hat{s}_p$ is the probe spins which is the NV center in our case, and $\hat{s}_i$ is the spins in the bath (called system spins or system spins), which can be considered to be P1 centers or others. We focus only on this Hamiltonian term because, in most cases, (i) the T_1 of these spins are on a much longer time scale, (ii) the NV is not in resonance with other defects, including P1 centers, and (iii) the interaction between spins is highly off-resonant. This Hamiltonian can also be understood as the dipolar interaction between spins that are off-resonance under secular approximation. The following discussion assumes the pulse sequence starts and ends with two $\pi/2$ pulses. Therefore, the coherence now can be defined as $C(t) = 2\left\langle \hat{s}_p^x(t) \right\rangle$. And the filter function of the pulse sequence is defined in the same way as Eq. (1.32).

5.1.1 Decoherence dynamics due to Gauss-Markov noise in a semi-classical picture

Following the derivation in Ref. [142] which collects many ideas from previous works [143, 144, 145, 146, 147, 148, 149, 55, 150, 151, 152, 153], we now treat the spin operators as fluctuating classical variables $s_i^z(t)$ instead, and derive the decoherence dynamics assuming a Gauss-Markov noise source.

In our experiments, when the density of NV is high, one can usually measure many NVs together with a confocal microscope. Similar to Eq. (1.31), the ensemble average of the coherence over all trajectories is:

$$C = 2\left\langle \hat{s}_p^x(t)\right\rangle = \langle \mathrm{Re}\left[\exp\left(-i\phi(t)\right)\right]\rangle\,, \tag{5.2}$$

where

$$\phi(t) = \sum_i \frac{J_z g_i}{r_i^\alpha}\int_0^t s(t')s_i^z(t')dt'. \tag{5.3}$$

Here, we still assume $\phi(t)$ and $s_i^z(t)$ are captured by a Gauss-Markov process which is the same as previous works, including Ref. [55], so that we have

$$C = \exp\left(-\left\langle\phi^2\right\rangle/2\right) = \prod_i \exp\left\{-\frac{1}{2}\left[\frac{J_z|g_i|\chi(t)^{1/2}}{2r_i^\alpha}\right]^2\right\}. \tag{5.4}$$

The $\chi(t)$ is the convolution of the correlation function of i-th spin and the step function $s(t)$ for the pulse sequence:

$$\chi(t) = 4\left\langle\left[\int_0^t s(t')s_i^z(t')dt'\right]^2\right\rangle = \int_0^t dt'\int_0^t s(t')s(t'')\left\langle 4s_i^z(t')s_i^z(t'')\right\rangle, \tag{5.5}$$

where the factor of 4 is used to normalize the spin numbers when both probe and system spins are spin-1/2 particles. Because we have assumed the Gauss-Markov process for $s_i^z(t)$, the correlation function can be explicitly written as:

$$\xi(\tau) = \langle 4s_i^z(t')s_i^z(t'')\rangle = e^{-|\tau|/\tau_c} \tag{5.6}$$

where tau_c is the correlation time of the spin bath (P1 centers or other spins). Again, this correlation function is the Fourier transform of the noise spectrum $\tilde{S}(\omega)$. Given this

specific form of correlation function, the $\chi(t)$ for any pulse sequence can be solved.

Sequence	$\chi(t)$	Early-time ($t \ll \tau_c$)	Late-time ($t \gg \tau_c$)
Ramsey(DEER)	$2\tau_c t - 2\tau_c^2(1 - e^{-t/\tau_c})$	$t^2 - \frac{t^3}{3\tau_c}$	$2\tau_c t - 2\tau_c$
Hahn Echo	$2\tau_c t - 2\tau_c^2(3 + e^{-t/\tau_c} - 4e^{-t/2\tau_c})$	$\frac{t^3}{6\tau_c}$	$2\tau_c t - 6\tau_c$
XY8	$\frac{\tau_p^2}{12\tau_c}t$	$\frac{\tau_p^2}{12\tau_c}t$	$\frac{\tau_p^2}{12\tau_c}t$

For double electron-electron resonance, π pulses drive both probe spin and system spins, so the filter function is effectively the same as Ramsey. For XY8, the τ_p is the interval time between the π pulses. In theory, by shortening the τ_p and increasing the number of π pulses, the coherence of XY8 can approach the time scale only limited by intra-group NV-NV interaction. But sometimes, this is difficult to achieve in the experiments since there are always pulse errors and decoherence during the microwave pulses.

One can observe the averaged decoherence dynamics over positional disorder by just measuring a large number of NVs, where the positions of NVs and P1s, for example, are totally random in some sense. By Eq. [5.4], we can already use numerical simulation to investigate the decoherence profile with varying parameters. One could also derive the analytical form when assuming the probability density of positions of spins is completely homogeneous in an infinite volume in the D dimensions. After averaging Eq. (5.4) over N system spins, we have:

$$\begin{aligned} C(t) &= \exp\left\{ -\frac{n}{\alpha}\left(\frac{J_z\chi(t)^{\frac{1}{2}}}{2}\right)^{\frac{D}{\alpha}}\left[\int_0^\infty dz(1-\cos(z^2))z^{-\frac{D}{\alpha}-1}\right]\int d\Omega|g|^{\frac{D}{\alpha}}\right\} \\ &= \exp\left\{ nA\frac{D\pi^{\frac{D}{2}}\Gamma(-\frac{D}{2\alpha})}{\alpha\Gamma(\frac{D}{2}+1)2^{1+\frac{D}{2\alpha}}}\left[\frac{1}{2}\bar{g}J_z\chi(t)^{\frac{1}{2}}\right]^{\frac{D}{\alpha}}\right\}, \end{aligned} \tag{5.7}$$

where $z = \frac{J_z|g|\chi(t)^{1/2}}{2r^\alpha}$ is a substitution, n is the D-dimensional density of system spins,

and $\bar{g} = \left(\frac{\int |g|^{D/\alpha} d\Omega}{\int d\Omega}\right)^{\alpha/D}$ is the angular dependence of the interaction averaged over the D-dimensional solid angle. There is a factor of $A = \frac{\cos(\frac{D\pi}{2\alpha})\Gamma(\frac{1}{2}-\frac{D}{2\alpha})}{\sqrt{\pi}2^{D/2\alpha}}$, coming from the fact that we haven't impose the phase accumulation being Gaussian. Here $A = \approx 1.25$ for $D = 3$ and $D = 2$ when $\alpha = 3$. If assuming Gaussian phase accumulation, the term $(1 - \cos(z^2))$ will become $(1 - e^{-z^2/2})$, and we will have $A = 1$. Therefore, there is only a small difference between the two assumptions about phase accumulation statistics, and experimentally, it is hard to distinguish them. The assumption of Gauss-Markov noise versus telegraph noise (quantum jumps in the $s_i^z(t)$) will lead to a difference of stretch power in the early-time Hahn echo decay [142]. For Gauss-Markov, we have $n = 3D/2\alpha$, while for telegraph noise, we have $n = 1 + D/\alpha$. In Ref. [142], the $n = 3/2$ is observed in a 3D NV layer, thus confirming the assumption of Gauss-Markov noise.

For our experiment, the system spins are oftentimes P1 centers or other unknown spin-1/2, and it's either 2-dimensional or 3-dimensional. The interaction between P1 and NV centers is the magnetic dipole-dipole interaction, so the angular dependence is explicitly $g = 1 - 3\cos^2\theta'$, where θ' is the angle between the NV axis and the distance vector connecting NV and P1 centers. In [100] diamond sample, where the NV axis is $\arccos(1/\sqrt{3})$ to the normal to the plane of 2D system spins, for $\alpha = 3$, $D = 2$, we have $\bar{g} = 0.6023$. In [111] diamond sample, where the NV axis is 0 degrees to the normal to the plane of 2D system spins, for $\alpha = 3$, $D = 2$, we have $\bar{g} = 1$. In both [100] and [111] diamond samples, for $\alpha = 3$, $D = 3$, we have $\bar{g} = 1.008$. After computing all the terms explicitly, for a 2D sample, where both probe spins and system spins reside in a thin 2D layer, we have:

$$C(t) = \exp\left[-n(a_{2\mathrm{d}}J_z)^{\frac{2}{3}}\chi(t)^{\frac{1}{3}}\right], \tag{5.8}$$

where $J_z = \mu_0\hbar\gamma_e^2/4\pi = 2\pi \times 52$ MHz·nm^3 (μ_0 is the vacuum permeability and γ_e is the gyromagnetic ratio of free electron), and $a_{2\mathrm{d}} \approx 1.87$ for [100] diamond sample, $a_{2\mathrm{d}} \approx 3.10$

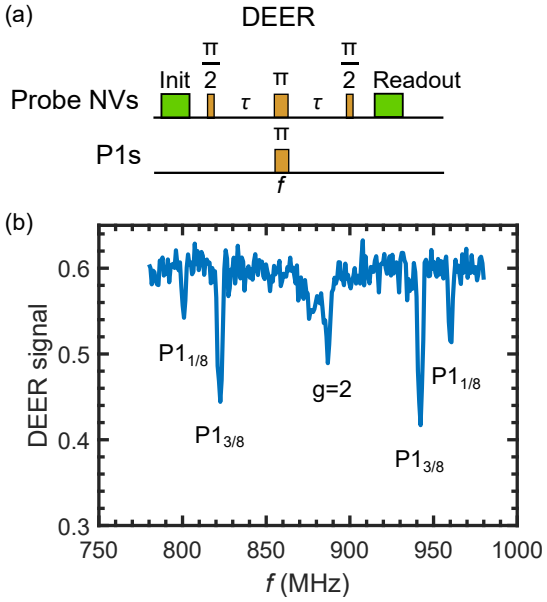

Figure 5.1: DEER measurement of P1 centers. (a) The pulse sequence of DEER measurement. The microwave pulse on the second row is driving one of the P1 transitions. (b) The DEER spectrum taken by varying the frequency of the π pulse driving the P1s. Four transition peaks of P1s caused by Jahn-Teller distortion are observed here. Each $P1_{3/8}$ peak is degenerated from three transitions. The data is taken from sample L021.

for [111] diamond sample. If assuming $A = 1.25$ instead, we have $a_{2d} \approx 2.61$ for [100] sample, $a_{2d} \approx 4.34$ for [111] sample. As for 3D sample, we have:

$$C(t) = \exp\left[-n a_{3d} J_z \chi(t)^{\frac{1}{2}}\right], \tag{5.9}$$

where $a_{3d} \approx 2.65$. And if assuming $A = 1.25$, $a_{3d} \approx 3.31$. Lastly, note that the derivation above assumes the system spins are spin-1/2, so there should be an extra factor of 2 before J_z, for example, when considering intra-group NV-NV interaction so the system spins are NV centers.

5.1.2 Decoherence due to multiple species of system spins

Furthermore, one could model the decoherence when having multiple species of system spins. For a Hahn echo measurement, we can denote the signal contribution from a specific group ν of system spins as $E_\nu(t)$. For example, for interaction with 2D spin-1/2 system spins, we have:

$$E_\nu(t) = \exp\left\{-n_\nu(a_{2\mathrm{d}}J_z)^{\frac{2}{3}}\left[2\tau_c t - 2\tau_c^2(3+e^{-t/\tau_c}-4e^{-t/2\tau_c})\right]^{\frac{1}{3}}\right\}. \tag{5.10}$$

Similarly, we can denote the signal contribution from a specific group ν of system spins as $R_\nu(t)$ for Ramsey or DEER measurement. For example, the ^{15}N P1 centers have 8 electron resonance levels caused by the Jahn-Teller distortion, and some of them can be degenerated at room temperature. When the external field is aligned to the probe NV axis, assuming all transitions have an equal population, we end up with $\nu = 3/8, 3/8, 1/8, 1/8$ four resonance lines, as shown in Fig. 5.1. If only considering inter-group NV-NV interaction and interaction with P1 centers, the resulting Hahn echo measurement decoherence profile will be:

$$E(t) = R_{\mathrm{inter,nv}}(t)[E_{\frac{3}{8}}(t)]^2[E_{\frac{1}{8}}(t)]^2. \tag{5.11}$$

For another example, the DEER measurement with driving the $\nu = \frac{3}{8}$ group, we have:

$$R(t) = R_{\mathrm{inter,nv}}(t)R_{\frac{3}{8}}(t)E_{\frac{3}{8}}(t)[E_{\frac{1}{8}}(t)]^2. \tag{5.12}$$

In practice, for example, we are often interested in knowing the density of the P1 centers. However, even the DEER measurement contains contributions from inter-group NVs, other groups of P1 transitions, and other unknown spins. Therefore, we often normalize the DEER signal by the Hahn echo signal to extract the decoherence due to interaction

with a specific group of P1:

$$\frac{R_{\exp}(t)}{E_{\exp}(t)} = \frac{R_\nu(t)}{E_\nu(t)} = \frac{\exp\left\{-n_\nu(a_{2\mathrm{d}}J_z)^{\frac{2}{3}}\left[2\tau_c t - 2\tau_c^2(1-e^{-\frac{t}{\tau_c}})\right]^{\frac{1}{3}}\right\}}{\exp\left\{-n_\nu(a_{2\mathrm{d}}J_z)^{\frac{2}{3}}\left[2\tau_c t - 2\tau_c^2(3+e^{-\frac{t}{\tau_c}}-4e^{-\frac{t}{2\tau_c}})\right]^{\frac{1}{3}}\right\}}. \tag{5.13}$$

In the early-time regime, $t \ll \tau_c$, therefore we have:

$$\frac{R_{\exp}(t)}{E_{\exp}(t)} \approx \exp\left[-n_\nu(a_{2\mathrm{d}}J_z)^{\frac{2}{3}}t^{\frac{2}{3}}\right]. \tag{5.14}$$

So the DEER signal normalized by Hahn echo will have a stretch power of 2/3 if the spins are located in a two-dimensional layer with a small thickness. If the spins are three-dimensional, then the stretch power should be 1 instead. Therefore, such a signal can also inform the dimensionality of the spin system.

5.2 Two-dimensional NV ensemble created through delta-doping or ion implantation

Creation of dense one-dimensional or two-dimensional NV ensemble spin layers in diamond is a promising experimental approach towards observing the unique many-body phenomenon in the strongly interacting spin system [154, 155, 156, 157, 158]. Increasing the density of NVs while maintaining the NV properties is also a big challenge for improving the sensitivity in many sensing applications [110, 24, 25]. Furthermore, reduced dimensionality is necessary for generating phenomena, including the spin squeezing via dipolar interaction, which enables enhanced metrological sensing protocol beyond standard quantum limit [159, 160, 161, 162, 142].

In order to generate NV center layers in diamond with nanometer-scale thickness,

there are two common methods, delta doping and ion implantation, to introduce a high density of nitrogens into diamond [24, 35]. Because of the low density of vacancies after the delta-doping plasma-enhanced chemical vapor deposition (PECVD) growth, transmission electron microscopy (TEM) or similar techniques are often used to create more vacancies to further increase the NV density [4]. We now discuss the interesting phenomenon in two-dimensional spin systems we created in two diamond samples, one by delta doping and one by ion implantation.

5.2.1 Two-dimensional spin systems created by delta-doping PECVD diamond growth

We fabricated two diamond samples with the same procedures [4]. The growth uses the plasma-enhanced chemical vapor deposition (PECVD) technique (SEKI SDS6300 reactor), and a delta-doped layer is created to have an FWHM thickness of 3.55(4) nm and a depth of around 95 nm. After growth, the transmission electron microscope (TEM) (ThermoFisher Talos F200X G2) with 200 keV electrons was used to further augment the NV density by creating more single vacancies. Sample L026 is prepared with the same procedure, resulting in a delta-doped layer that has an FWHM thickness of 4.06(7) and a depth of 90 nm.

We developed a method to estimate the NV density of the NV ensemble by measuring the fluorescence intensity of the difference between $m_s = \pm 1$ and $m_s = 0$ states ($\Delta\mathrm{PL_R}$). The $\Delta\mathrm{PL_R}$ of a single NV is measured first and averaged from several single NVs with the laser power tuned to the half-saturation. The saturation curve of NVs is the measurement of PL dependence on laser power at the back aperture of the objective and fitted to $\mathrm{PL} = a\frac{P}{P+P_{\mathrm{sat}}}$ where P_{sat} is the saturation power. Then $\Delta\mathrm{PL_R}$ is measured by Rabi oscillation. With our experiment setup, the point spread function (PSF) of a single NV

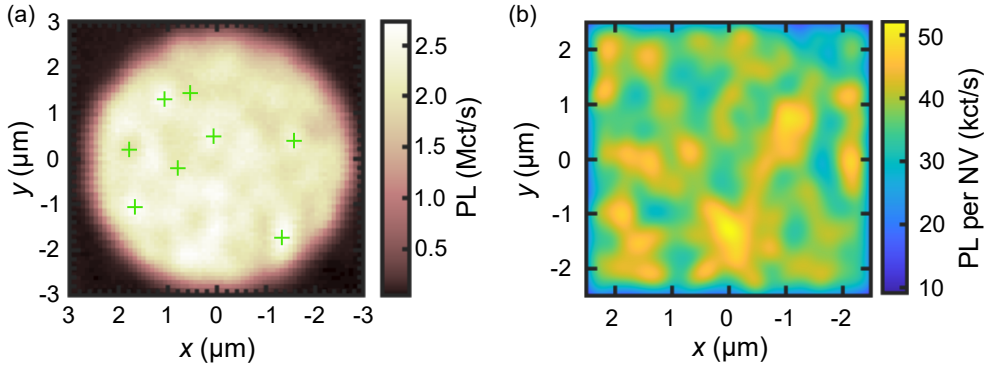

Figure 5.2: (a) The confocal PL image of a TEM irradiated spot in our diamond sample L021. The electron dosage is 5.4×10^{19} cm^{-2}. The 532-nm laser power is around 1.6 mW at the back aperture. The green crosses mark where Rabi measurements are taken. (b) The simulated PL image of NV ensemble. The PL from a single NV is assumed to be a Gaussian function with an amplitude of 25.04 kct/s and linewidth of $\sigma_x = 174$ nm, $\sigma_y = 208$ nm.

can be modeled by a 2D Gaussian function:

$$\mathrm{PSF}(x, y) = c + A \exp\left[-\frac{(x - x_0)^2}{2\sigma_x^2} - \frac{(y - y_0)^2}{2\sigma_y^2}\right], \tag{5.15}$$

where c is the PL background, σ_x and σ_y are the linewidths in two directions. Experimentally, we measured several single NVs found in unirradiated areas in sample L021. We observed $\sigma_x = 174(5)$ nm and $\sigma_y = 208(7)$ nm. The small asymmetry of the PSF is consistent between single NV, which we attribute to the imperfect optical alignment at the time of experiments. The rabi contrast $\Delta\mathrm{PL_R}$ should also be subject to the same optical response and thus can be modeled by the same equation except for a $c = 0$ and a lower A. The PL image of the NV ensemble can then be understood as just the overlapped images of single NVs and a near-constant background (c in Eq. [5.2.1]). We performed a numerical simulation to demonstrate such an effect in Fig. 5.2(b). Assuming all four axes of NVs have the same density, the total density of NV can be estimated by

Dosage(/cm^2)	Rabi-PL(ppm·nm)	$(XY8)_n$ (ppm·nm)	NV-NV DEER (ppm·nm)
5.4×10^{19}	2.6(9)	4.0(2)	1.4(2)
6.8×10^{19}	3.6(2)	3.0(2)	1.6(1)

Table 5.1: Comparison of three NV density estimation methods. Data were taken on two TEM spots from two similar diamond samples. The 5.4×10^{19} e$^-$/cm^2 spot is from sample L021 while the 6.8×10^{19} e$^-$/cm^2 spot is from sample L026.

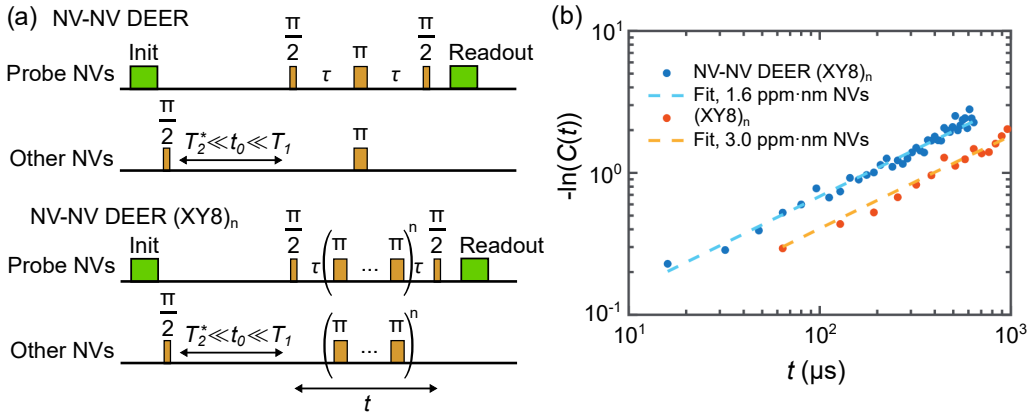

Figure 5.3: (a) The pulse sequences of the NV-NV DEER and NV-NV DEER $(XY8)_n$. The first $\pi/2$ pulse for the other NVs is to ensure the NVs have decohered, while the probe NVs are still largely polarized, therefore we use $T_2^* \ll t_0 \ll T_1$. (b) The NV-NV DEER $(XY8)_n$ measurement and $(XY8)_n$ measurement on an irradiation spot of 6.8×10^{19} e$^-$/cm^2 in sample L026. Both signal curves show a stretch power of 2/3, indicating the NVs are located in a two-dimensional layer.

relating ΔPL_R of single and ensemble NVs by:

$$n_{nv} = 4\frac{\Delta PL_{R,ensemble}}{\Delta PL_{R,single}}\frac{1}{f_{avg}}, \tag{5.16}$$

where the averaged conversion factor is $f_{avg} = 38(8)$ ppm^{-1}nm^{-1} extracted from simulation. For example, we now can estimate the total NV density to be 2.6(9) ppm · nm averaged from 8 locations in the TEM spot shown in Fig. 5.2 (marked by green cross), where we performed other experiments in Ref. [142] including the Rabi contrast measurement ($\Delta PL_{R,ensemble} = 201 \pm 24$ kct/s).

The NV density can also be estimated via other methods, including the following two

approaches. Firstly, the NV-NV interaction can be utilized since it is dependent on the density, quantization axis, and dimensionality of the NV ensemble. For example, $(XY8)_n$ pulse sequence can mitigate the interaction with other noise source including P1 centers, while not suppressing the interaction between NVs that in the same axis. Therefore, when pushing the coherence time to the maximum one can achieve by using more cycles of XY8 (larger n) and decreasing the interval between pulses, an upper limit estimation of the NV density can be extracted from the decay signal. The dipole-dipole interaction between NV spins under secular approximation should be:

$$H_{i,j} = \frac{J_z(3\cos^2\theta - 1)}{r_{i,j}^3} 2(\sigma_{i,x}\sigma_{i,y} + \sigma_{i,y}\sigma_{i,y} - \sigma_{i,z}\sigma_{i,z}). \tag{5.17}$$

Note that the factor before $\sigma_{i,z}\sigma_{i,z}$ is 1 here, while it is 2 for spin-1/2 spin systems. For simplicity, we adopt the model we discussed in the previous section, ignoring the $\sigma_{i,x}\sigma_{j,x}$ and $\sigma_{i,y}\sigma_{j,y}$ terms, as well as the contribution from all other decoherence sources, we have:

$$C_{\mathrm{XY8}}(t) \approx \exp\left[-n_{\mathrm{inter,NV}}(2a_{\mathrm{2d}}J_z)^{\frac{2}{3}}t^{\frac{2}{3}}\right], \tag{5.18}$$

for early-time regime (τ_c of NV bath is much longer than free precession time t), where the $n_{\mathrm{inter,NV}}$ is one-fourth of the total NV density, and the extra factor of 2 comes from the spin number of NV centers being 1 instead of 1/2. Secondly, we can directly probe the interaction between the group of NVs aligned with the external B field and all other misaligned NVs. For example, this can be achieved by measuring the NV-NV DEER signal, as shown in Fig. 5.3(a). In order to mitigate other noise more strongly, we performed NV-NV DEER $(XY8)_{\mathrm{n}}$ measurement, which still preserved the interaction between NVs [157]. Therefore, the signal decay shown in Fig. 5.3(b) has at least the contribution from both intra-group NV-NV interaction, which cannot be removed by

XY8 sequence, and the inter-group NV-NV interaction. However, one problem is that the other three groups of NVs have different quantization axes and thus cannot be driven by appropriate microwave pulses simultaneously. So we argue that such measurement is a lower limit estimate of the NV density:

$$C_{\text{NV-NV}}(t) > R_{\text{NV,total}}(t) = \exp\left[-n_{\text{NV,total}}(2a_{2\text{d}}J_z)^{\frac{2}{3}}t^{\frac{2}{3}}\right], \tag{5.19}$$

where $n_{\text{NV,total}}$ is the total NV density. We also performed a numerical simulation for DEER, XY8, and NV-NV DEER measurement, and the details can be found in Ref. [4].

A comparison of these three approaches to estimate NV density is summarized in table 5.1, over two specific TEM spots from sample L021 and sample L026. Experimentally, we found the estimation method by Rabi PL is the most convenient approach, and it generally agrees with the other two methods. We also note that such Rabi PL estimation may suffer from two main drawbacks. Firstly, other effects, including the difference of charge state instability between single and ensemble NVs, may cause a wrong estimate. Secondly, the diamond sample may not have single NVs to calibrate the PL measurement. Nevertheless, such a method is useful for quickly estimating NV density and providing feedback for research processes such as diamond growth. We also noticed there is a trend that the estimation from XY8 is higher than from NV-NV DEER, which is consistent with our expectation for the limitation of these two methods.

With the information about the density of NV and P1 centers at the same location in the diamond, one may calculate the expected contribution from NV and P1 in the Hahn echo decay. For example, as shown in Fig. 5.4, we analyze the DEER and Hahn echo decay using such an approach. The total NV density is estimated to be 3.39 ppm·nm by the aforementioned Rabi PL method. The total P1 density is estimated by fitting the DEER signal normalized by the Hahn echo signal by Eq. 5.1.2, as shown in Fig.

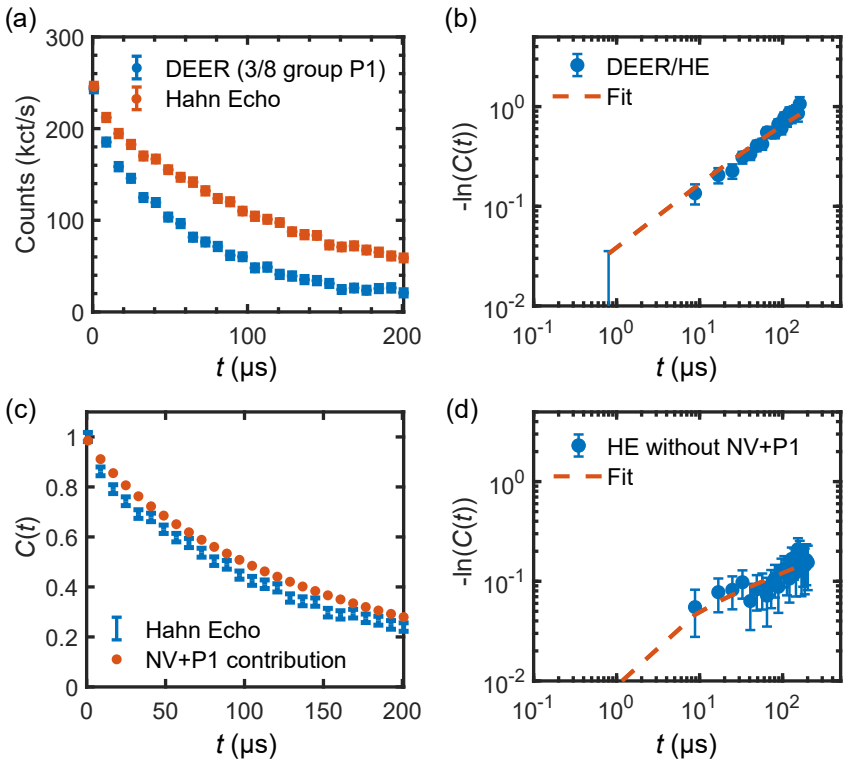

Figure 5.4: The analysis of NV and P1 contribution to Hahn echo decay. (a) The Hahn echo and DEER measurement. The DEER measurement is using the sequence shown in Fig.5.1(a), driving a $P1_{3/8}$ transition. (b) The DEER signal normalized by the Hahn echo signal. The dashed line is fit by Eq. [5.1.2], assuming a two-dimensional P1 and NV layer, in the early-time regime. The density of $P1_{3/8}$ extracted is 2.59(7) ppm·nm, thus corresponds to a total P1 density of 6.9(2) ppm·nm. (c) The Hahn echo decay compared to the NV and P1 contribution in theory. (d) The Hahn echo decay normalized by the NV and P1 contribution shows a remaining contribution from the unknown noise source. The dashed line is a fit with Eq. [5.1.2] assuming the unknown noise source is a layer of two-dimensional spin-1/2 particles. The extracted density is 1.3(5) ppm·nm, with a correlation time of $\tau_c = 1.2 \pm 1.7$ μs. All the data is taken at the same location inside the TEM spot with dosage of 5.4×10^{19} e^-/cm^2 in sample L021.

5.4(a)(b). We did not observe any obvious late-time regime behavior here, suggesting the correlation time of the P1 bath is much longer than 100 μs. The contribution from NV and P1 together can be modeled by:

$$E_{\mathrm{NV+P1}}(t) = R_{\mathrm{intra,nv}}(t) E_{\mathrm{inter,nv}}(t) [E_{\frac{3}{8}}(t)]^2 [E_{\frac{1}{8}}(t)]^2, \tag{5.20}$$

where $R_{\mathrm{intra,nv}}$ is the contribution from intra-group NVs (1/4 of total NV density) with a Ramsey filter function, $E_{\mathrm{inter,nv}}$ is the contribution from inter-group NVs (3/4 of the total NV density) with a Hahn echo filter function, and the rest terms are from P1 centers. This equation is shown in Fig. 5.4(c) and compared to the Hahn echo decay. In our example, these two curves are close to each other, suggesting that the NV's T_2 is mainly limited by a high density of NV and P1 centers. The remaining decoherence source may come from an unknown noise bath. Assuming such bath is two-dimensional spin-1/2 particles, we adopt the model of Eq. [5.1.2] and fit the HE decay after normalizing by the curve from Eq. [5.2.1]. As shown in Fig. 5.4(d), we extracted a density of 1.3(5) ppm·nm for this unknown spin-1/2 bath with a short correlation of $\tau_c = 1.2 \pm 1.7$ μs. This is not surprising given that we did observe g=2 particles and an unknown transition with slightly lower transition frequency than g=2 within the same TEM spot in sample L021, as shown in Fig. 5.1(b). We also applied this analysis method to a few other locations in sample L021, where we have both estimations of P1 and NV densities, and we always observed that the contribution from NV and P1 together cannot fully explain the Hahn echo decay.

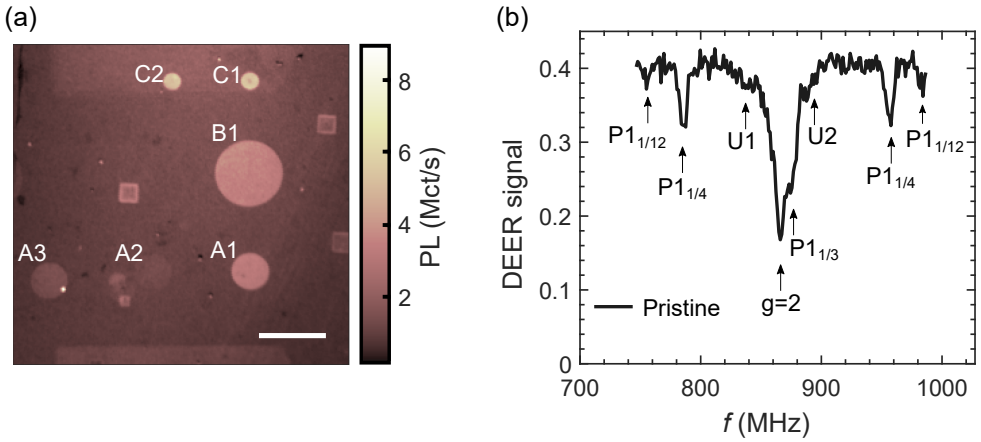

Figure 5.5: Two dimensional spin systems in sample L004, created by ion implantation. (a) The confocal image of the sample L004 around the TEM irradiation spots. The scale bar is 20 μm. (b) The DEER spectrum taken at the center of TEM B1 spot in (a). There are peaks from ^{14}N P1 centers and g=2 spin-1/2 particles. We also observed two peaks near g=2 from unknown particles (U1 and U2). The external magnetic field is aligned to one of the NV axis. Based on the frequencies of the NV ESR peaks, the misaligned angle smaller than 2 degrees and the amplitude is 309.1 G, which is consistent with the location of g=2 peak.

Spot	Dose(/cm^2)	NV density	P1 density	g=2 density	$T_2(\mu s)$	n
Outside	0	5.3 ppm·nm	39.8 ppm·nm	30.2 ppm·nm	4.29	0.80
A2	2.03e18	5.6 ppm·nm	25.9 ppm·nm	33.2 ppm·nm	3.68	0.96
A3	2.03e19	7.8 ppm·nm	33.3 ppm·nm	35.0 ppm·nm	3.89	0.90
B1	1.01e20	9.6 ppm·nm	26.4 ppm·nm	35.3 ppm·nm	3.86	0.92
C1	1.01e21	10.3 ppm·nm	26.2 ppm·nm	27.3 ppm·nm	4.34	0.89

Table 5.2: The properties of shallow two-dimensional spin systems in sample L004, measured outside or at the center of TEM spots. The NV density is estimated by the Rabi PL method. The P1 density is estimated by DEER measurement, driving the $P1_{1/4}$ peak. The g=2 density is also estimated by DEER, thus only contains spins that are coherent on the time scale of a few microseconds. n is the stretch power of the Hahn echo T_2 decay.

5.2.2 Near surface two-dimensional spin systems created by ion implantation in grown diamond

For many quantum sensing applications, the creation of near surface NV ensemble is often needed to bring sensing target close enough to NVs [25, 110, 24]. Here, we also demonstrate the creation of ultra-shallow two-dimensional NV ensembles in sample L004 by ion implantation at low energy into a grown diamond substrate. Sample L004 is grown in a similar way to sample L021 and L026, except there is no delta-doped layer. The sample is implanted with ^{14}N (2.5 keV and 10^{13} cm^{-2} dose) by INNOVion, and it goes through several rounds of high temperature anneal at 850°C and 1200°C. TEM irradiation is used to further augment the NV density. The photoluminascence (PL) image of the diamond sample after TEM irradiation is shown in Fig. 5.5(a), and the three square-shape hillock features can be used for co-locating the AFM measurement and confocal NV measurement. These hillock features are square-shape growth defect which are usually over 100 nm tall and have a higher density of nitrogen incorporated along the edges [163]. Outside the hillock, the majority of nitrogen should come from the ion implantation. The depth distribution of NVs can be approximated by a normal distribution of 4.5 ± 2.0 nm, based on the stopping and range of ions in matter (SRIM) simulation with our implantation parameters.

A DEER spectrum is measured at the center of the TEM spot B1 as shown in Fig. 5.5(b). The spectrum clearly shows the existence of ^{14}N P1 centers and g=2 spins, which is likely to be related to surface spins [24]. Close to the $P1_{1/3}$ and the g=2 peaks, we also observed two unknown transition peaks, U1 and U2, at -32.4(9) MHz and +51.46(7) MHz relative to g=2 peak. We also notice that the Rabi oscillation of these two transitions has a smaller frequency, specifically $\omega_{\mathrm{U1}}/\omega_{\mathrm{g=2}} \approx 0.42$.

Then, we also perform the analysis of the NV and P1 densities, as well as their

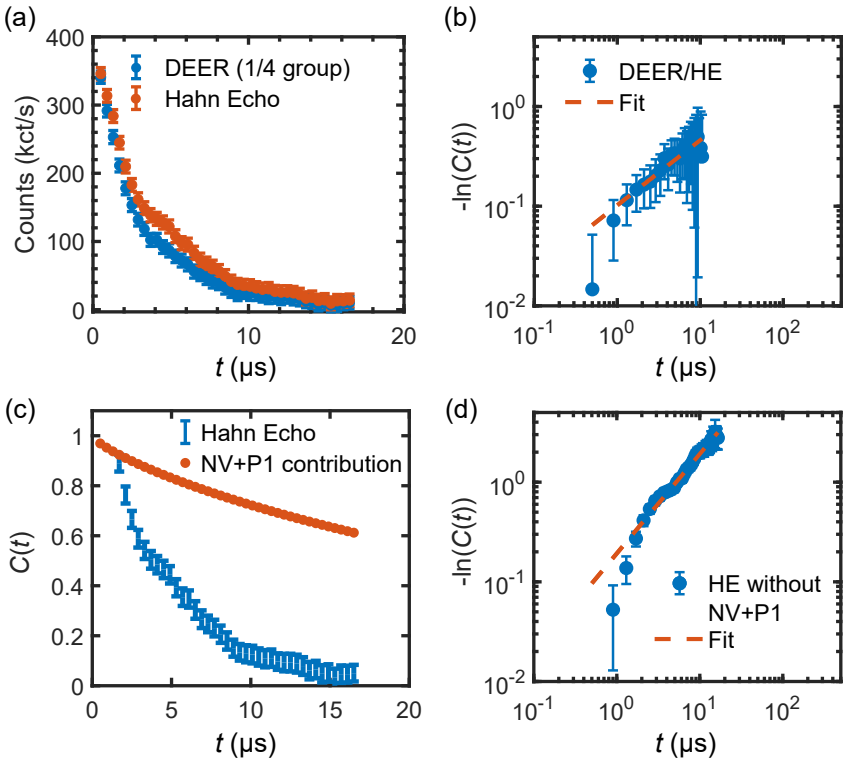

Figure 5.6: The analysis of NV and ^{14}N P1 contribution to Hahn echo decay for sample L004, in which the ^{14}N are introduced by ion implantation. (a) The Hahn echo and DEER measurement. The DEER measurement is using the sequence shown in Fig.5.1(a), driving a $P1_{1/4}$ transition. (b) The DEER signal normalized by the Hahn echo signal. The dashed line is a fit that shows a stretch power of 2/3, assuming a two-dimensional P1 and NV layer, for the early-time regime. The density of $P1_{1/4}$ extracted is 6.61 ± 0.25 ppm·nm, thus corresponds to a total P1 density of 26.4 ± 1.0 ppm·nm. (c) The Hahn echo decay compared to the NV and P1 contribution in theory. (d) The Hahn echo decay normalized by the NV and P1 contribution shows a remaining contribution from unknown noise source. The dashed line is a fit assuming the unknown noise source is a layer of two-dimensional spin-1/2 particles. The extracted density is 365(7) ppm·nm, with a correlation time of $\tau_c > 3$ ms. All the data is taken at the same location inside the TEM spot with dosage of 1.01×10^{20} e$^-$/cm^2 in sample L004. There seems to be a dimensional crossover around $t = 3$ μs caused by the finite thickness of the NV layer.

contribution to the Hahn echo decay as shown in Fig. 5.6. By comparing to the sample L021 and sample L026, we found this shallow NV ensemble created by ion implantation has a much shorter T_2. The DEER signal normalized by Hahn echo still shows a stretch power of 2/3, indicating the thickness of the NV and P1 layer is small. There seems to be a dimensional crossover around $t = 0.5$ μs, before which the stretch power is larger than 2/3. Such crossover corresponds to a thickness of around 5 nm. For TEM B1 spot, which has a dosage of 1.01×10^{20} e^-/cm^2, the P1 density is 26.4 ± 1.0 ppm·nm and NV total density is 9.6 ppm·nm. If adopting the aforementioned model, the remaining decoherence in Hahn echo decay comes from a quasi two-dimensional spin-1/2 bath with a density of 365(7) ppm·nm. Note this estimation should also contain the contribution from g=2 spins and U1 U2 spins that are visible in the DEER spectrum. The dimensional crossover happens at a later time around $t = 2$ μs, thus corresponding to a larger thickness for this unknown noise source. A summary of the NV and P1 densities is shown in table 5.2. The NV densities are all estimated by using the Rabi PL method.

Chapter 6

Sensing molecular spin arrays programmably patterned by DNA origami

Utilizing solid-state spin qubits in proximity to material surfaces for quantum sensing offers a viable route for various potential uses, such as nanoscale Nuclear Magnetic Resonance (NMR) and Electron Paramagnetic Resonance (EPR) spectroscopy that are capable of analyzing small groups or individual molecules [164, 165, 166, 110, 167, 25]. Diamond defects, especially negatively charged nitrogen-vacancy centers (NVs), have garnered significant attention for their remarkable features, including the photo-stability, distinct spin properties at room temperature with optical polarization and readout, and biocompatibility [35]. One central challenge of the field is to position the sensing targets near the material surfaces, ensuring precise control over their density, selectivity,

The content of this chapter will substantially appear in the paper we are preparing for publication: Zhiran Zhang, Taylor Morrison, Lillian Hughes, Weijie Wu, Ruiyao Liu, Dolev Bluvstein, Norman Y. Yao, Deborah Fygenson, and Ania C. Bleszynski Jayich, Diamond defect-based sensing of programmably patterned molecular spin arrays with single-spin sensitivity, in preparation (2024).

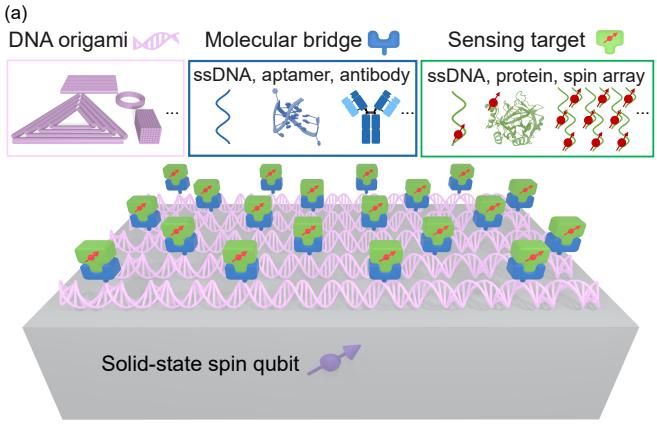

Figure 6.1: A novel sensing approach that combines solid-state spin qubits with DNA origami as a framework for arranging molecular structures. This method utilizes DNA origami to create a programmable pattern of molecular bridge, such as ssDNA, aptamers, and antibodies, that act as specific binding sites. These binding sites are designed to selectively attach to a range of sensing targets, including ssDNA, proteins, and spin arrays. The solid-state spin qubits are then employed to detect these bound molecules. This experimental setup is versatile, allowing for its application in both wet and dry environments. The structures of the aptamer and human α-thrombin protein shown here are from the RCSB protein data bank (RCSB.org) of ID 6EO6 [169].

and binding chemistry, all the while preserving the sensor's characteristics and reducing noise generated at the interface [25, 24]. Conventional approaches to surface functionalization often involve the direct covalent bonding of target molecules to the diamond surface. Nevertheless, both covalent and non-covalent functionalization techniques face challenges in controlling the density and placement of molecules when using these methods [25]. Additionally, these approaches can negatively affect the charge stability and spin coherence of near-surface NV centers [24, 168].

In our work, we introduce and validate a novel sensing approach that employs DNA origami to intricately arrange target molecules and anchor them onto the diamond surface through electrostatic force, as illustrated in Figure 6.1. Our findings reveal that the influence of DNA origami on the properties of shallow NV centers is negligible. Subsequently, we successfully detected Gd^{3+} chelate spins, which were programmably patterned on

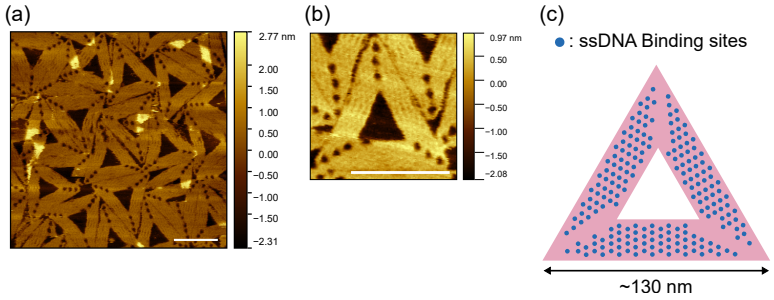

Figure 6.2: The triangular DNA origami structure. (a) The wet AFM image of the DNA origami on a mica synthesized in our lab. Imaging was performed in Tapping Mode under 12.5 mM Tris/Mg^{2+} buffer on a Digital Instruments Nanoscope III Multimode AFM (Veeco), using Bruker SNL-B AFM probe. $NiCl_2$ was also added to the buffer improve binding to mica surface. The binding sites on origami have not hybridized to ssDNA. (b) The zoom-in wet AFM image. (c) The locations of 204 possible binding sites on one side of the DNA origami.

the origami, using NV T1 relaxometry. The density of Gd^{3+} on the diamond surface is demonstrated to be well controlled. This innovative approach, which allows for the precise placement of various molecules on the diamond surface with predetermined densities, could facilitate the selective detection of small ensembles of target molecules with high consistency in our experiments. Our experiments were conducted in dry conditions; however, in theory, this sensing method is equally applicable in liquid environments.

Additionally, the strongly interacting spin network created using DNA origami could act as nearby auxiliary spins to facilitate quantum-enhanced sensing. It also opens up opportunities to explore many-body dynamics in these spin networks. In our simulations, significant spin squeezing was noted when multiple binding sites on a triangular origami structure hosted coherent spins on the time scale of ten microseconds.

6.1 Synthesis of molecular-spin-labeled DNA origami

DNA origami are programmable bottom-up self-assembly of DNA molecules, typically consisting of a long scaffold single-stranded DNA (ssDNA) and numerous short staples

ssDNAs [170]. These short staples are crafted to match different parts of the scaffold DNA and can include additional "tails" that serve as attachment points for target molecules, like spin-labeled ssDNA [171]. In our study, we utilized a triangular origami structure where all the binding sites are positioned on one side of the triangle, as depicted in Fig. 6.1 and Fig. 6.2(c) [172]. On 1/3 of the triangle, there are 8 rows of dsDNA, which are connected by staples crossing two rows. Along each row, there are 3 turns of DNA between two adjacent binding sites, as shown in Fig. 6.1 and Fig. 6.5(a). The spacing between rows is around 6-10 nm when the crossover is every 1.5 turns for our design, which is not equal to when DNA are closely packed, probably affected by the electrostatic repulsion between two negatively charged DNA [170]. As a result, the smallest distance between any two binding sites is around 6 nm. This design allows for up to 204 binding sites, arranged with C3 symmetry, and gives us the ability to selectively activate or deactivate each site. Another reason why we choose triangular origami is because such a shape is easy to identify under AFM, rigid against distortion, and has a low tendency to aggregate [173]. The details of the design can be found in the original paper [172]. To minimize the likelihood of two origami structures hybridizing through the complementary ssDNA present in the tails of the binding sites, we incorporated a 29-base sequence (AATGCTGATGCAATGTGCGCAAATAAAAA) at the 5' end of each staple strand sequence, rather than the more commonly used poly-T sequences.

The triangle origami with binding sites are synthesized using the following procedure, which is standard in the origami community [172]. Staple strands (Integrated DNA Technologies, 150 or 200 μM each in water) and the scaffold strand (single-stranded M13mp18, Bayou Biolabs, P-107) were mixed together to target concentrations of 100 nM (each staple) and 40 nM, respectively (2.5:1 staple:scaffold ratio) in 10 mM Tris Base with 12.5 mM magnesium chloride (adjusted to pH 8.35-8.40 with HCl). (We refer to the buffer used for origami synthesis, with the above combination of Tris Base, and $MgCl_2$,

as "Tris/Mg^{2+}".) 50 μL volumes of staple/scaffold mixture were heated to 90°C for 5min and annealed from 90°C to 20°C at -0.2°C/min in a PCR machine. We used 0.5 mL DNA LoBind tubes (Eppendorf) to minimize loss of origami to the sides of the tubes. Then the excess staples were purified away using 100 kD molecular weight cut-off spin filters (Amicon Ultra-0.5 mL). By the following protocol, recovery is generally 35%–50% and staples are not visible by agarose gel. Wet the filter by adding 500 μL Tris/Mg^{2+}. Spin filter at 2,000 r.c.f. (relative centrifugal force) for 8.5 min at room temperature until the volume in the filter is around 50 μL. Discard the filtrate. Add 50 μL of unpurified origami and 400 μL Tris/Mg^{2+}. Spin at 2,000 r.c.f. for 8.5 min. Wash the origami two more times by discarding the filtrate, adding Tris/Mg^{2+}, and spinning at 2,000 r.c.f. for 8.5 min. Invert the filter onto a clean tube and spin at 2,000 r.c.f. for 8.5 min to collect purified origami. Throughout the process, the origami were quantified using a NanoDrop 2000 spectrophotometer (Thermo Scientific). The synthesized DNA origami can be imaged and verified under wet AFM as demonstrated in Fig. 6.2(a)(b).

The binding sites can then hybridize to ssDNA labeled by different kinds of molecules. In our recent work, we demonstrate Gd-labeled origami and use NV T_1 relaxometry to detect Gd^{3+}. As an example, the Gd-labeled ssDNA are synthesized using the following protocol. If using another kind of target molecules, it should have an azide group to conjugate to the alkyne group on the ssDNA.

The ssDNA complementary to binding sites with 0-4 modified thymine bases closest to the 5' end (Octadiynyl dU) depending on our design are ordered from Integrated DNA Technologies and suspended in Milli-Q water at a target concentration of 0.5 mM. Gd-Azido-mono-amide-DOTA (we will refer to it as Gd- DOTA) is purchased from Macrocyclics, Inc., and is suspended in Milli-Q water targeting at 100 mM. (Gd-DOTA now refers to Gadolinium(III) 1,4,7,10-Tetraazacyclododecane-1,4,7,10-tetraacetate.) The click reagent, BTTAA:$CuSO_4$ 1:1 solution, is prepared by dissolving

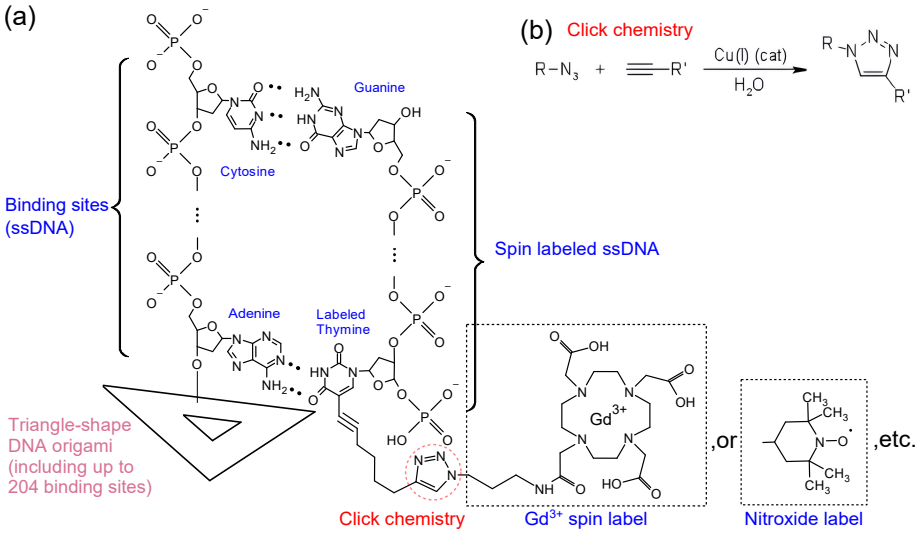

Figure 6.3: (a) The structure of the spin labeled DNA origami. The chemical formula only shows one binding sites and complementary spin-labeled ssDNA. The conjugation by click chemistry happens where the red dashed line circle marks. In our work, Gd-DOTA (tetraxetan chelate) spin label and nitroxide (TEMPO) spin label are used. (b) The general reaction formula for click chemistry using Cu(I) catalyst in aqueous solution.

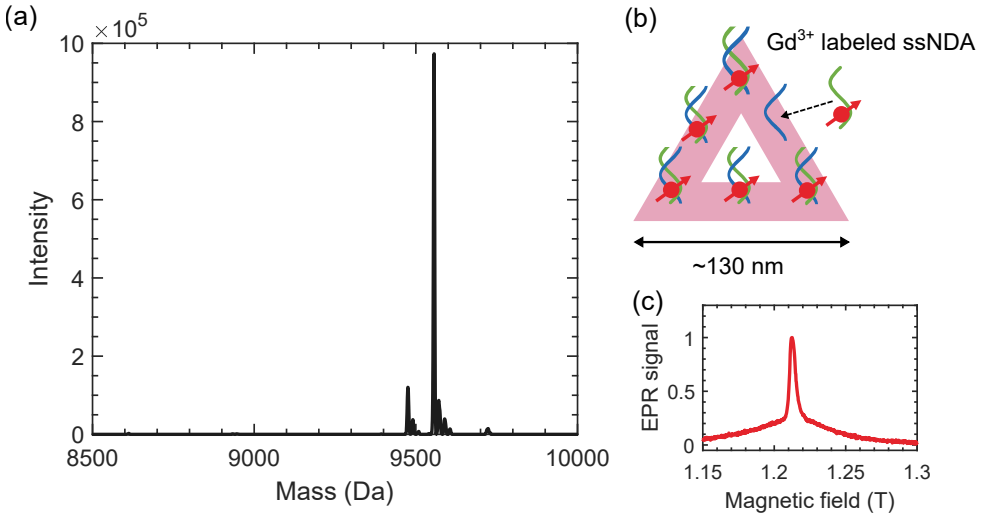

Figure 6.4: Verifying the synthesis of Gd^{3+} labeled DNA origami. (a) The Liquid Chromatography Mass Spectrometry (LC-MS) of Gd-DOTA labeled ssDNA. The Gd-DOTA-ssDNA, conjugated via click chemistry, is expected at 9555.2 Da, while the unlabeled ssDNA is expected at 8913.9 Da. (b) The schematic of the hybridization between Gd-DOTA-ssDNA and origami. (c) The Q-band (33.81 GHz) cw-EPR signal of the Gd-labeled origami in solution after hybridization. The measured g-factor of 1.9923(3) is distinct from common g=2 spins.

BTTAA (purchased from Bioconjugate Technologies, LLC.) and $CuCl_2 \cdot 2H_2O$ (Sigma-Aldrich) in Milli-Q water, targeting at 10 mM.

The click chemistry between ssDNA and Gd-DOTA is performed as follows.

1. First, 200 μL 0.5 mM ssDNA with a number of M modified thymine bases (ratio=1) is mixed with $5\times M$ μL 100 mM Gd-DOTA (ratio=$5\times M$, which is 5× excess) in a 500 mL LoBind tube (Eppendorf).

2. Add 5 μL 10 mM BTTAA:$CuSO_4$=1:1 in Milli-Q water (ratio=4), and 20μL 100 mM fresh Sodium Ascorbate (MilliporeSigma) in Milli-Q water (ratio=20) into the tube.

3. Use a clean syringe to inject N_2 into the solution and atmosphere in the tube to purge O2 away for 5 min in the LoBind tube. The solution should be transparent or a little yellow instead of blue or green. No precipitation should happen in this procedure.

4. Then, incubate the solution for at least 10 hours at room temperature.

5. Lastly, the Gd-labeled ss-DNA is purified into Tris/Mg^{2+} buffer by a 3 kD molecular weight cut-off spin filter (Amicon Ultra-0.5 mL), using the same centrifuging protocol described above but with 14,000 r.c.f. for 15 min each round.

6. The purified Gd-labeled ssDNA are then verified by Liquid Chromatography Mass Spectroscopy (LC-MS) to check molecular weights (Novatia LLC., 20-min LC-MS).

For instance, Fig. 6.4(a) presents the LC-MS of the ssDNA, which has a single Octadiynyl dU base, tagged with Gd-DOTA. The observed spectrum shows a predominant peak at 9556.2(1) Da, aligning with the expected mass of the Gd-DOTA labeled ssDNA, with a minor mass error of 1.0 Da. The spectrum does not show any peak around 8913.9 Da which corresponds to unlabeled ssDNA, therefore indicating the yield rate of the click chemistry is close to 100%. The origami and Gd-labeled ssDNA (ratio=1.5) are hybridized at room temperature for at least 12 hours. Then, the Gd-labeled origami are purified by 100 kDa molecular weight cut-off spin filters (Amicon Ultra-0.5 mL) again using the same procedure described above. The Q-band continuous-wave electron para-

magnetic resonance (EPR) measurement (Bruker EMXplus) can be performed to verify the existence of Gd^{3+} in the origami solution as shown in Fig. 6.4(c) [174, 175, 176]. EPR measurement can also be used to verify other possible spin labels, including the nitroxide.

6.2 Impact of DNA origami on shallow NV centers

The NV-origami platform shows promise for arranging coherent spins into arrays, which allows for exploration of many-body physics within these spin systems. As the first step, we examined how the presence of DNA origami deposited on the surface affects the characteristics of nearby shallow NV centers.

After the synthesis of spin-labeled origami, it can then be deposited onto the diamond surface. The deposition coverage of the origami can be roughly tuned by varying the concentration of origami used here. First, position the diamond at the center of a clean wafer carrier tray with NV side up. Pippette 2 μL of 150 mM Tris/Mg^{2+} pH=8.90 buffer to the diamond surface. Then add 2 μL of origami. To achieve a high fraction of surface coverage, the concentration of origami should be at least 1 nM. After gently pipetting up and down for 1 minute. Incubate at room temperature for 15 min. Then immerse the diamond, while the solution is still on the surface, into 150 mM Tris/Mg^{2+} pH=8.90 buffer for 5 seconds, then into 75% IPA in Milli-Q water (v/v%) for 5 seconds, and finally into 100% IPA for 1 min. Lastly, put the diamond on a cleanroom wipe and let it dry in the air.

In our study, we evaluated five different areas within a TEM spot, which had been exposed to a dosage of 1.01×10^{20} e^-/cm^2 as mentioned before (see table 5.2), to assess changes in NV center coherence times and DEER signals before and after the deposition of unlabeled origami. As shown in Figure 6.5(d), the presence of origami on the surface

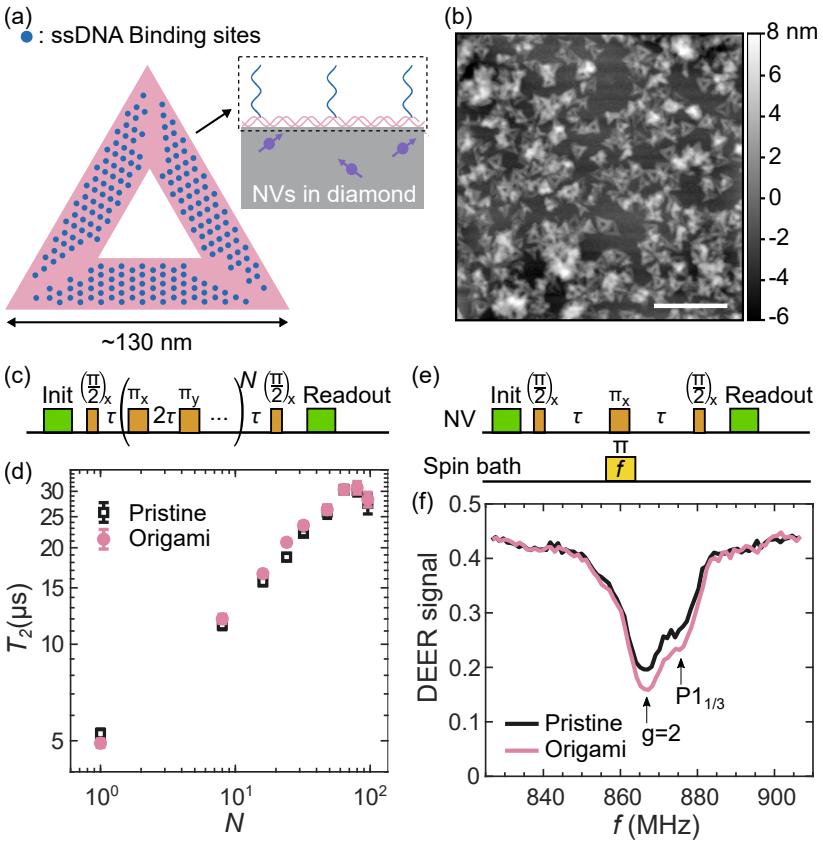

Figure 6.5: The DNA origami structures were found to have minimal impact on the shallow NV centers from sample L004. (a) The experiment setup involves a triangular DNA origami deposited on the diamond surface in proximity to shallow NV centers. The origami has not hybridized with any spin-labeled ssDNA. (b) The dry AFM image showcases the diamond surface after the deposition and drying of DNA origami. (c) The Hahn echo and XY8 pulse sequence used to measure the coherence time T_2 of NV centers. $N = 1$ corresponds to Hahn echo sequence, and $N = 8k, k = 1, 2, 3, ...$ corresponds to XY8 sequences. (d) The coherence time with origami deposited on the surface compared to that with a pristine diamond surface. The XY8 results are taken from a single confocal spot as a representative example, whereas the Hahn echo data is averaged from various spots across the diamond. (e) The DEER pulse sequence. The DEER spectrum is measured when τ is fixed, and the frequency of the microwave pulse on the spin bath (f) is varied. (f) The DEER spectra from both a pristine surface and an origami-covered surface are compared. The signals feature two peaks attributed to g=2 spin-1/2 particles and 1/3 of the transitions from nearby P1 centers. This data is averaged from various locations across the diamond.

did not lead to a notable decrease in the Hahn echo coherence time (T_2 with $N = 1$). The decay of the Hahn echo exhibited a stretch power close to 1, indicating that the Hahn echo T_2 is predominantly limited by a three-dimensional noise bath over a timescale of a few microseconds. Furthermore, the coherence time for the XY8 pulse sequence, where $N = 8k$ ($k = 1, 2, 3, ...$), remained consistent with that observed on a pristine surface. A power law fit of $T_2(k) = T_2(1) \cdot (k)^{\lambda}$ before the saturation, where k is the number of cycles of XY8 pulses, shows a decoupling coefficient of $\lambda = 0.46(2)$. This value is less than expected $\lambda = 2/3$ for a noise environment dominated solely by slowly fluctuating substitutional nitrogen (P1 centers), thereby suggesting the presence of another rapidly fluctuating noise bath arising from other spin defects such as surface spins [177, 104, 106].

Furthermore, the DEER measurement revealed peaks corresponding to the transition frequencies of P1 centers as well as peak at g=2, as shown in Fig. 6.5(f). There was only a slight increase in the peak amplitude associated with coherent g=2 spins. The deposition of origami on the surface did not introduce any new peaks compared to a pristine surface. In our experiments, when DNA origami are deposited on diamond, we consistently found no significant change in several key properties of shallow NV centers. These aspects include (1) the PL value and spatial variation of PL under an identical initialization condition, (2) the contrast of Rabi oscillation, and (3) the charge state stability. These results collectively suggest that the DNA origami platform is capable of supporting arrays of coherent spins without significantly impacting the performance or properties of adjacent shallow NV centers, highlighting its potential for advanced quantum sensing and investigation of many-body spin dynamics. Future experiments could focus on measuring single NV centers to more closely investigate how the noise environment, as detected by dynamical decoupling sequences, is influenced by the presence of DNA origami.

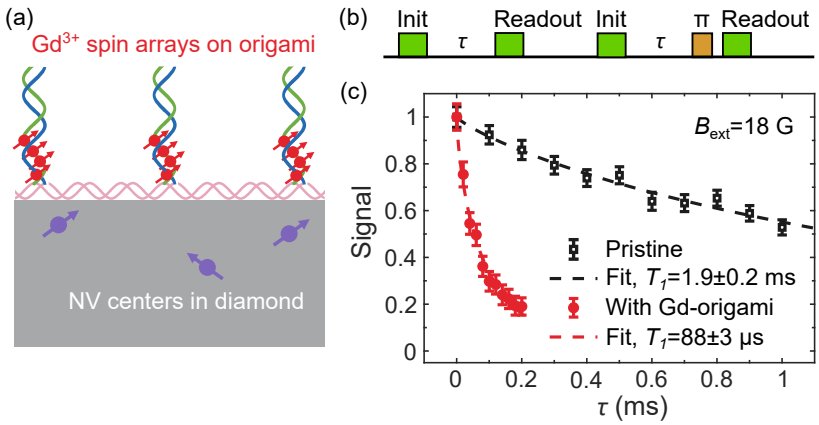

Figure 6.6: The T_1 relaxometry using shallow NV ensemble to detect Gd^{3+} spin arrays patterned by origami. (a) The schematic of the experiment. (b) The pulse sequence of differential T_1 relaxometry. The two readouts are PL and PL_{swap} respectively. (c) T_1 reduction caused by Gd-labeled origami on diamond surface. The differential signal is the normalized $PL - PL_{swap}$. The two sets of data are taken at the same location on the diamond sample L004.

6.3 Detection of Gd^{3+} arrays patterned on origami by shallow NV ensemble

To demonstrate the ability of origami to pattern spinful molecules on the diamond surface, we now turn to the detection of the origami patterned Gd3+ spins via T_1 relaxometry using ensemble NVs.

The experiment demonstrating the detection of Gd3+ by NV relaxometry is shown in Fig. 6.6. In our T_1 relaxometry experiments, we aligned the external magnetic field to one of the four possible NV axes, and the amplitude of the field is small enough so that the difference between the relaxation rates of $|m_s = 0\rangle \leftrightarrow |m_s = -1\rangle$ and $|m_s = 0\rangle \leftrightarrow |m_s = +1\rangle$ transitions is negligible. Thus we have $\Omega_+ \approx \Omega_- = \Omega$. See Fig. 6.7(a) for the energy diagram with relaxation rates. We perform differential T_1 relaxometry as shown in Fig. 6.6(b). The NV ensemble is initialized and readout by a 532-nm laser. The microwave π pulse drives the $|m_s = 0\rangle \leftrightarrow |m_s = -1\rangle$ transition of the NVs which are

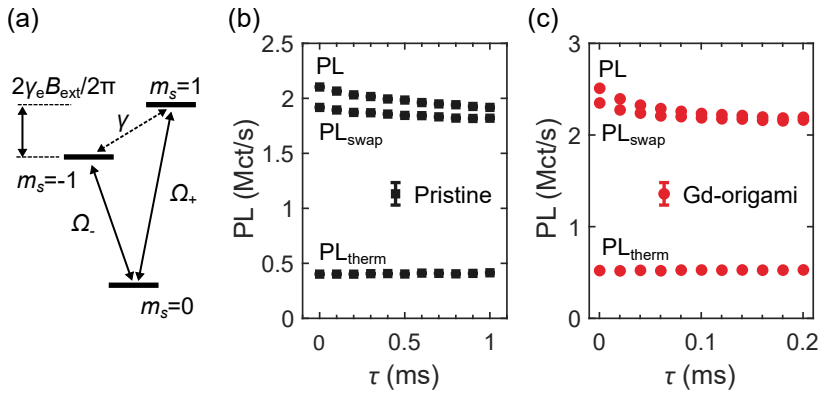

Figure 6.7: The details of differential T_1 relaxometry. (a) The energy diagram and transition rates of NV ground state manifold. (b) The relaxometry signal (PL and PL_{swap}) with a pristine surface for sample L004. The PL_{therm} is calculated by Eq. (6.3), and does not show a significant increase or decrease, indicating no unbalanced charge state recombination or ionization. (c) The relaxometry signal with Gd-labeled origami deposited on the diamond surface. The origami is designed to have 204 binding sites to hybridize to Gd-ssDNA, where each ssDNA conjugated to four Gd-DOTA. The PL_{therm} also indicates no unbalanced charge state recombination or ionization.

aligned to the external field. The sequence consists two readout per cycle, PL and PL_{swap}, to be averaged over shots and calculated for the final signal defined as the normalized $PL - PL_{swap}$. We observed both PL and PL_{swap} decrease with the dark time τ, shown in Fig. 6.7(b)(c), which is in contrast to T_1 measurement of single NV centers in the absence of charge decay. With the following phenomenological model, we argue that this behaviour is consistent with there being no significant charge state ionization or recombination.

When a strong external B field is applied along with the NV axis, the transition rates cannot be assumed to be the same: $\Omega_+ \neq \Omega_- \neq \gamma$. Additionally, the charge state ionization process, which may be relevant on the timescale of the pulse sequence, can cause the total NV^- population to have a dark time dependence ($\rho^-(\tau)$). Under these conditions, the spin relaxation process of the NV center can be captured by the following

set of differential equations:

$$\frac{d}{d\tau}\left[\frac{1}{\rho^{-}(\tau)}\begin{pmatrix}\rho_0(t)\\ \rho_{-1}(\tau)\end{pmatrix}\right]=\frac{1}{\rho^{-}(\tau)}\begin{pmatrix}-\Omega_{-}-2\Omega_{+} & -\Omega_{+}+\Omega_{-}\\ \Omega_{-}-\gamma & -\Omega_{-}-2\gamma\end{pmatrix}\begin{pmatrix}\rho_0(\tau)\\ \rho_{-1}(\tau)\end{pmatrix}+\begin{pmatrix}\Omega_{+}\\ \gamma\end{pmatrix}, \tag{6.1}$$

where $\rho_{-1}(\tau)$ and $\rho_0(\tau)$ are the population of $|m_s=-1\rangle$ and $|m_s=0\rangle$ states respectively. The solution to the rate equations is rather complicated and not single-exponential. In order to accurately determine all three transition rates, several pulse sequences for both single-quantum and double-quantum spin relaxation need to be employed [94]. Therefore, to circumvent this problem, in our work, we apply a small external field so that approximately we have $\Omega_{+}=\Omega_{-}=\Omega$. Moreover, when we initialize the NVs with the 532-nm green laser, we assume the $\rho_{+1}(0)=\rho_{-1}(0)=\rho^{-}(0)\eta$, where η is due to imperfect polarization of the NV after initialization pulse. A nonzero η will not affect our simple interpretation of the relaxation signal we observed, so it is omitted in the following discussion. Lastly, in the relaxation pulse sequence used in this work, the two PL signals, where the first signal is a direct readout and the second signal has a resonant microwave pulse to swap the ρ_{-1} and ρ_0 right before the readout, can be written as [1]:

$$\begin{aligned}\mathrm{PL}(\tau)=&\mathrm{PL}_0^{-}\rho_0(\tau)+\mathrm{PL}_{\pm1}^{-}\rho_{-1}(\tau)\\ &+\mathrm{PL}_{\pm1}^{-}\rho_{+1}(\tau)+\mathrm{PL}^{0}(1-\rho^{-}(\tau)),\end{aligned} \tag{6.2}$$

$$\begin{aligned}\mathrm{PL}_{\mathrm{swap}}(\tau)=&\mathrm{PL}_0^{-}\rho_{-1}(\tau)+\mathrm{PL}_{\pm1}^{-}\rho_0(\tau))\\ &+\mathrm{PL}_{\pm1}^{-}\rho_{+1}(\tau)+\mathrm{PL}^{0}(1-\rho^{-}(\tau)),\end{aligned} \tag{6.3}$$

PL_0^{-}, $\mathrm{PL}_{\pm1}^{-}$ are the PL of different NV^{-} spin states, and PL^{0} is the PL of NV^{0}. Finally,

we calculate the difference signal:

$$\begin{aligned} \mathrm{PL}_{\mathrm{diff}}(\tau) =& \mathrm{PL}(\tau) - \mathrm{PL}_{\mathrm{swap}}(\tau) \\ &= (\mathrm{PL}_0^- - \mathrm{PL}_{\pm 1}^-)(\rho_0(\tau) - \rho_{-1}(\tau)). \end{aligned} \tag{6.4}$$

Under the aforementioned assumptions, this differential signal can be written in a simple form:

$$\mathrm{PL}_{\mathrm{diff}}(\tau) = (\mathrm{PL}_0^- - \mathrm{PL}_{\pm 1}^-)e^{-3\Omega\tau}\rho^-(\tau). \tag{6.5}$$

This implies that the measured differential signal could have a stretched parameter $n \neq 1$ if the charge ionization in the dark is present on the relevant time scale. Furthermore, a variation of T_1 across individual NVs can cause the relaxation signal for the NV ensemble to have a stretched parameter $n \neq 1$. In this work, we fit our signals by the single exponential decay with a stretched parameter:

$$\mathrm{PL}_{\mathrm{diff}}(\tau) = (\mathrm{PL}_0^- - \mathrm{PL}_{\pm 1}^-)e^{-(\tau/T_1)^n}. \tag{6.6}$$

The fitted T_1 should be interpreted as a weighted averaged relaxation time for the NV ensemble. It still can be used to reflect the relaxation signal, but we need to perform a numerical simulation to model its dependence on the density of Gd^{3+}, for example.

For NV ensembles, $\rho^-(\tau)$ cannot be directly probed by the usual photon distribution analysis [74]. To figure out whether strong charge ionization or recombination is present, we analyze the PL level of the thermal mixture of the NV spin state. Assuming all four axes NVs have the same PL, the PL of the thermal mixture could be extracted from the differential T_1 measurement:

$$\mathrm{PL}_{\mathrm{therm}}(\tau) = -\frac{5}{12}\mathrm{PL}(\tau) + \frac{2}{3}\mathrm{PL}_{\mathrm{swap}}(\tau). \tag{6.7}$$

An example of the thermal mixture PL for a pristine surface and a surface with Gd-DOTA labeled origami is shown in Fig. 6.7(b)(c). The $\mathrm{PL}_{\mathrm{therm}}(\tau)$ for both pristine surface data and Gd-origami data are around 0.5 Mct/s, and do not show any reduction over 1 ms, which indicates that the population of NV^0 does not increase.

When fitting the differential signal by $\exp[-(\tau/T_1)^n]$, with a pristine diamond surface we measured $T_1 = 1.9(2)$ ms, and $n = 0.83(7)$, shown in Fig. 6.6(c). We attribute the stretched parameter of $n < 1$ to the averaging effect of the ensemble signal, which consists of decays at various rates [141]. After the surface is covered with Gd-labeled origami, the T_1 measured at the same location drops to 88(3) μs. Furthermore, to rule out the possibility of charge state being the primary reason for T_1 reduction, we checked that $\mathrm{PL}_{\mathrm{therm}}$ does not decay to a smaller value when varying τ in the presence of Gd^{3+}.

In Fig. 6.8, we present the dependence of T_1 of NV ensemble on the estimated density of Gd^{3+}. The data is from all the successful deposition attempts with various Gd-origami configurations (enabling different numbers of binding sites and Gd^{3+} per sits) and fractions of surface coverage. The two-dimensional densities of Gd^{3+} spins are estimated using the following equation:

$$\sigma_{\mathrm{Gd}} = \frac{N_{\mathrm{b}} \cdot M \cdot C_{\mathrm{s}}}{A}, \tag{6.8}$$

where N_{b} is the number of binding sites on the DNA origami and can range from 0 to 204; M is the number of Gd-DOTA per target ssDNA ($M = 0, 1, 2, 3,$ or 4 in our experiment); C_{s} represents the fractional surface coverage ($C_{\mathrm{s}} = 100\%$ represents a perfect monolayer of origami deposited), and A is the area of a triangular origami when it is not distorted or folded. In each round of experiment after Gd-origami deposition, we recorded T_1 over at minimum of 8 locations, including outside and inside the TEM irradiation spot, and calculated the averaged T_1. Remarkably, we observed a strong correlation between

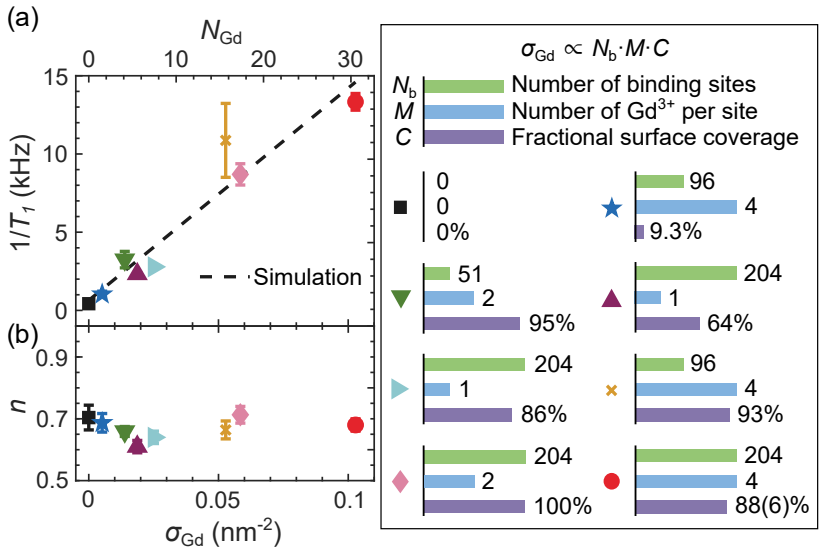

Figure 6.8: T_1 relaxometry detection of Gd^{3+} programmably patterned on DNA origami with a controllable density. (a) The T_1 relaxometry conducted in eight rounds of experiments with different DNA origami designs. The NV relaxation rates, $1/T_1$, show a strong positive correlation with the estimated densities of Gd (σ_{Gd}). We vary the number of binding sites, the number of Gd^{3+} per site, and the fraction coverage of the diamond surface. The data is averaged from the same set of multiple locations on the diamond. All data shown here is not post-selected. The dashed line represents the numerical simulation, from which we extracted the correlation time of the Gd^{3+} to be $\tau_c = 0.18(3)$ ns. The stretch power of the T_1 decay does not show any significant correlation with ρ_{Gd}. (b) The averaged stretch power of T_1 decay in each experiment.

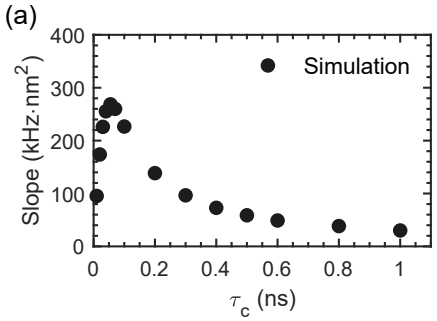

Figure 6.9: The dependence of the slope, $d(1/T_1)/d(\sigma_{\mathrm{Gd}})$, on the correlation time τ_c from numerical simulation. We approximate the depths of NVs by a normal distribution of 4.5 ± 2.0 nm based on SRIM simulation, with a cutoff at 0.2 nm. The simulation is based on Eq. (6.9) with $\omega_0 = 2\pi \times 2.87$ GHz, and $S = 7/2$ for Gd^{3+} spins.

averaged $1/T_1$ and σ_{Gd} with a sample Pearson correlation coefficient of $r_P = 0.958$. As for the stretch power, it did not show a significant correlation with the Gd^{3+} density (with $r_P = 0.169$). The stretch power also did not fluctuate by more than 0.1 over all rounds of our experiments. This might be because the distribution function of the T_1 in a certain confocal spot did not dramatically change with different Gd-origami deposition, except for having lower mean values in the presence of Gd^{3+}. Furthermore, our numerical simulation reveals a linear relationship between $1/T_1$ and σ_{Gd}.

For a single NV as the qubit sensor at low field, the reduction of T_1 induced by a Lorentzian noise bath (equivalent to correlation function being a single-exponential decay) from a single Gd^{3+} can be modeled by the following equation, which is similar to Fermi's golden rule [44, 45, 46]:

$$\frac{1}{T_1} = 3\Omega' + \left(\frac{\mu_0 \hbar \gamma_{\mathrm{nv}} \gamma_{\mathrm{Gd}}}{4\pi r^3}\right)^2 \frac{(S^2+S)(2+3\sin^2\alpha)\tau_{\mathrm{c}}}{1+\omega_0^2\tau_{\mathrm{c}}^2}, \tag{6.9}$$

where Ω' denotes the original transition rate between NV ground states $|0\rangle$ and $|\pm 1\rangle$ with a pristine diamond surface, $S = 7/2$ is the spin number of Gd^{3+}, α is the angle between the external field and the vector joining NV and Gd^{3+} locations, μ_0 is the

vacuum permeability, γ_{nv} and γ_{Gd} are the gyromagnetic ratios of NV and Gd^{3+}, r is the distance between NV and Gd^{3+}, and $\omega_0 \approx 2.87$ GHz is the transition frequency of NV. Finally, we extracted the correlation time of Gd^{3+}, $\tau_c = 0.18(3)$ ns, assuming a depths contribution based on the stopping and range of ions in matter (SRIM) simulation with our implantation parameters. The slope coefficient of the linear dependence between $1/T_1$ and density is only a function of τ_c when we keep all other conditions fixed. Thus, we can estimate τ_c from the measured slope, as shown in Fig. 6.9. Our estimation of Gd^{3+} correlation time is consistent with the Monte Carlo simulation beyond the Redfield limit at low field and room temperature [178]. In our experiment, we maintained the external magnetic field at a consistent value, 18.4(5) G. Therefore, the change of field-dependent correlation time of Gd^{3+} and NV relaxation behavior should be negligible between different rounds of experiments.

6.4 Potential future applications

We first discussed the possible different experiment setups to be used in future research. In our work, we have used 150-μW, 4-μs 532 nm green laser pulses for the initialization, forming a Gaussian beam spot with a 500-nm FWHM. In practice, a widefield setup with a higher power and longer duration laser pulse could be used to initialize NVs within a larger beam spot. If we assume one uses 10-mW, 4-μs 532 nm green laser pulses for initialization of a Gaussian beam spot with a 4.1-μm FWHM, the number of NVs measured is about 65.7× more compared to the confocal setup in this work. Therefore, the time to achieve the same measurement results would only require 1/66.7 of the time if we also assume all other experiment conditions are the same, including the collection efficiency and overhead time in the pulse sequence. For real applications, the PL may be subject to laser power drift over the course of time, which is much longer than one

shot of pulse sequence but shorter than the total measurement time. Furthermore, one could perform all-optical measurements instead to eliminate the need for the microwave components and make the experiment setup more compact [179, 180].

The DNA origami, serving as an alternative method for diamond surface functionalization, is compatible with many sensing applications of the NV center. For example, our NV-origami sensing scheme is readily applicable to detect small traces of ssDNA in the solution, or as illustrated in Fig. 6.10(a), the structure-switching events of aptamers. Aptamers are artificial short sequences of DNA, RNA, or peptide that can specifically bind to target molecules in a similar way to antibodies [181]. Assuming the solution containing target molecules is covering the diamond surface, which hosts a layer of shallow NV ensemble with the same properties as in this work, the triangle origami used in this work provides binding sites with a density up to around 0.026 nm^{-2}. Therefore, if one only deposits origami onto a 1000 $\mu\mathrm{m}^2$ area to fully cover the wide-field laser spot, the binding sites can be conjugated to 4.3×10^{-17} mole target molecules. In Fig. 6.10(b), we show the estimation of detection time under the realistic conditions of the confocal setup in this work and a typical wide-field setup as described above. The sensing volume of NV relaxometry when using Gd^{3+} spin labels is rather small. A 100-nm thick layer of solution on the surface will suffice, which corresponds to only 0.1 pL.

Given the requirement of only an atto-moles amount of aptamer and pico-litters sample L004onsumption volume, the limit of detection (LOD) and sensitivity of target molecule concentration are instead constrained by (1) other properties of NV ensembles including the total surface area being measured, PL, and overhead time in the pulse sequence; (2) the equilibrium dissociation constants (K_D) of the aptamers reacting with both origami binding sites and target molecules; (3) the molecule dynamics and the approach of solution delivery to diamond surface if the solution has a large volume and is not homogeneous. Assuming the aptamer's dissociation constant with target

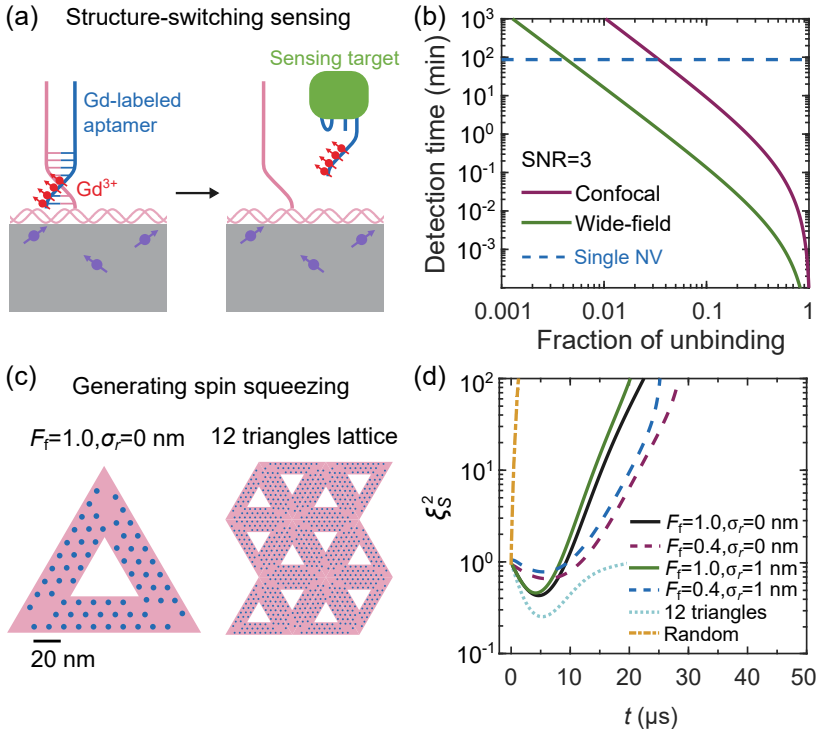

Figure 6.10: Potential applications of the NV-origami platform. (a) Sensing of structure-switching events of the Gd-labeled aptamer. (b) Minimal detection time required for sensing the percentage of empty binding sites under various sensing conditions, assuming SNR=3. The dashed line represents the detection time of a 4.5-nm deep NV center to detect the structure-switching event of an aptamer. (c) The spin arrays that one could pattern by origami triangles to generate spin squeezing. The filling factor F_{f} is the probability of each of 66 binding sites to be occupied by a spin. The positional disorder σ_r is the positional uncertainty of each spin. (d) Discrete truncated Wigner approximation (DTWA) simulation of quench dynamics of the spin arrays measured by the squeezing parameter ξ_S^2 under various spatial geometries, including different filling factor F_f and positional disorder σ_r, which is also compared to a larger lattice formed by 12 triangles and completely random spin geometry while keeping the same density.

molecules being $K_D = 1$ nM and sample volume of $V \gg 0.1$ μL, we can estimate the LOD concentration of target molecule at equilibrium to be 12 pM, (with 30 min measurement, wide-field, SNR=3). Furthermore, there are other potential advantages of the NV-origami platform, including the μm-scale spatial resolution, reproducibility, and less device-dependence if the density and depth of NVs are known or well controlled.

DNA origami is also promising for engineering a strongly interacting spin network. For example, in a numerical simulation, we observed the generation of spin squeezing using 66 binding sites in the current triangular origami design shown in Fig. 6.10(c). We simulate the quantum spin dynamics by the discrete truncated Wigner approximation (DTWA) method [182]. This method is well suited to capture the mean-field quantum correlation and describe the spin squeezing quantitatively in the dipolar-interacted spin systems [183, 184]. The spin squeezed state is prepared by quenching from a coherent spin state along +x axis of the Bloch sphere under the magnetic dipole-dipole interaction for the spin-1/2 system:

$$\hat{H} = \sum_{i \neq j} \frac{J}{r_{i,j}^3} (\hat{S}_i^x \hat{S}_j^x + \hat{S}_i^y \hat{S}_j^y - 2\hat{S}_i^z \hat{S}_j^z), \tag{6.10}$$

where J is the coupling strength and is equal to 52 MHz$\cdot$nm^3, $r_{i,j}$ is the distance between two spins, and $\hat{S}_i$ are the spin operators of each spin. The time evolution of a spin-1/2 ensemble can be measured by the squeezing parameter, $\xi_S^2 = \min_\theta \mathrm{Var}(S_\theta)/S_x^2$. As shown in Fig. 6.10(d), with a filling factor of $F_\mathrm{f} = 1.0$ and no positional disorder, the state is spin-squeezed as ξ_S^2 drops below 1. The positional disorder of 1 nm does not deteriorate the squeezing significantly. We also consider a smaller filling factor since the hybridization of spin-labeled ssDNA may not be perfect, and the yield rate may not be 100% if using other conjugation methods instead of click chemistry. With a filling factor of $F_\mathrm{f} = 0.4$, we still observe a spin squeezing, although ξ_S^2 drops to a higher value. Furthermore, in

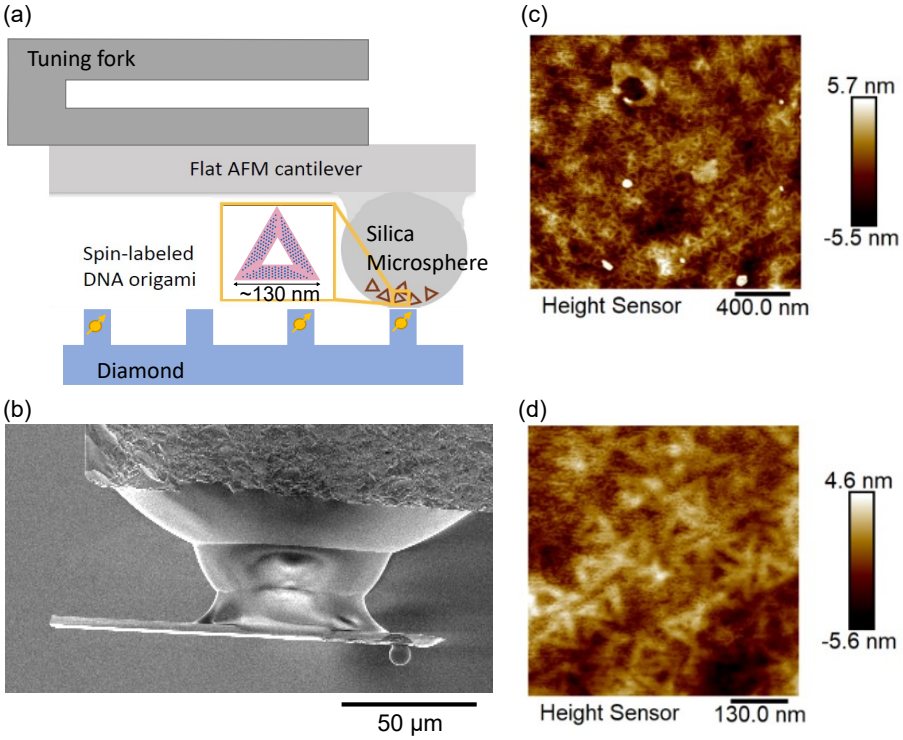

Figure 6.11: NV scanning T_1 relaxometry to detect spin-labeled DNA origami deposited on microsphere. (a) The schematic of the experiment. The triangular origami is deposited onto a SiO_2 microsphere. Diamond nanopillar with a single shallow NV center can be positioned near the top of the microsphere to enable scanning experiments. (b) Scanning electron microscopy (SEM) of the structure of the microsphere, cantilever, and tuning fork glued together. (c) The dry AFM image (Bruker Dimension Icon, tapping mode) of the top of a SiO_2 microsphere covered by triangular DNA origami. The microspheres are dried on a clean coverslip. (d) The zoomed AFM image of (c) shows triangle origami features.

future experiments, one could consider using origami that can connect with each other to form a larger lattice. We also simulate a lattice formed by twelve triangles, shown in Fig. 6.10(c)(d), and observe a stronger spin squeezing.

6.5 The challenge of single Gd^{3+} spin imaging using scanning NV relaxometry

Magnetic Resonance Imaging (MRI) is an essential non-invasive technique for detecting nuclear spins, making great contributions to chemistry, material science, and structural biology. Traditional MRI, however, requires around 10^{12} nuclear spins to produce a signal, limiting its spatial resolution to about 10^{12} nm^3. Similarly, techniques like X-ray crystallography and cryo-Electron Microscopy (cryo-EM) struggle to image individual proteins. Advances in nanoscale quantum sensors, especially nitrogen-vacancy (NV) centers in diamonds, have the potential to surpass these previous methods. The NV center has recently showcased the ability to detect nuclear magnetic resonance signals with a resolution of 5 nm (for single NV) [165] or a few μm (for NV ensemble) [185]. This makes the single NV center, when combined with scanning probe microscopy (SPM), a possible tool for investigating single nuclear spins in individual proteins, offering insights into protein structures. As the first step, we propose to use T_1 relaxometry to image Gd^{3+} ions patterned on DNA origami to test and improve the imaging resolution, sensitivity, and robustness of the sample preparation, as shown in Fig. 6.11(a). Leveraging a spin-to-charge conversion (SCC) readout technique to boost sensitivity, our laboratory has already achieved T_1 relaxometry imaging with a high resolution close to the requirement of imaging single Gd^{3+} [60].

We have made the first attempt on our room temperature scanning NV setup. We start with an AFM cantilever glued (UV glue) on the end of a tuning fork by a micromanipulator system. Then, we deposited Gd-labeled DNA origami on the surface of the clean 8-μm SiO_2 microspheres and AFM to validate the surface coverage (See Appendix for the protocol). An example of a microsphere covered with triangular origami is shown in Fig. 6.11(c)(d). We glued a microsphere on top of the cantilever and made sure that

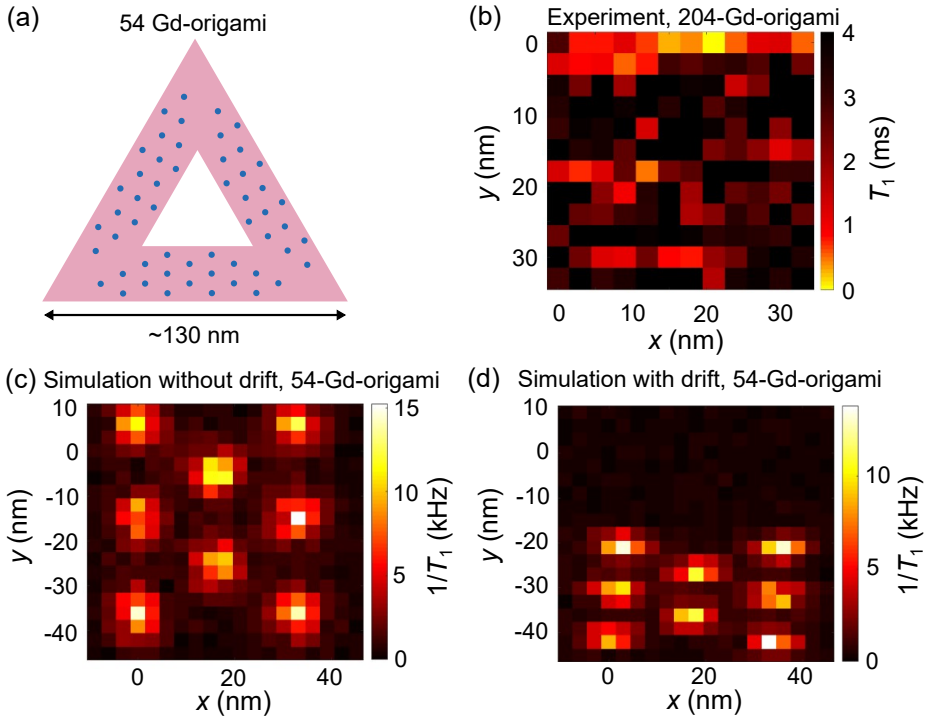

Figure 6.12: The experiment attempt and simulation of Gd^{3+} arrays detection by NV scanning relaxometry. (a) The schematic of a Gd-origami with 54 binding sites. Each binding site can host a single Gd^{3+} spin label. (b) The scanning experiment with Gd-origami (204 Gd^{3+} per triangle) deposited onto a microsphere using spin-to-charge conversion (SCC) readout technique. Tapping mode is used with feedback on the amplitude of tuning fork vibration. We observed T_1 reduction, but stable imaging that clearly displays the arrays of spins was not achieved. This scanning image took about 5 hours. (c) Numerical simulation for the scanning experiment with Gd-origami is shown in (a). We assume a noise level of 15× spin-projection limit for SCC readout, 7-nm distance between origami and the scanning NV. The image is averaged for 1 min per pixel and 6 hours for the whole image. We also assume ideal adaptive T_1 measurements. (d) The simulation with drift is being considered. We assume a drift of 1 nm/hour in the x-direction and 10 nm/hour in the y-direction, which is challenging but achievable in a scanning NV setup.

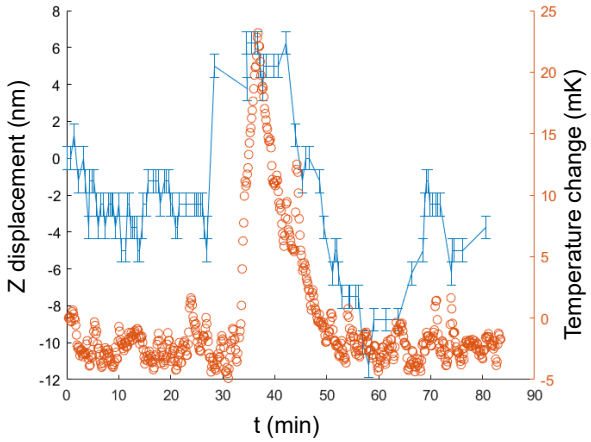

Figure 6.13: Testing stability of our room temperature NV scanning setup. The temperature is maintained around 5 K above the room temperature by the heating wires in the sample box controlled through a PID controller, and it is intentionally disturbed at $t \approx 32$ min.

the microsphere would engage into the diamond first. The tuning fork is then glued onto a sliced coverslip and connected to the AFM control circuit. Diamond nanopillar structures are used in our work to serve as the "AFM probe". We pre-measured each nanopillar to make sure the nanopillar we used for scanning does host a single shallow NV that has a long T_1. The confocal microscope can be directly used to image PL features caused by the cantilever and the microsphere as well [59].

Although we observed T_1 reduction in our scanning experiment, as shown in Fig. 6.12(b), the results are not conclusive because we did not observe any spin array pattern expected from the origami design. One of the main challenges for this experiment is the mechanical drift between the microsphere and the diamond at room temperature. By keeping the space around the objective and sample in a plastic box with acoustic foams and maintaining the temperature 5 Kelvin above the outside room temperature through a PID controlled heating wires, the best temperature stability we can achieve is on the order of 2-5 mK (standard deviation). We tested the stability of the scanning setup by measuring the relative z displacement when engagement happens while we

intentionally disturbed the temperature, as shown in Fig. 6.13. We also measured the long-term drift in the x and y directions and found a similar value of around 1-10 nm/hour. However, due to the high intrinsic measurement time required to detect single Gd^{3+} by a single NV through relaxometry, the corresponding displacement is still large compared to the imaging speed. As shown in Fig. 6.12(d), we have assumed a constant drift of 1 nm/hour in the x-direction and 10 nm/hour in the y-direction, and the image already becomes heavily distorted. Moreover, we lack an obvious AFM feature with the microsphere to register the image back after drifting [60]. We observed a drift of up to about 10 nm/hour in x, y, and z directions (relative distance between the microsphere and diamond nanopillar) for our scanning setup. Another two potential problems that need our further investigation are whether the DNA origami are preserved during the scanning and whether the diamond surface is not contaminated.

6.6 Summary and outlook

The observed strong correlation between the density of Gd^{3+} and NV ensemble relaxation rate $1/T_1$ indirectly validates the capability of patterning Gd^{3+} spins on diamond via origami. Future studies, such as using single NV scanning relaxometry to image Gd^{3+} spin arrays, could offer more direct insights and assess the positional disorder of spins. Furthermore, single NVs with known depths could be the better method to quantitatively study the relaxation mechanism associated with Eq. (6.9) and measure the correlation time of Gd^{3+}.

Optimizing the origami design for spin array formation and refining the deposition process are also essential next steps. Shortening the linker between Gd-DOTA chelates and the DNA base, currently a nine-carbon chain with a 1,2,3-triazole from click chemistry, could reduce the spin label's positional disorder. Additionally, the deposition pro-

tocol may be further improved to minimize the unwanted residual on the surface from the buffer and decrease the uncertainty in the fractional surface coverage. Moreover, exploring alternative origami configurations where the individual origami connect each other to form a larger lattice may offer additional avenues for advancement.

Our research presents a novel approach to utilizing external spins as auxiliary spins, enhancing quantum sensing capabilities. Traditional methods of attaching molecules to a diamond surface often lead to significant challenges, such as high positional disorder, uncontrolled molecule density, orientation, and binding configurations. Additionally, altering the diamond surface's termination, whether through covalent bonding to molecules or depositing other materials, typically degrades the spin coherence and charge state properties of shallow NV centers [24, 25]. Our innovative use of DNA origami to attach target molecules to the diamond surface demonstrates exceptional control over spin density while preserving the spin coherence and charge state stability of shallow NV centers. This method ensures a well-defined binding configuration for the molecules, as they are first attached to the ssDNA via click chemistry, with the yield rate thoroughly verified. In cases where alternative conjugation chemistries have to be used, if the yield rate is not nearly 100%, the product can be first purified before hybridization with the DNA origami. Regarding the orientation of the molecules, in theory, the motion of the target molecule should be restricted when bonded to the DNA via a short chain of atoms. This aspect certainly needs further investigation to fully understand the implications for quantum sensing applications.

Our work also establishes a foundation for sensing strongly interacting spin arrays patterned via origami. To date, there have been limited studies employing solid-state spin defect systems for quantum simulation [155, 142]. A critical challenge in this domain remains the high positional disorder among qubits and other dark spins such as P1s. Once spin defects are created within a lattice, the current technology does not offer a

viable means to reposition them precisely or reduce this inherent disorder. For example, the efforts to achieve phenomena such as spin squeezing in NV ensembles can be hampered by this positional disorder. Instead, our work may show us a promising alternative: engineering low-dimensional spin arrays on DNA origami substrates, which can then be probed using NV centers. Theoretical studies have shown that such strongly interacting dipole systems potentially can host exotic phenomena, including the many-body localization and quantum spin liquids, which are characterized by long-range entanglement [140, 158, 186].

Nevertheless, sensing coherent spins on origami at low temperatures still remains a challenge. Future experiments need to test the stability of spin-labeled DNA origami on the diamond surface in the cryogenic chamber, evaluate the magnitude of the signal background from other g=2 surface spins, and measure the coherence time of those coherent spins on origami at low temperatures. Our group is actively engaged in this research, continually conducting experiments and making progress.

Appendix A

Preparation of diamond samples and RF waveguide

A.1 Fabrication process of diamond sample B033

The diamond begins as a polished, commercial Element Six electronic grade (100) diamond substrate of lateral dimensions 2 mm × 2 mm and a thickness of 0.5 mm. The diamond is sliced to reduce the thickness and then polished from the sliced side to a thickness of 150 μm. Polishing damage is then mitigated by etching 1 μm of the surface with $ArCl_2$ plasma. Then the substrate is cleaned for 40 minutes in boiling acids of H_2NO_3:H_2SO_4 2:3. A 50-nm-thick layer of 99.99% ^{12}C is then grown on the substrate by plasma-enhanced chemical vapor deposition. To form NV centers, ^{14}N ions are then implanted with a dosage of 5.2×10^{10} ions/cm^2 at 4 keV and a 7° tilt. The expected average depth of the implanted nitrogen is 7 nm, calculated by the Stopping and Range of Ions in Matter (SRIM) program. Subsequently, the sample is annealed in the vacuum ($<10^6$ Torr at max temperature) at 850 °C for 2.5 hours with a 40-minute temperature ramp. After annealing, the sample is cleaned in boiling acids of $HClO_4$:H_2NO_3:H_2SO_4

1:1:1 for 1 hour at around 230-240 °C. Materials processing techniques used here are similar to those detailed and characterized in Reference [39]. To increase the photon collection efficiency from the NV centers, tapered nano-pillar structures with a diameter of 400-nm are patterned by e-beam lithography and etched by O_2 plasma to a height of 500 nm. The NV properties in this work are measured after a standard surface preparation protocol: the diamond is acid cleaned with boiling piranha solution for 12 minutes, and then the sample is oxygen annealed at 400 °C for 4 hours.

A.2 Fabrication process of diamond sample L021 and L026

A high-quality grown diamond epilayer on top of an electronic grade [100] oriented diamond substrate (from Element Six Ltd.). The substrate is first fine-polished by Syntek Ltd. and then etched for 4-5 μm to relieve strain before the growth. The growth is using plasma-enhanced chemical vapor deposition (PECVD) technique (SEKI SDS6300 reactor) with low power of plasma and low methane concentration to achieve a slow epitaxial growth rate of 10-30 nm/h [4]. The methane used here is isotopically purified, thus the resulting growth layer has a low concentration of ^{13}C ($\leq$ 0.002%) [4]. We created a delta-doped layer by introducing $^{15}N_2$ gas, and the delta-layer in L021 has a FWHM thickness of 3.55(4) nm and a depth of around 95 nm from top surface, measured by secondary ion mass spectrometry (SIMS) [4]. After growth, transmission electron microscope (TEM) (ThermoFisher Talos F200X G2) with 200 keV electrons was used to further augment the NV density by creating more single vacancies before annealing. Then, the sample was annealed at 850 ℃ for 6 h in an Ar/H_2 atmosphere, which allows the vacancies to diffuse to either form NV centers or move out of the diamond lattice.

Finally, the diamond was cleaned in piranha solution (3:1 H_2SO_4:H_2O_2) and annealed in O_2 at 450 ℃ for 2 hours to ensure an oxygen terminated surface. Sample L026 is prepared with the same procedure, resulting in a delta-doped layer, which has a FWHM thickness of 4.06(7) and a depth of 90 nm.

A.3 Fabrication process of diamond sample L004

Sample L004 is grown in a similar way to sample L021 and L026, except there is no delta-doped layer. The epitaxial growth was performed via PECVD using a SEKI SDS6300 reactor on a [100] oriented electronic grade diamond substrate (Element Six Ltd.). Prior to growth, the substrate was fine-polished by Syntek Ltd. to a surface roughness of ∼200-300 pm, followed by a 500 nm etch to relieve polishing-induced strain. The growth conditions consisted of a 750 W plasma containing 0.1% $^{12}CH_4$ in 400 sccm H_2 flow held at 25 torr and ∼800 °C. A ∼120 nm-thick isotopically purified (99.98% ^{12}C) epilayer was grown. After growth, to create a dense two-dimensional shallow NV ensemble, the sample was implanted with ^{14}N (2.5 keV and 1e13 cm^{-2} dose) by INNOVion and annealed in an Ar/H_2 atmosphere at 850°C for 2 hours. After this first round of high temperature anneal, we found the NV T_2 of a specific location is 1.8 μs. Then the sample is annealed again at 1200°C for 2 hours. After annealing, the sample is cleaned in tri-acid ($HClO_4$:H_2NO_3:H_2SO_4 1:1:1) for 1 hour at 150°C, then annealed in air at 450°C for 4 hours. We observed the NV T_2 from the same location increased to 2.2 μs. Then to further augment the NV density, we performed TEM (Talos F200X G2 TEM) irradiation over several areas of this sample with different dosages at 200 keV. After irradiation, the sample is then annealed in an Ar/H_2 atmosphere at 1200°C for another 2 hours, cleaned again in tri-acid for 1 hour at 150°C, annealed in air at 450°C for 4 hours, and cleaned in boiling piranha solution (H_2SO_4:H_2O_2 3:1) for 20 min. The final NV T_2 from the same

location increased to 3.4 μs.

A.4 Fabrication process for coplanar waveguide

The recipe for making the omega coplanar waveguides is as follows [187]. A useful rule of thumb for the recipe is that one should follow the time duration of baking, exposure and development exactly (as accurate as 1 second). Also, one may not want to wait too long between each step in order to achieve a high-quality waveguide.

1. Start with a clean substrate. We have tested 75x25x0.140 mm^3 glass coverslips, glass slide and sapphire, and this protocol works well on all of them.

2. Solvent clean the substrate by sonicating in acetone followed by IPA for 5 min each and dry with nitrogen.

3. Bake at 80 ℃ for 5 minutes to make sure all solvent has evaporated. Or just wait for long enough so that the surface is dry completely.

4. Spin HMDS at 4000 kRPM for 30 seconds.

5. Bake at 115 ℃ for 60 seconds.

6. Spin AZ5214-IR at 400 kRPM for 30 seconds.

7. Bake at 95 ℃ for 60 seconds.

8. Use contact lithography tool SUSS MJB-3 at 7.5 mW/cm^2 of power. Expose under the mask for 5 seconds. If using a different power, keep the total UV dose to be the same. For example, when using 7.0 mW/cm^2, the exposure time should be 5.4 seconds.

9. Post-exposure bake at 110 ℃ for 60 seconds.

10. Flood exposure (without any mask) at 7.5 mW/cm^2 for 60 seconds. When using 7.0 mW/cm^2, the exposure time should be 64.3 seconds.

11. Develop 45 seconds in AZ300MIF.

12. Rise in DI water for 3 minutes.

13. Deposit 10 nm Ti, 400 nm Au, (and 10 nm Pt if doing the SiO_2 capping layer) using electron beam evaporation (E-beam 3 in UCSB nanofabrication facility).

14. Lift off using acetone and follow with an IPA clean.

15. (Optional for doing aqueous sensing experiment.) Deposit 100 nm of SiO_2 using PECVD. Do this step in two 50 nm steps to prevent pin holes forming in the SiO_2 layer.

Appendix B

Additional protocols for DNA origami experiment

B.1 Protocols for creating DNA origami coated microspheres

Well-controlled deposition of DNA origami on a surface with large curvature is an interesting challenge. For our scanning experiment, we only need to use a microsphere that has a much larger diameter compared to the size of a DNA origami (∼130 nm). We use monodisperse silica microspheres of around 8-μm diameter with a coefficient of variance $< 2\%$ (Cospheric LLC.).

We first clean the Silica Microsphere using the following procedure:

1. Weight the microspheres in order to calculate the concentration. We typically use $\sim 10^{-2}$ pM concentration of microspheres, which corresponds to roughly 20 mg of microsphere in 5.5 mL Milli-Q water (Millipore).

2. Sonicate (in plastic vial to prevent abrasion) in acetone for 3 min.

3. Rinse in IPA for 5 times. Use the centrifuge or wait till the microspheres sink to the bottom of the vial. Then sonicate in IPA for 3 min.

4. Rinse in DI water for 5 times. Then sonicate in DI water for 3 min.

5. Etch in 4 M KOH solution at 70 °C for 90 min. Continually shaking the vial every 3 min to prevent microspheres from sinking to the bottom of the vial.

6. Rinse in DI water for 5 times.

7. Dilute or concentrate the solution if needed. Store in Milli-Q water. The solution can be used for very long time if one is careful not to contaminate the solution.

Then, the coverslip (22 mm × 22 mm, Fisherfinest, 12548B) used for drying the origami coated microsphere needs to be carefully cleaned first.

1. Load the coverslip in the racks (6817B, Newcomer Supply; 50949462, Electron Microscopy Sciences) sitting in glass jars.

2. Sonicate for 10 min in Milli-Q water containing 0.1 vol % of concentrated cleaning solution (Micro-90, International Products Corp).

3. Rinse the coverslips with the racks at least five times with Milli-Q water (by filling the glass jars with water and gently shaking to remove soap residue).

4. Incubated in 2 M NaOH for 30 min to etch away a thin layer of glass. Rinse five times with Milli-Q water to remove the remaining NaOH.

5. Pour the water out and fill the container with IPA. Do not use other kind of solvent to prevent residuals on coverslips when dried.

6. After 1 min, pour out the IPA and dry the whole rack and the container in the fume-hood or an oven if allowed by lab safety rules.

Finally, the DNA origami can be deposited onto the microsphere while in solution, and then dried on a clean coverslip:

1. Add 80 μL of 40mM Tris/Mg pH=8.5 buffer into a 0.5 mL LoBind tubes (Eppendorf).

2. Add 2 μL of 40 nM spin-labeled origami and 2 μL of 10^{-2} pM microspheres. Use pipetting to mix the solution.

3. Vortex at a low speed for 15 min ($\sim$1000 rpm).

4. Centrifuge to pull microspheres down to the bottom of the tube. Then add 240 μL of Tris/$MgCl_2$ buffer (pH=8.40). Repeat this step one more time.

5. Now repeat last step but with the "stabilizing" buffer (40 mM Tris/$MgCl_2$, pH=8.90). (Wash two times.)

6. Take off $\sim$240 uL buffer on top. Then add 240 μL 75% IPA in water (v/v%) for 1 time, centrifuge, pipette $\sim$240 μL solution off.

7. Repeat the last step but with 240 μL 100% IPA to wash the microspheres instead for 4 times. Then pipette away excess IPA. The left solution is about 10 μL.

8. Drop a 2 μL solution onto a clean coverslip, and let it dry itself in the open air.

9. AFM image the microsphere to check the quality. (A finer AFM probe with a 2-8 nm tip radius gives better images.)

Note that (1) After centrifuging, the pellet is visible at the bottom of the tube. The visibility in different solutions should be Tris/Mg buffer > 100% IPA > 75% IPA. (2) When the microspheres are successfully covered with origami, after the same condition of centrifuging, the microspheres usually become more adhesive to the tube wall, sometimes leaving a visible "tail" along the tube wall.

B.2 Protocols for conjugating Gd-p-SCN-Bn-DOTA to ssDNA with amine group

The amine group functionalized ssDNA is purchased from IDT (with an Amino Modifier C6). The isothiocyanates (SCN group) labeled Gd-DOTA (Gd-p-SCN-Bn-DOTA) is

purchased from Macrocyclics. Isothiocyanates form thioureas upon reaction with amines in just aqueous condition without catalyst, thus attaching the Gd-DOTA to the ssDNA. The reaction yield rate we achieved in our lab is usually only around 40%; therefore, we need to further purify the product by liquid chromatography (LC). The synthesis protocol is as follows:

1. For every 100 μL of the reaction mixture, add 81.5 μL sodium borate buffer (100 mM, pH=8.5), 8.5 μL 60 mM Gd-DOTA in water (510 nmol), 10uL 3mM ssDNA polyT-amine (30 nmol).

2. Incubate the reaction for 48 hours at room temperature. Vortex the mixture every 30 min in the first 2 hours. Then store it at 4 Celsius.

3. Use proFIRE ion-exchange LC system (Dynamic Biosensor) for purification. Use buffer A of 50 mM Phosphate buffer 0.15 M NaCl, Buffer B of 50 mM Phosphate buffer 1 M NaCl. Flow rate = 1 mL/min. The gradient we run is 0-3 min 100%A; 3.5-6.4 min 75%A; 6.5-16.4 min 73.5%A; 16.5-20.4 min 70%A; 20.9 min 25%A; 20.95-22 min 0%A; 22.05-27 min 100%A. Collect from 9.8-11.8min, the result if using 20T-amine.

4. Use Zymo DNA clean and concentrator to desalt some 20T-Gd-DOTA strands for PAGE analysis to confirm this purification step.

5. Use GE Healthcare illustra NAP-25 columns (use 10 mM Tris/$MgCl_2$ as the buffer) to desalt the 20T-Gd-DOTA (about 4 mL). When loading with 2.5 mL, one drop of water from NAP-25 is around 45 μL, collecting every 6 drops (270 μL) using a tube.

6. If needed, use a vacuum evaporator to concentrate the DNA solution. Use DNA SpeedVac (DNA 110), use the "low rate" for a lower temperature. Put 1 mL into one tube, and typically it takes around 1 hour to remove 200 μL of water.

Given the complexity of this protocol compared to click chemistry, we currently only use click chemistry for the conjugation of ssDNA.

B.3 Polyacrylamide Gel Electrophoresis

Polyacrylamide Gel Electrophoresis (PAGE) can also be used to confirm the conjugation results after LC. The protocol we have used is as follows:

1. Make 30 mL 15% acrylamide in 8.3 M UREA and 15 mL 5% acrylamide in 8.3 M UREA. Make fresh 10% APS, $(NH_4)_2S_2O_8$, can be stored at 4°C for a week.

2. Assemble the gel unit, make sure it's horizontal, clean glass, and no leakage.

3. First add 150 μL $(NH_4)_2S_2O_8$ and 15 μL N'N'N'N'-Tetramethylethylenediamine to the 15% acrylamide. Mix well and slowly. Pour it between the glass plates. Then add 200 μL IPA to it from the middle. Wait 30 min for the gel to form.

4. Add 75 μL $(NH_4)_2S_2O_8$ and 10 μL N'N'N'N'-Tetramethylethylenediamine to the 5% acrylamide. Mix well and slowly. Pour this stacking gel. Put the comb in. Wait another 1 h. Wash the gel's top using Milli-Q water.

5. Put the gel (in the glass plates) into the big buffer box. Add 1x TBE buffer to the top. Pre-run the gel at 300 Volts for 30 min at 55℃.

6. Pipette up and down in each well to make sure the glassy thing goes away. Then load 5 wells with our prepared samples.

7. Run the gel for 1 h and 15 min at 300 Volts, 55℃.

8. Post stain. We use 1x Sybr Gold, in 8.3M UREA. We put the gel on a kitchen wrap (SARAN) which sits in a plastic tray. Put it on a rocker for 20 min.

9. Image. Use a hand-held UV light source in the dark. Use a scanner to take pictures (BIO-RAD, Molecular-Imager FX pro).

Bibliography

[1] D. Bluvstein, Z. Zhang, and A. C. B. Jayich, *Identifying and mitigating charge instabilities in shallow diamond nitrogen-vacancy centers*, *Phys. Rev. Lett.* **122** (Feb, 2019) 076101.

[2] D. Bluvstein, Z. Zhang, C. A. McLellan, N. R. Williams, and A. C. B. Jayich, *Extending the quantum coherence of a near-surface qubit by coherently driving the paramagnetic surface environment*, *Phys. Rev. Lett.* **123** (Oct, 2019) 146804.

[3] Z. Zhang, M. Joos, D. Bluvstein, Y. Lyu, and A. C. Bleszynski Jayich, *Reporter-spin-assisted T_1 relaxometry*, *Phys. Rev. Appl.* **19** (Mar, 2023) L031004.

[4] L. B. Hughes, Z. Zhang, C. Jin, S. A. Meynell, B. Ye, W. Wu, Z. Wang, E. J. Davis, T. E. Mates, N. Y. Yao, K. Mukherjee, and A. C. Bleszynski Jayich, *Two-dimensional spin systems in PECVD-grown diamond with tunable density and long coherence for enhanced quantum sensing and simulation*, *APL Materials* **11** (02, 2023) 021101.

[5] M. Steger, K. Saeedi, M. L. W. Thewalt, J. J. L. Morton, H. Riemann, N. V. Abrosimov, P. Becker, and H.-J. Pohl, *Quantum information storage for over 180 s using donor spins in a 28si semiconductor vacuum*, *Science* **336** (2012), no. 6086 1280–1283.

[6] D. D. Awschalom, R. Hanson, J. Wrachtrup, and B. B. Zhou, *Quantum technologies with optically interfaced solid-state spins*, *Nature Photonics* **12** (Sept., 2018) 516–527.

[7] G. Wolfowicz, F. J. Heremans, C. P. Anderson, S. Kanai, H. Seo, A. Gali, G. Galli, and D. D. Awschalom, *Quantum guidelines for solid-state spin defects*, *Nature Reviews Materials* **6** (Oct., 2021) 906–925.

[8] C. Hepp, T. Müller, V. Waselowski, J. N. Becker, B. Pingault, H. Sternschulte, D. Steinmüller-Nethl, A. Gali, J. R. Maze, M. Atatüre, and C. Becher, *Electronic structure of the silicon vacancy color center in diamond*, *Phys. Rev. Lett.* **112** (Jan, 2014) 036405.

[9] L. J. Rogers, K. D. Jahnke, T. Teraji, L. Marseglia, C. Müller, B. Naydenov, H. Schauffert, C. Kranz, J. Isoya, L. P. McGuinness, and F. Jelezko, *Multiple intrinsically identical single-photon emitters in the solid state*, *Nature Communications* **5** (Aug, 2014) 4739.

[10] W. F. Koehl, B. B. Buckley, F. J. Heremans, G. Calusine, and D. D. Awschalom, *Room temperature coherent control of defect spin qubits in silicon carbide*, *Nature* **479** (Nov, 2011) 84–87.

[11] A. L. Falk, B. B. Buckley, G. Calusine, W. F. Koehl, V. V. Dobrovitski, A. Politi, C. A. Zorman, P. X.-L. Feng, and D. D. Awschalom, *Polytype control of spin qubits in silicon carbide*, *Nature Communications* **4** (May, 2013) 1819.

[12] A. L. Falk, P. V. Klimov, B. B. Buckley, V. Ivády, I. A. Abrikosov, G. Calusine, W. F. Koehl, A. Gali, and D. D. Awschalom, *Electrically and mechanically tunable electron spins in silicon carbide color centers*, *Phys. Rev. Lett.* **112** (May, 2014) 187601.

[13] D. J. Christle, A. L. Falk, P. Andrich, P. V. Klimov, J. U. Hassan, N. Son, E. Janzén, T. Ohshima, and D. D. Awschalom, *Isolated electron spins in silicon carbide with millisecond coherence times*, *Nature Materials* **14** (Feb, 2015) 160–163.

[14] N. Ohlsson, R. Krishna Mohan, and S. Kröll, *Quantum computer hardware based on rare-earth-ion-doped inorganic crystals*, *Optics Communications* **201** (2002), no. 1 71–77.

[15] L. Rippe, M. Nilsson, S. Kröll, R. Klieber, and D. Suter, *Experimental demonstration of efficient and selective population transfer and qubit distillation in a rare-earth-metal-ion-doped crystal*, *Phys. Rev. A* **71** (Jun, 2005) 062328.

[16] F. Könz, Y. Sun, C. W. Thiel, R. L. Cone, R. W. Equall, R. L. Hutcheson, and R. M. Macfarlane, *Temperature and concentration dependence of optical dephasing, spectral-hole lifetime, and anisotropic absorption in* eu^{3+}: $\mathrm{Y_2sio_5}$, *Phys. Rev. B* **68** (Aug, 2003) 085109.

[17] M. Zhong, M. P. Hedges, R. L. Ahlefeldt, J. G. Bartholomew, S. E. Beavan, S. M. Wittig, J. J. Longdell, and M. J. Sellars, *Optically addressable nuclear spins in a solid with a six-hour coherence time*, *Nature* **517** (Jan, 2015) 177–180.

[18] K. Saeedi, S. Simmons, J. Z. Salvail, P. Dluhy, H. Riemann, N. V. Abrosimov, P. Becker, H.-J. Pohl, J. J. L. Morton, and M. L. W. Thewalt, *Room-temperature quantum bit storage exceeding 39 minutes using ionized donors in silicon-28*, *Science* **342** (2013), no. 6160 830–833.

[19] X. Mi, M. Benito, S. Putz, D. M. Zajac, J. M. Taylor, G. Burkard, and J. R. Petta, *A coherent spin–photon interface in silicon*, *Nature* **555** (Mar, 2018) 599–603.

[20] N. Samkharadze, G. Zheng, N. Kalhor, D. Brousse, A. Sammak, U. C. Mendes, A. Blais, G. Scappucci, and L. M. K. Vandersypen, *Strong spin-photon coupling in silicon*, *Science* **359** (2018), no. 6380 1123–1127.

[21] K. Momma and F. Izumi, *VESTA3 for three-dimensional visualization of crystal, volumetric and morphology data*, *Journal of Applied Crystallography* **44** (Dec, 2011) 1272–1276.

[22] J. H. N. Loubser and J. A. van Wyk, *Electron spin resonance in the study of diamond*, *Reports on Progress in Physics* **41** (aug, 1978) 1201.

[23] M. W. Doherty, N. B. Manson, P. Delaney, F. Jelezko, J. Wrachtrup, and L. C. Hollenberg, *The nitrogen-vacancy colour centre in diamond*, *Physics Reports* **528** (2013), no. 1 1–45. The nitrogen-vacancy colour centre in diamond.

[24] L. V. H. Rodgers, L. B. Hughes, M. Xie, P. C. Maurer, S. Kolkowitz, A. C. Bleszynski Jayich, and N. P. de Leon, *Materials challenges for quantum technologies based on color centers in diamond*, *MRS Bulletin* **46** (Jul, 2021) 623–633.

[25] E. Janitz, K. Herb, L. A. Völker, W. S. Huxter, C. L. Degen, and J. M. Abendroth, *Diamond surface engineering for molecular sensing with nitrogen—vacancy centers*, *J. Mater. Chem. C* **10** (2022) 13533–13569.

[26] D. Lee, K. W. Lee, J. V. Cady, P. Ovartchaiyapong, and A. C. B. Jayich, *Topical review: spins and mechanics in diamond*, *Journal of Optics* **19** (feb, 2017) 033001.

[27] V. M. Acosta, E. Bauch, M. P. Ledbetter, A. Waxman, L.-S. Bouchard, and D. Budker, *Temperature dependence of the nitrogen-vacancy magnetic resonance in diamond*, *Phys. Rev. Lett.* **104** (Feb, 2010) 070801.

[28] S. McGlynn, T. Azumi, and M. Kinoshita, *Molecular Spectroscopy of the Triplet State [by] S.P. Mc-Glynn, T. Azumi [and] M. Kinoshita*. Prentice-Hall international series in chemistry. Prentice-Hall, 1969.

[29] X.-F. He, N. B. Manson, and P. T. H. Fisk, *Paramagnetic resonance of photoexcited n-v defects in diamond. i. level anticrossing in the* ^{3}*a ground state*, *Phys. Rev. B* **47** (Apr, 1993) 8809–8815.

[30] A. Gruber, A. Dräbenstedt, C. Tietz, L. Fleury, J. Wrachtrup, and C. von Borczyskowski, *Scanning confocal optical microscopy and magnetic resonance on single defect centers*, *Science* **276** (1997), no. 5321 2012–2014.

[31] S. Felton, A. M. Edmonds, M. E. Newton, P. M. Martineau, D. Fisher, D. J. Twitchen, and J. M. Baker, *Hyperfine interaction in the ground state of the negatively charged nitrogen vacancy center in diamond*, *Phys. Rev. B* **79** (Feb, 2009) 075203.

[32] P. Deák, B. Aradi, M. Kaviani, T. Frauenheim, and A. Gali, *Formation of nv centers in diamond: A theoretical study based on calculated transitions and migration of nitrogen and vacancy related defects*, *Phys. Rev. B* **89** (Feb, 2014) 075203.

[33] P. E. Barclay, K.-M. C. Fu, C. Santori, A. Faraon, and R. G. Beausoleil, *Hybrid nanocavity resonant enhancement of color center emission in diamond*, *Phys. Rev. X* **1** (Sep, 2011) 011007.

[34] M. L. Goldman, M. W. Doherty, A. Sipahigil, N. Y. Yao, S. D. Bennett, N. B. Manson, A. Kubanek, and M. D. Lukin, *State-selective intersystem crossing in nitrogen-vacancy centers*, *Phys. Rev. B* **91** (Apr, 2015) 165201.

[35] R. Schirhagl, K. Chang, M. Loretz, and C. L. Degen, *Nitrogen-vacancy centers in diamond: Nanoscale sensors for physics and biology*, *Annual Review of Physical Chemistry* **65** (2014), no. 1 83–105.

[36] N. Aslam, G. Waldherr, P. Neumann, F. Jelezko, and J. Wrachtrup, *Photo-induced ionization dynamics of the nitrogen vacancy defect in diamond investigated by single-shot charge state detection*, *New Journal of Physics* **15** (jan, 2013) 013064.

[37] M. Steiner, P. Neumann, J. Beck, F. Jelezko, and J. Wrachtrup, *Universal enhancement of the optical readout fidelity of single electron spins at nitrogen-vacancy centers in diamond*, *Phys. Rev. B* **81** (Jan, 2010) 035205.

[38] P. Reineck, A. Francis, A. Orth, D. W. M. Lau, R. D. V. Nixon-Luke, I. D. Rastogi, W. A. W. Razali, N. M. Cordina, L. M. Parker, V. K. A. Sreenivasan, L. J. Brown, and B. C. Gibson, *Brightness and photostability of emerging red and near-ir fluorescent nanomaterials for bioimaging*, *Advanced Optical Materials* **4** (2016), no. 10 1549–1557.

[39] S. Sangtawesin, B. L. Dwyer, S. Srinivasan, J. J. Allred, L. V. H. Rodgers, K. De Greve, A. Stacey, N. Dontschuk, K. M. O'Donnell, D. Hu, D. A. Evans, C. Jaye, D. A. Fischer, M. L. Markham, D. J. Twitchen, H. Park, M. D. Lukin, and N. P. de Leon, *Origins of diamond surface noise probed by correlating single-spin measurements with surface spectroscopy*, *Phys. Rev. X* **9** (Sep, 2019) 031052.

[40] A. Dréau, M. Lesik, L. Rondin, P. Spinicelli, O. Arcizet, J.-F. Roch, and V. Jacques, *Avoiding power broadening in optically detected magnetic resonance of single nv defects for enhanced dc magnetic field sensitivity*, *Phys. Rev. B* **84** (Nov, 2011) 195204.

[41] A. Jarmola, V. M. Acosta, K. Jensen, S. Chemerisov, and D. Budker, *Temperature- and magnetic-field-dependent longitudinal spin relaxation in nitrogen-vacancy ensembles in diamond*, *Phys. Rev. Lett.* **108** (May, 2012) 197601.

[42] J. Choi, S. Choi, G. Kucsko, P. C. Maurer, B. J. Shields, H. Sumiya, S. Onoda, J. Isoya, E. Demler, F. Jelezko, N. Y. Yao, and M. D. Lukin, *Depolarization dynamics in a strongly interacting solid-state spin ensemble*, *Phys. Rev. Lett.* **118** (Mar, 2017) 093601.

[43] L. T. Hall, P. Kehayias, D. A. Simpson, A. Jarmola, A. Stacey, D. Budker, and L. C. L. Hollenberg, *Detection of nanoscale electron spin resonance spectra demonstrated using nitrogen-vacancy centre probes in diamond*, *Nature Communications* **7** (Jan, 2016) 10211.

[44] C. P. Slichter, *Spin-Lattice Relaxation and Motional Narrowing of Resonance Lines*, pp. 137–187. Springer Berlin Heidelberg, Berlin, Heidelberg, 1978.

[45] R. J. Schoelkopf, A. A. Clerk, S. M. Girvin, K. W. Lehnert, and M. H. Devoret, *Qubits as Spectrometers of Quantum Noise*, pp. 175–203. Springer Netherlands, Dordrecht, 2003.

[46] J.-P. Tetienne, T. Hingant, L. Rondin, A. Cavaillès, L. Mayer, G. Dantelle, T. Gacoin, J. Wrachtrup, J.-F. Roch, and V. Jacques, *Spin relaxometry of single nitrogen-vacancy defects in diamond nanocrystals for magnetic noise sensing*, *Phys. Rev. B* **87** (Jun, 2013) 235436.

[47] B. A. Myers, A. Ariyaratne, and A. C. B. Jayich, *Double-quantum spin-relaxation limits to coherence of near-surface nitrogen-vacancy centers*, *Phys. Rev. Lett.* **118** (May, 2017) 197201.

[48] J. Gugler, T. Astner, A. Angerer, J. Schmiedmayer, J. Majer, and P. Mohn, *Ab initio calculation of the spin lattice relaxation time T_1 for nitrogen-vacancy centers in diamond*, *Phys. Rev. B* **98** (Dec, 2018) 214442.

[49] M. C. Cambria, A. Norambuena, H. T. Dinani, G. Thiering, A. Gardill, I. Kemeny, Y. Li, V. Lordi, A. Gali, J. R. Maze, and S. Kolkowitz, *Temperature-dependent spin-lattice relaxation of the nitrogen-vacancy spin triplet in diamond*, *Phys. Rev. Lett.* **130** (Jun, 2023) 256903.

[50] B. A. Myers, A. Das, M. C. Dartiailh, K. Ohno, D. D. Awschalom, and A. C. Bleszynski Jayich, *Probing surface noise with depth-calibrated spins in diamond*, *Phys. Rev. Lett.* **113** (Jul, 2014) 027602.

[51] A. Stacey, N. Dontschuk, J.-P. Chou, D. A. Broadway, A. K. Schenk, M. J. Sear, J.-P. Tetienne, A. Hoffman, S. Prawer, C. I. Pakes, A. Tadich, N. P. de Leon, A. Gali, and L. C. L. Hollenberg, *Evidence for primal sp2 defects at the diamond surface: Candidates for electron trapping and noise sources*, *Advanced Materials Interfaces* **6** (2019), no. 3 1801449.

[52] K. Rezai, S. Choi, M. D. Lukin, and A. O. Sushkov, *Probing dynamics of a two-dimensional dipolar spin ensemble using single qubit sensor*, 2023.

[53] L. Viola, E. Knill, and S. Lloyd, *Dynamical decoupling of open quantum systems*, *Phys. Rev. Lett.* **82** (Mar, 1999) 2417–2421.

[54] G. de Lange, Z. H. Wang, D. Ristè, V. V. Dobrovitski, and R. Hanson, *Universal dynamical decoupling of a single solid-state spin from a spin bath*, *Science* **330** (2010), no. 6000 60–63.

[55] R. de Sousa, *Electron Spin as a Spectrometer of Nuclear-Spin Noise and Other Fluctuations*, pp. 183–220. Springer Berlin Heidelberg, Berlin, Heidelberg, 2009.

[56] C. A. Ryan, J. S. Hodges, and D. G. Cory, *Robust decoupling techniques to extend quantum coherence in diamond*, *Phys. Rev. Lett.* **105** (Nov, 2010) 200402.

[57] L. M. Pham, N. Bar-Gill, C. Belthangady, D. Le Sage, P. Cappellaro, M. D. Lukin, A. Yacoby, and R. L. Walsworth, *Enhanced solid-state multispin metrology using dynamical decoupling*, *Phys. Rev. B* **86** (Jul, 2012) 045214.

[58] J. H. Shim, I. Niemeyer, J. Zhang, and D. Suter, *Robust dynamical decoupling for arbitrary quantum states of a single nv center in diamond*, *Europhysics Letters* **99** (aug, 2012) 40004.

[59] B. A. Myers, *Quantum decoherence of near-surface nitrogen-vacancy centers in diamond and implications for nanoscale imaging*. Phd dissertation, University of California, Santa Barbara, Santa Barbara, CA, 2016. Available at `https://alexandria.ucsb.edu/downloads/w9505083n`.

[60] A. Ariyaratne, D. Bluvstein, B. A. Myers, and A. C. B. Jayich, *Nanoscale electrical conductivity imaging using a nitrogen-vacancy center in diamond*, *Nature Communications* **9** (Jun, 2018) 2406.

[61] S. Inoué, *Foundations of Confocal Scanned Imaging in Light Microscopy*, pp. 1–19. Springer US, Boston, MA, 2006.

[62] S. An, M.-h. Hong, J. Kim, S. Kwon, K. Lee, M. Lee, and W. Jhe, *Quartz tuning fork-based frequency modulation atomic force spectroscopy and microscopy with all digital phase-locked loop*, *Review of Scientific Instruments* **83** (11, 2012) 113705.

[63] S. An, K. Lee, B. Kim, J. Kim, S. Kwon, Q. Kim, M. Lee, and W. Jhe, *Compensation of stray capacitance of the quartz tuning fork for a quantitative force spectroscopy*, *Current Applied Physics* **13** (2013), no. 9 1899–1905.

[64] F. J. Giessibl, F. Pielmeier, T. Eguchi, T. An, and Y. Hasegawa, *Comparison of force sensors for atomic force microscopy based on quartz tuning forks and length-extensional resonators*, *Phys. Rev. B* **84** (Sep, 2011) 125409.

[65] J. Welker, F. de Faria Elsner, and F. J. Giessibl, *Application of the equipartition theorem to the thermal excitation of quartz tuning forks*, *Applied Physics Letters* **99** (08, 2011) 084102.

[66] T. Gaebel, M. Domhan, C. Wittmann, I. Popa, F. Jelezko, J. Rabeau, A. Greentree, S. Prawer, E. Trajkov, P. Hemmer, and J. Wrachtrup, *Photochromism in single nitrogen-vacancy defect in diamond*, *Applied Physics B* **82** (feb, 2006) 243–246.

[67] K. Iakoubovskii, G. J. Adriaenssens, and M. Nesladek, *Photochromism of vacancy-related centres in diamond*, *Journal of Physics: Condensed Matter* **12** (jan, 2000) 189–199.

[68] N. Manson and J. Harrison, *Photo-ionization of the nitrogen-vacancy center in diamond*, *Diamond and Related Materials* **14** (oct, 2005) 1705–1710.

[69] M. V. Hauf, B. Grotz, B. Naydenov, M. Dankerl, S. Pezzagna, J. Meijer, F. Jelezko, J. Wrachtrup, M. Stutzmann, F. Reinhard, and J. A. Garrido, *Chemical control of the charge state of nitrogen-vacancy centers in diamond*, *Physical Review B* **83** (feb, 2011) 081304.

[70] L. Rondin, G. Dantelle, A. Slablab, F. Grosshans, F. Treussart, P. Bergonzo, S. Perruchas, T. Gacoin, M. Chaigneau, H.-C. Chang, V. Jacques, and J.-F. Roch, *Surface-induced charge state conversion of nitrogen-vacancy defects in nanodiamonds*, *Phys. Rev. B* **82** (Sep, 2010) 115449.

[71] K.-M. C. Fu, C. Santori, P. E. Barclay, and R. G. Beausoleil, *Conversion of neutral nitrogen-vacancy centers to negatively charged nitrogen-vacancy centers through selective oxidation*, *Applied Physics Letters* **96** (mar, 2010) 121907.

[72] J. M. Taylor, P. Cappellaro, L. Childress, L. Jiang, D. Budker, P. R. Hemmer, A. Yacoby, R. Walsworth, and M. D. Lukin, *High-sensitivity diamond magnetometer with nanoscale resolution*, *Nature Physics* **4** (oct, 2008) 810–816.

[73] D. Rugar, H. J. Mamin, M. H. Sherwood, M. Kim, C. T. Rettner, K. Ohno, and D. D. Awschalom, *Proton magnetic resonance imaging using a nitrogen–vacancy spin sensor*, *Nature Nanotechnology* **10** (feb, 2015) 120–124.

[74] B. J. Shields, Q. P. Unterreithmeier, N. P. de Leon, H. Park, and M. D. Lukin, *Efficient readout of a single spin state in diamond via spin-to-charge conversion*, *Phys. Rev. Lett.* **114** (Mar, 2015) 136402.

[75] X.-D. Chen, C.-L. Zou, F.-W. Sun, and G.-C. Guo, *Optical manipulation of the charge state of nitrogen-vacancy center in diamond*, *Applied Physics Letters* **103** (jul, 2013) 013112.

[76] Y. Doi, T. Fukui, H. Kato, T. Makino, S. Yamasaki, T. Tashima, H. Morishita, S. Miwa, F. Jelezko, Y. Suzuki, and N. Mizuochi, *Pure negatively charged state of the NV center in n -type diamond*, *Physical Review B* **93** (feb, 2016) 081203.

[77] Y. Doi, T. Makino, H. Kato, D. Takeuchi, M. Ogura, H. Okushi, H. Morishita, T. Tashima, S. Miwa, S. Yamasaki, P. Neumann, J. Wrachtrup, Y. Suzuki, and N. Mizuochi, *Deterministic electrical charge-state initialization of single nitrogen-vacancy center in diamond*, *Phys. Rev. X* **4** (Mar, 2014) 011057.

[78] D. A. Hopper, R. R. Grote, A. L. Exarhos, and L. C. Bassett, *Near-infrared-assisted charge control and spin readout of the nitrogen-vacancy center in diamond*, *Physical Review B* **94** (dec, 2016) 241201.

[79] A. N. Newell, D. A. Dowdell, and D. H. Santamore, *Surface effects on nitrogen vacancy centers neutralization in diamond*, *Journal of Applied Physics* **120** (nov, 2016) 185104.

[80] S. Dhomkar, P. R. Zangara, J. Henshaw, and C. A. Meriles, *On-Demand Generation of Neutral and Negatively Charged Silicon-Vacancy Centers in Diamond*, *Physical Review Letters* **120** (mar, 2018) 117401.

[81] S. Dhomkar, J. Henshaw, H. Jayakumar, and C. A. Meriles, *Long-term data storage in diamond*, *Science Advances* **2** (oct, 2016) e1600911–e1600911.

[82] H. Jayakumar, J. Henshaw, S. Dhomkar, D. Pagliero, A. Laraoui, N. B. Manson, R. Albu, M. W. Doherty, and C. A. Meriles, *Optical patterning of trapped charge in nitrogen-doped diamond*, *Nature Communications* **7** (aug, 2016) 12660.

[83] R. Giri, F. Gorrini, C. Dorigoni, C. E. Avalos, M. Cazzanelli, S. Tambalo, and A. Bifone, *Coupled charge and spin dynamics in high-density ensembles of nitrogen-vacancy centers in diamond*, *Physical Review B* **98** (jul, 2018) 045401.

[84] S. Dhomkar, H. Jayakumar, P. R. Zangara, and C. A. Meriles, *Charge Dynamics in near-Surface, Variable-Density Ensembles of Nitrogen-Vacancy Centers in Diamond*, *Nano Letters* **18** (jun, 2018) 4046–4052.

[85] R. Brouri, A. Beveratos, J.-P. Poizat, and P. Grangier, *Photon antibunching in the fluorescence of individual color centers in diamond*, *Optics Letters* **25** (sep, 2000) 1294.

[86] L. M. Pham, S. J. DeVience, F. Casola, I. Lovchinsky, A. O. Sushkov, E. Bersin, J. Lee, E. Urbach, P. Cappellaro, H. Park, A. Yacoby, M. Lukin, and R. L. Walsworth, *NMR technique for determining the depth of shallow nitrogen-vacancy centers in diamond*, *Phys. Rev. B* **93** (2016), no. 4 045425.

[87] L. Hacquebard and L. Childress, *Charge-state dynamics during excitation and depletion of the nitrogen-vacancy center in diamond*, *Physical Review A* **97** (jun, 2018) 063408.

[88] T. Staudacher, F. Shi, S. Pezzagna, J. Meijer, J. Du, C. A. Meriles, F. Reinhard, and J. Wrachtrup, *Nuclear magnetic resonance spectroscopy on a (5-nanometer)3 sample volume.*, *Science (New York, N.Y.)* **339** (feb, 2013) 561–3.

[89] H. J. Mamin, M. Kim, M. H. Sherwood, C. T. Rettner, K. Ohno, D. D. Awschalom, and D. Rugar, *Nanoscale Nuclear Magnetic Resonance with a Nitrogen-Vacancy Spin Sensor*, *Science* **339** (feb, 2013) 557–560.

[90] M. Loretz, J. M. Boss, T. Rosskopf, H. J. Mamin, D. Rugar, and C. L. Degen, *Spurious harmonic response of multipulse quantum sensing sequences*, *Physical Review X* **5** (apr, 2015) 021009.

[91] P. Deák, B. Aradi, M. Kaviani, T. Frauenheim, and A. Gali, *Formation of NV centers in diamond: A theoretical study based on calculated transitions and migration of nitrogen and vacancy related defects*, *Physical Review B* **89** (feb, 2014) 075203.

[92] A. Stacey, N. Dontschuk, J.-P. Chou, D. A. Broadway, A. K. Schenk, M. J. Sear, J.-P. Tetienne, A. Hoffman, S. Prawer, C. I. Pakes, A. Tadich, N. P. de Leon, A. Gali, and L. C. L. Hollenberg, *Evidence for primal sp2 defects at the diamond surface: Candidates for electron trapping and noise sources*, *Advanced Materials Interfaces* **6** (2019), no. 3 1801449.

[93] R. Farrer, *On the substitutional nitrogen donor in diamond*, *Solid State Communications* **7** (may, 1969) 685–688.

[94] B. A. Myers, A. Ariyaratne, and A. C. B. Jayich, *Double-quantum spin-relaxation limits to coherence of near-surface nitrogen-vacancy centers*, *Phys. Rev. Lett.* **118** (May, 2017) 197201.

[95] J.-P. Chou, Z. Bodrog, and A. Gali, *First-Principles Study of Charge Diffusion between Proximate Solid-State Qubits and Its Implications on Sensor Applications*, *Physical Review Letters* **120** (mar, 2018) 136401.

[96] F. Dolde, M. W. Doherty, J. Michl, I. Jakobi, B. Naydenov, S. Pezzagna, J. Meijer, P. Neumann, F. Jelezko, N. B. Manson, and J. Wrachtrup, *Nanoscale Detection of a Single Fundamental Charge in Ambient Conditions Using the NV Center in Diamond*, *Physical Review Letters* **112** (mar, 2014) 097603.

[97] T. Mittiga, S. Hsieh, C. Zu, B. Kobrin, F. Machado, P. Bhattacharyya, N. Z. Rui, A. Jarmola, S. Choi, D. Budker, and N. Y. Yao, *Imaging the local charge environment of nitrogen-vacancy centers in diamond*, *Phys. Rev. Lett.* **121** (Dec, 2018) 246402.

[98] R. S. Hayano, Y. J. Uemura, J. Imazato, N. Nishida, T. Yamazaki, and R. Kubo, *Zero-and low-field spin relaxation studied by positive muons*, *Phys. Rev. B* **20** (aug, 1979) 850–859.

[99] K. Agarwal, R. Schmidt, B. Halperin, V. Oganesyan, G. Zaránd, M. D. Lukin, and E. Demler, *Magnetic noise spectroscopy as a probe of local electronic correlations in two-dimensional systems*, *Phys. Rev. B* **95** (apr, 2017) 155107.

[100] B. Flebus and Y. Tserkovnyak, *Quantum-Impurity Relaxometry of Magnetization Dynamics*, *Phys. Rev. Lett.* **121** (nov, 2018) 187204.

[101] J. Y. Khoo, F. Pientka, and I. Sodemann, *The universal shear conductivity of Fermi liquids and spinon Fermi surface states and its detection via spin qubit noise magnetometry*, *New J. Phys.* **23** (2021), no. 11 113009.

[102] S. Chatterjee, P. E. Dolgirev, I. Esterlis, A. A. Zibrov, M. D. Lukin, N. Y. Yao, and E. Demler, *Single-spin qubit magnetic spectroscopy of two-dimensional superconductivity*, *Phys. Rev. Res.* **4** (2022), no. 1 L012001.

[103] P. E. Dolgirev, S. Chatterjee, I. Esterlis, A. A. Zibrov, M. D. Lukin, N. Y. Yao, and E. Demler, *Characterizing two-dimensional superconductivity via nanoscale noise magnetometry with single-spin qubits*, *Phys. Rev. B* **105** (2022), no. 2 024507.

[104] T. Rosskopf, A. Dussaux, K. Ohashi, M. Loretz, R. Schirhagl, H. Watanabe, S. Shikata, K. M. Itoh, and C. L. Degen, *Investigation of surface magnetic noise by shallow spins in diamond*, *Phys. Rev. Lett.* **112** (Apr, 2014) 147602.

[105] Y. Romach, C. Müller, T. Unden, L. J. Rogers, T. Isoda, K. M. Itoh, M. Markham, A. Stacey, J. Meijer, S. Pezzagna, B. Naydenov, L. P. McGuinness, N. Bar-Gill, and F. Jelezko, *Spectroscopy of surface-induced noise using shallow spins in diamond*, *Phys. Rev. Lett.* **114** (2015), no. 1 017601.

[106] B. A. Myers, A. Das, M. C. Dartiailh, K. Ohno, D. D. Awschalom, and A. C. Bleszynski Jayich, *Probing surface noise with depth-calibrated spins in diamond*, *Phys. Rev. Lett.* **113** (Jul, 2014) 027602.

[107] P. Caravan, J. J. Ellison, T. J. McMurry, and R. B. Lauffer, *Gadolinium(III) chelates as MRI contrast agents: Structure, dynamics, and applications*, *Chem. Rev.* **99** (1999), no. 9 2293–2352.

[108] A. M. Raitsimring, C. Gunanathan, A. Potapov, I. Efremenko, J. M. L. Martin, D. Milstein, and D. Goldfarb, *Gd3+ complexes as potential spin labels for high field pulsed epr distance measurements*, *Journal of the American Chemical Society* **129** (2007), no. 46 14138–14139. PMID: 17963387.

[109] C. Li, R. Soleyman, M. Kohandel, and P. Cappellaro, *Sars-cov-2 quantum sensor based on nitrogen-vacancy centers in diamond*, *Nano Letters* **22** (2022), no. 1 43–49. PMID: 34913700.

[110] C. L. Degen, F. Reinhard, and P. Cappellaro, *Quantum sensing*, *Rev. Mod. Phys.* **89** (Jul, 2017) 035002.

[111] T. van der Sar, F. Casola, R. Walsworth, and A. Yacoby, *Nanometre-scale probing of spin waves using single electron spins*, *Nature Communications* **6** (Aug, 2015) 7886.

[112] C. Du, T. van der Sar, T. X. Zhou, P. Upadhyaya, F. Casola, H. Zhang, M. C. Onbasli, C. A. Ross, R. L. Walsworth, Y. Tserkovnyak, and A. Yacoby, *Control and local measurement of the spin chemical potential in a magnetic insulator*, *Science* **357** (2017), no. 6347 195–198.

[113] L. S. Langsjoen, A. Poudel, M. G. Vavilov, and R. Joynt, *Electromagnetic fluctuations near thin metallic films*, *Phys. Rev. B* **89** (Mar, 2014) 115401.

[114] S. Kolkowitz, A. Safira, A. A. High, R. C. Devlin, S. Choi, Q. P. Unterreithmeier, D. Patterson, A. S. Zibrov, V. E. Manucharyan, H. Park, and M. D. Lukin, *Probing johnson noise and ballistic transport in normal metals with a single-spin qubit*, *Science* **347** (2015), no. 6226 1129–1132.

[115] T. I. Andersen, B. L. Dwyer, J. D. Sanchez-Yamagishi, J. F. Rodriguez-Nieva, K. Agarwal, K. Watanabe, T. Taniguchi, E. A. Demler, P. Kim, H. Park, and M. D. Lukin, *Electron-phonon instability in graphene revealed by global and local noise probes*, *Science* **364** (2019), no. 6436 154–157.

[116] D. Schmid-Lorch, T. Häberle, F. Reinhard, A. Zappe, M. Slota, L. Bogani, A. Finkler, and J. Wrachtrup, *Relaxometry and dephasing imaging of superparamagnetic magnetite nanoparticles using a single qubit*, *Nano Letters* **15** (2015), no. 8 4942–4947. PMID: 26218205.

[117] S. Steinert, F. Ziem, L. T. Hall, A. Zappe, M. Schweikert, N. Götz, A. Aird, G. Balasubramanian, L. Hollenberg, and J. Wrachtrup, *Magnetic spin imaging*

under ambient conditions with sub-cellular resolution, *Nature Communications* **4** (Mar, 2013) 1607.

[118] M. Pelliccione, B. A. Myers, L. M. A. Pascal, A. Das, and A. C. Bleszynski Jayich, *Two-dimensional nanoscale imaging of gadolinium spins via scanning probe relaxometry with a single spin in diamond*, *Phys. Rev. Appl.* **2** (Nov, 2014) 054014.

[119] A. O. Sushkov, N. Chisholm, I. Lovchinsky, M. Kubo, P. K. Lo, S. D. Bennett, D. Hunger, A. Akimov, R. L. Walsworth, H. Park, and M. D. Lukin, *All-optical sensing of a single-molecule electron spin*, *Nano Letters* **14** (2014), no. 11 6443–6448. PMID: 25333198.

[120] J.-P. Tetienne, T. Hingant, L. Rondin, A. Cavaillès, L. Mayer, G. Dantelle, T. Gacoin, J. Wrachtrup, J.-F. Roch, and V. Jacques, *Spin relaxometry of single nitrogen-vacancy defects in diamond nanocrystals for magnetic noise sensing*, *Phys. Rev. B* **87** (Jun, 2013) 235436.

[121] S. Pezzagna, B. Naydenov, F. Jelezko, J. Wrachtrup, and J. Meijer, *Creation efficiency of nitrogen-vacancy centres in diamond*, *New Journal of Physics* **12** (jun, 2010) 065017.

[122] Z. Yuan, M. Fitzpatrick, L. V. H. Rodgers, S. Sangtawesin, S. Srinivasan, and N. P. de Leon, *Charge state dynamics and optically detected electron spin resonance contrast of shallow nitrogen-vacancy centers in diamond*, *Phys. Rev. Res.* **2** (Aug, 2020) 033263.

[123] M. Schaffry, E. M. Gauger, J. J. L. Morton, and S. C. Benjamin, *Proposed spin amplification for magnetic sensors employing crystal defects*, *Phys. Rev. Lett.* **107** (2011), no. 20 207210.

[124] A. O. Sushkov, I. Lovchinsky, N. Chisholm, R. L. Walsworth, H. Park, and M. D. Lukin, *Magnetic resonance detection of individual proton spins using quantum reporters*, *Phys. Rev. Lett.* **113** (Nov, 2014) 197601.

[125] M. Joos, D. Bluvstein, Y. Lyu, D. M. Weld, and A. Bleszynski Jayich, *Protecting qubit coherence by spectrally engineered driving of the spin environment*, *Npj Quantum Inf.* **8** (2021), no. 1 47.

[126] B. L. Dwyer, L. V. H. Rodgers, E. K. Urbach, D. Bluvstein, S. Sangtawesin, H. Zhou, Y. Nassab, M. Fitzpatrick, Z. Yuan, K. De Greve, E. L. Peterson, H. Knowles, T. Sumarac, J.-P. Chou, A. Gali, V. Dobrovitski, M. D. Lukin, and N. P. de Leon, *Probing spin dynamics on diamond surfaces using a single quantum sensor*, *PRX Quantum* **3** (Dec, 2022) 040328.

[127] R. Chao and B. W. Reichardt, *Quantum Error Correction with Only Two Extra Qubits*, *Phys. Rev. Lett.* **121** (aug, 2018) 050502.

[128] A. Laraoui, F. Dolde, C. Burk, F. Reinhard, J. Wrachtrup, and C. A. Meriles, *High-resolution correlation spectroscopy of 13c spins near a nitrogen-vacancy centre in diamond*, *Nature Communications* **4** (Apr, 2013) 1651.

[129] D. Goldfarb, *Gd3+ spin labeling for distance measurements by pulse epr spectroscopy*, *Phys. Chem. Chem. Phys.* **16** (2014) 9685–9699.

[130] M. Pelliccione, A. Jenkins, P. Ovartchaiyapong, C. Reetz, E. Emmanouilidou, N. Ni, and A. C. Bleszynski Jayich, *Scanned probe imaging of nanoscale magnetism at cryogenic temperatures with a single-spin quantum sensor*, *Nat. Nanotechnol.* **11** (2016), no. 8 700–705.

[131] H. K. Kim, G. H. Lee, T. J. Kim, and Y. Chang, *Determination of correlation times of new paramagnetic gadolinium MR contrast agents by EPR and 17O NMR*, *Bull. Korean Chem. Soc.* **30** (2009), no. 4 849–852.

[132] A. Finco, A. Haykal, R. Tanos, F. Fabre, S. Chouaieb, W. Akhtar, I. Robert-Philip, W. Legrand, F. Ajejas, K. Bouzehouane, N. Reyren, T. Devolder, J. P. Adam, J. V. Kim, V. Cros, and V. Jacques, *Imaging non-collinear antiferromagnetic textures via single spin relaxometry*, *Nat. Commun.* **12** (2021), no. 1 767.

[133] B. Grotz, J. Beck, P. Neumann, B. Naydenov, R. Reuter, F. Reinhard, F. Jelezko, J. Wrachtrup, D. Schweinfurth, B. Sarkar, and P. Hemmer, *Sensing external spins with nitrogen-vacancy diamond*, *New J. Phys.* **13** (2011), no. 5 055004.

[134] M. S. Grinolds, M. Warner, K. De Greve, Y. Dovzhenko, L. Thiel, R. L. Walsworth, S. Hong, P. Maletinsky, and A. Yacoby, *Subnanometre resolution in three-dimensional magnetic resonance imaging of individual dark spins*, *Nat. Nanotechnol.* **9** (2014), no. 4 279–284.

[135] J. J. L. Morton, A. M. Tyryshkin, A. Ardavan, K. Porfyrakis, S. A. Lyon, and G. A. D. Briggs, *Environmental effects on electron spin relaxation in N@ C60*, *Phys. Rev. B* **76** (2007), no. 8 085418.

[136] K. Bader, D. Dengler, S. Lenz, B. Endeward, S. D. Jiang, P. Neugebauer, and J. Van Slageren, *Room temperature quantum coherence in a potential molecular qubit*, *Nat. Commun.* **5** (2014), no. 1 5304.

[137] D. Pinto, D. Paone, B. Kern, T. Dierker, R. Wieczorek, A. Singha, D. Dasari, A. Finkler, W. Harneit, J. Wrachtrup, and K. Kern, *Readout and control of an endofullerene electronic spin*, *Nat. Commun.* **11** (2020), no. 1 6405.

[138] M. Kveder, D. Merunka, M. Jokić, and B. Rakvin, *Low-temperature electron-spin relaxation in the crystalline and glassy states of solid ethanol*, *Phys. Rev. B* **77** (2008), no. 9 094202.

[139] F. Shi, F. Kong, P. Zhao, X. Zhang, M. Chen, S. Chen, Q. Zhang, M. Wang, X. Ye, Z. Wang, Z. Qin, X. Rong, J. Su, P. Wang, P. Z. Qin, and J. Du, *Single-DNA electron spin resonance spectroscopy in aqueous solutions*, *Nat. Methods* **15** (2018), no. 9 697–699.

[140] N. Y. Yao, C. R. Laumann, S. Gopalakrishnan, M. Knap, M. Müller, E. A. Demler, and M. D. Lukin, *Many-body localization in dipolar systems*, *Phys. Rev. Lett.* **113** (Dec, 2014) 243002.

[141] S. Choi, J. Choi, R. Landig, G. Kucsko, H. Zhou, J. Isoya, F. Jelezko, S. Onoda, H. Sumiya, V. Khemani, C. von Keyserlingk, N. Y. Yao, E. Demler, and M. D. Lukin, *Observation of discrete time-crystalline order in a disordered dipolar many-body system*, *Nature* **543** (Mar, 2017) 221–225.

[142] E. J. Davis, B. Ye, F. Machado, S. A. Meynell, W. Wu, T. Mittiga, W. Schenken, M. Joos, B. Kobrin, Y. Lyu, Z. Wang, D. Bluvstein, S. Choi, C. Zu, A. C. B. Jayich, and N. Y. Yao, *Probing many-body dynamics in a two-dimensional dipolar spin ensemble*, *Nature Physics* **19** (Jun, 2023) 836–844.

[143] P. W. Anderson and P. R. Weiss, *Exchange narrowing in paramagnetic resonance*, *Rev. Mod. Phys.* **25** (Jan, 1953) 269–276.

[144] J. R. Klauder and P. W. Anderson, *Spectral diffusion decay in spin resonance experiments*, *Phys. Rev.* **125** (Feb, 1962) 912–932.

[145] M. Glasbeek and R. Hond, *Phase relaxation of photoexcited triplet spins in cao*, *Phys. Rev. B* **23** (Apr, 1981) 4220–4235.

[146] K. Salikhov, S. Dzuba, and A. Raitsimring, *The theory of electron spin-echo signal decay resulting from dipole-dipole interactions between paramagnetic centers in solids*, *Journal of Magnetic Resonance (1969)* **42** (1981), no. 2 255–276.

[147] F. M. Cucchietti, J. P. Paz, and W. H. Zurek, *Decoherence from spin environments*, *Phys. Rev. A* **72** (Nov, 2005) 052113.

[148] L. Cywiński, R. M. Lutchyn, C. P. Nave, and S. Das Sarma, *How to enhance dephasing time in superconducting qubits*, *Phys. Rev. B* **77** (May, 2008) 174509.

[149] V. V. Dobrovitski, A. E. Feiguin, D. D. Awschalom, and R. Hanson, *Decoherence dynamics of a single spin versus spin ensemble*, *Phys. Rev. B* **77** (Jun, 2008) 245212.

[150] V. V. Dobrovitski, A. E. Feiguin, R. Hanson, and D. D. Awschalom, *Decay of rabi oscillations by dipolar-coupled dynamical spin environments*, *Phys. Rev. Lett.* **102** (Jun, 2009) 237601.

[151] Z.-H. Wang, G. de Lange, D. Ristè, R. Hanson, and V. V. Dobrovitski, *Comparison of dynamical decoupling protocols for a nitrogen-vacancy center in diamond*, *Phys. Rev. B* **85** (Apr, 2012) 155204.

[152] Z.-H. Wang and S. Takahashi, *Spin decoherence and electron spin bath noise of a nitrogen-vacancy center in diamond*, *Phys. Rev. B* **87** (Mar, 2013) 115122.

[153] W. Yang, W.-L. Ma, and R.-B. Liu, *Quantum many-body theory for electron spin decoherence in nanoscale nuclear spin baths*, *Reports on Progress in Physics* **80** (nov, 2016) 016001.

[154] N. Y. Yao, C. R. Laumann, S. Gopalakrishnan, M. Knap, M. Müller, E. A. Demler, and M. D. Lukin, *Many-body localization in dipolar systems*, *Phys. Rev. Lett.* **113** (Dec, 2014) 243002.

[155] S. Choi, J. Choi, R. Landig, G. Kucsko, H. Zhou, J. Isoya, F. Jelezko, S. Onoda, H. Sumiya, V. Khemani, C. von Keyserlingk, N. Y. Yao, E. Demler, and M. D. Lukin, *Observation of discrete time-crystalline order in a disordered dipolar many-body system*, *Nature* **543** (Mar, 2017) 221–225.

[156] N. Y. Yao, M. P. Zaletel, D. M. Stamper-Kurn, and A. Vishwanath, *A quantum dipolar spin liquid*, *Nature Physics* **14** (Apr, 2018) 405–410.

[157] J. Choi, H. Zhou, H. S. Knowles, R. Landig, S. Choi, and M. D. Lukin, *Robust dynamic hamiltonian engineering of many-body spin systems*, *Phys. Rev. X* **10** (Jul, 2020) 031002.

[158] D. A. Abanin, E. Altman, I. Bloch, and M. Serbyn, *Colloquium: Many-body localization, thermalization, and entanglement*, *Rev. Mod. Phys.* **91** (May, 2019) 021001.

[159] R. J. Sewell, M. Koschorreck, M. Napolitano, B. Dubost, N. Behbood, and M. W. Mitchell, *Magnetic sensitivity beyond the projection noise limit by spin squeezing*, *Phys. Rev. Lett.* **109** (Dec, 2012) 253605.

[160] T. Bilitewski, L. De Marco, J.-R. Li, K. Matsuda, W. G. Tobias, G. Valtolina, J. Ye, and A. M. Rey, *Dynamical generation of spin squeezing in ultracold dipolar molecules*, *Phys. Rev. Lett.* **126** (Mar, 2021) 113401.

[161] G. Bornet, G. Emperauger, C. Chen, B. Ye, M. Block, M. Bintz, J. A. Boyd, D. Barredo, T. Comparin, F. Mezzacapo, T. Roscilde, T. Lahaye, N. Y. Yao, and A. Browaeys, *Scalable spin squeezing in a dipolar rydberg atom array*, *Nature* **621** (Sep, 2023) 728–733.

[162] M. Block, B. Ye, B. Roberts, S. Chern, W. Wu, Z. Wang, L. Pollet, E. J. Davis, B. I. Halperin, and N. Y. Yao, *A universal theory of spin squeezing*, 2023.

[163] S. A. Meynell, C. A. McLellan, L. B. Hughes, W. Wang, T. E. Mates, K. Mukherjee, and A. C. Bleszynski Jayich, *Engineering quantum-coherent defects: The role of substrate miscut in chemical vapor deposition diamond growth*, *Applied Physics Letters* **117** (11, 2020) 194001.

[164] V. S. Perunicic, L. T. Hall, D. A. Simpson, C. D. Hill, and L. C. L. Hollenberg, *Towards single-molecule nmr detection and spectroscopy using single spins in diamond*, *Phys. Rev. B* **89** (Feb, 2014) 054432.

[165] I. Lovchinsky, A. O. Sushkov, E. Urbach, N. P. de Leon, S. Choi, K. D. Greve, R. Evans, R. Gertner, E. Bersin, C. Müller, L. McGuinness, F. Jelezko, R. L. Walsworth, H. Park, and M. D. Lukin, *Nuclear magnetic resonance detection and spectroscopy of single proteins using quantum logic*, *Science* **351** (2016), no. 6275 836–841.

[166] F. Casola, T. van der Sar, and A. Yacoby, *Probing condensed matter physics with magnetometry based on nitrogen-vacancy centres in diamond*, *Nature Reviews Materials* **3** (Jan, 2018) 17088.

[167] G. Wolfowicz, F. J. Heremans, C. P. Anderson, S. Kanai, H. Seo, A. Gali, G. Galli, and D. D. Awschalom, *Quantum guidelines for solid-state spin defects*, *Nature Reviews Materials* **6** (Oct, 2021) 906–925.

[168] M. Xie, X. Yu, L. V. H. Rodgers, D. Xu, I. Chi-Durán, A. Toros, N. Quack, N. P. de Leon, and P. C. Maurer, *Biocompatible surface functionalization architecture for a diamond quantum sensor*, *Proceedings of the National Academy of Sciences* **119** (2022), no. 8 e2114186119.

[169] R. Dolot, C. H. Lam, M. Sierant, Q. Zhao, F.-W. Liu, B. Nawrot, M. Egli, and X. Yang, *Crystal structures of thrombin in complex with chemically modified thrombin DNA aptamers reveal the origins of enhanced affinity*, *Nucleic Acids Research* **46** (04, 2018) 4819–4830.

[170] P. W. K. Rothemund, *Folding dna to create nanoscale shapes and patterns*, *Nature* **440** (Mar, 2006) 297–302.

[171] S. Rinker, Y. Ke, Y. Liu, R. Chhabra, and H. Yan, *Self-assembled dna nanostructures for distance-dependent multivalent ligand-protein binding*, *Nature Nanotechnology* **3** (Jul, 2008) 418–422.

[172] A. Gopinath, E. Miyazono, A. Faraon, and P. W. K. Rothemund, *Engineering and mapping nanocavity emission via precision placement of dna origami*, *Nature* **535** (2016), no. 7612 401–405.

[173] A. Gopinath, E. Miyazono, A. Faraon, and P. W. K. Rothemund, *Optimized assembly and covalent coupling of single-molecule dna origami nanoarrays*, *ACS Nano* **8** (2014), no. 12 12030–12040.

[174] A. Borel, E. Toth, L. Helm, A. Janossy, and A. E. Merbach, *Epr on aqueous gd3+ complexes and a new analysis method considering both line widths and shifts*, *Phys. Chem. Chem. Phys.* **2** (2000) 1311–1317.

[175] S. Rast, A. Borel, L. Helm, E. Belorizky, P. H. Fries, and A. E. Merbach, *Epr spectroscopy of mri-related gd(iii) complexes: Simultaneous analysis of multiple frequency and temperature spectra, including static and transient crystal field effects*, *Journal of the American Chemical Society* **123** (2001), no. 11 2637–2644.

[176] J. A. Clayton, K. Keller, M. Qi, J. Wegner, V. Koch, H. Hintz, A. Godt, S. Han, G. Jeschke, M. S. Sherwin, and M. Yulikov, *Quantitative analysis of zero-field splitting parameter distributions in gd(iii) complexes*, *Phys. Chem. Chem. Phys.* **20** (2018) 10470–10492.

[177] G. de Lange, D. Ristè, V. V. Dobrovitski, and R. Hanson, *Single-spin magnetometry with multipulse sensing sequences*, *Phys. Rev. Lett.* **106** (Feb, 2011) 080802.

[178] S. Rast, P. H. Fries, E. Belorizky, A. Borel, L. Helm, and A. E. Merbach, *A general approach to the electronic spin relaxation of Gd(III) complexes in solutions. Monte Carlo simulations beyond the Redfield limit*, *The Journal of Chemical Physics* **115** (10, 2001) 7554–7563.

[179] D. Kim, M. I. Ibrahim, C. Foy, M. E. Trusheim, R. Han, and D. R. Englund, *A cmos-integrated quantum sensor based on nitrogen–vacancy centres*, *Nature Electronics* **2** (Jul, 2019) 284–289.

[180] F. M. Stürner, A. Brenneis, T. Buck, J. Kassel, R. Rölver, T. Fuchs, A. Savitsky, D. Suter, J. Grimmel, S. Hengesbach, M. Förtsch, K. Nakamura, H. Sumiya, S. Onoda, J. Isoya, and F. Jelezko, *Integrated and portable magnetometer based on nitrogen-vacancy ensembles in diamond*, *Advanced Quantum Technologies* **4** (2021), no. 4 2000111.

[181] M. R. Dunn, R. M. Jimenez, and J. C. Chaput, *Analysis of aptamer discovery and technology*, *Nature Reviews Chemistry* **1** (Oct, 2017) 0076.

[182] J. Schachenmayer, A. Pikovski, and A. M. Rey, *Many-body quantum spin dynamics with monte carlo trajectories on a discrete phase space*, *Phys. Rev. X* **5** (Feb, 2015) 011022.

[183] M. A. Perlin, C. Qu, and A. M. Rey, *Spin squeezing with short-range spin-exchange interactions*, *Phys. Rev. Lett.* **125** (Nov, 2020) 223401.

[184] M. Block, B. Ye, B. Roberts, S. Chern, W. Wu, Z. Wang, L. Pollet, E. J. Davis, B. I. Halperin, and N. Y. Yao, *A universal theory of spin squeezing*, 2023.

[185] D. R. Glenn, D. B. Bucher, J. Lee, M. D. Lukin, H. Park, and R. L. Walsworth, *High-resolution magnetic resonance spectroscopy using a solid-state spin sensor*, *Nature* **555** (Mar, 2018) 351–354.

[186] N. Y. Yao, M. P. Zaletel, D. M. Stamper-Kurn, and A. Vishwanath, *A quantum dipolar spin liquid*, *Nature Physics* **14** (Apr, 2018) 405–410.

[187] C. A. McLellan, *Nitrogen-vacancy center ensembles in diamond: diamond growth and ensemble characterization for ensemble magnetometry*. Phd dissertation, University of California, Santa Barbara, Santa Barbara, CA, 2018. Available at `https://escholarship.org/uc/item/6f06r6qf#main`.